Fundamentals of (Thio)urea Catalysis

Dissertation zur Erlangung des Grades

„Doktor der Naturwissenschaften“

im Promotionsfach Chemie

am Fachbereich 09

Chemie, Pharmazie und Geowissenschaften

der Johannes Gutenberg-Universität Mainz

Amelie-Anthea Ehrhard

geboren in Pirmasens

Mainz, 2021

1. Berichterstatter: [redacted]

2. Berichterstatter: [redacted]

Tag der mündlichen Prüfung: 21.07.2021

Statutory Declaration

I hereby declare that I wrote this dissertation submitted without any unauthorized external assistance and used only sources acknowledged in the work. All textual passages, which are appropriated verbatim or paraphrased from published and unpublished texts as well as all information obtained from oral sources are duly indicated and listed in accordance with bibliographical rules. In carrying out this research, I complied with the rules of standard scientific practice as formulated in the statutes of the Johannes Gutenberg-University Mainz to insure standard scientific practice. In the chapters 4 to 6, I will write in the first person plural instead of singular (we instead of I) to make the text more readable.

Amelie Ehrhard

”Statt daran zu verzweifeln, sagte ich mir, dass ich weitermache und mich darauf konzentriere, was geht.”

– Roger Federer

Abstract

(Thio)urea catalysts have emerged as efficient and versatile catalysts for a wide range of reactions. Hydrogen-bonds are a common motif of these catalysts, however the nature of (thio)urea's hydrogen-bonds as well as the exact binding motif to the reactants (i.e. carbonyl groups) has remained elusive. The work covered in this thesis explores the fundamental interaction between (thio)urea catalysts to ketones in solution as well as the fundamental hydrogen-bonding dynamics of urea-motifs, relevant to organocatalysis. To that end, I use a combination of ^{1}H-NMR, linear IR, ultrafast Pump Probe IR and 2D-IR spectroscopy combined with DFT-calculations, in order to obtain insights into catalyst-substrate binding under catalytically relevant conditions.

In chapters 1-3, I embed this thesis in a context, discuss the theoretical background and present the experimental setups and techniques, which are used for the three main chapters.

To unravel the very fundamentals of urea's hydrogen-bonding, I study in chapter 4 urea-d4/urea mixtures in dimethylsulfoxide (DMSO) to disentangle urea's vibrational structure and dynamics. The linear IR spectra reveal spectrally separated absorption bands for ND_2 compared to ND stretching modes with significantly different linewidths. These different linewidths are confirmed with 2D-IR spectroscopy, which reveals a significantly larger inhomogeneous linewidths for ND modes as compared to ND_2 vibrations, implying that the hydrogen-bond environments give rise to a broader frequency distribution for ND compared to ND_2. Comparison to DFT calculations yields that this experimental observation can be explained with a marked asymmetry in the hydrogen-bond strength of the two hydrogen-bonds formed by an ND_2 group. This asymmetry persist for a rather long time of ~1ps. The presence of this long-lived asymmetry could explain the high directionality of urea's hydrogen-bond properties, which might be relevant for catalysis, protein denaturation, self-assembly or DNA base-pairing.

In chapter 5, I investigate the effect of the catalysts substituents containing electron-withdrawing CF_3 groups – which are known to tremendously enhance catalytic conversion – on the catalyst-substrate binding in solution with a combination of ^{1}H-NMR and linear IR spectroscopy. More specifically, I study the interaction of three diphenylthiourea (DPTU) based catalysts with zero (0CF-DPTU), two (2CF-DPTU) and four (4CF-DPTU) CF_3 substituents at the phenylring with the substrate 1,3-diphenyl-2-propenone (diphenylpropenone) in various solvents. In addition, I determine the association strength of the catalyst-substrate binding and find that the obtained association constants increase with increasing number of CF_3 substituents in the solvents dichloromethane and toluene, while there is no detectable association in acetonitrile. It is found that the enhanced binding in dichloromethane and toluene for an increasing number of CF_3 substituents correlates well with their increased catalytic

activity reported in literature and that it can explain the increased reaction rates for DPTU catalysts containing CF_3 groups.

Finally, I address the question how the binding strength is influenced by a different substrate and how the two conformers (trans-trans and trans-cis) of the catalyst affect the binding. For this purpose, I examine the interaction of the catalysts 4CF-DPTU, 2CF-DPTU and 0CF-DPTU with the substrate diphenylpropenone and compare it to the substrate acetophenone. The two conformers can be discriminated with fs-IR spectroscopy, due to their different vibrational lifetimes. By determining the association strength with ^{1}H-NMR spectroscopy, I find similar overall association constants for the two substrates, yet the chemical shift of the complex $\delta_{complex}$ is significantly reduced for the substrate acetophenone compared to diphenylpropenone. FT-IR spectra reveal in the NH region of the catalyst, as well as in the CO region of the substrate a red-shifted side band compared to the vibrations of the free molecules. The red-shifted bands are assigned to the hydrogen-bonded species and enable to spectrally discriminate free and hydrogen-bonded species. Mixtures of catalyst with substrate reveal three molecular states, which can be resolved by their different vibrational lifetimes: trans-trans, trans-cis and the hydrogen-bonded catalyst-substrate complex. The extracted associated spectrum of only the trans-cis conformer changes in the presence of the substrates and "spectrally mixes" with the spectrum of the hydrogen-bonded complexes. This observation suggests that only the trans-cis conformer forms complexes to the substrate within the experimental time window of ~10ps. This finding might help to improve the performance of thiourea catalysts by designing, for instance, conformationally more stable catalysts.

Zusammenfassung

(Thio)harnstoff Katalysatoren haben sich als effiziente und vielseitige Katalysatoren für ein breites Spektrum an Reaktionen erwiesen. Wasserstoffbrückenbindungen sind ein häufiges Motif dieser Katalysatoren, jedoch sind die Details von (Thio)harnstoff's Wasserstoffbrücken und das exakte Bindungsmotif zu den Reaktanden (z.B. Carbonylgruppen) schwer zu erfassen. Diese Dissertation untersucht die Grundlagen der Wechselwirkung zwischen (Thio)harnstoff Katalysatoren und Ketonen in Lösung, sowie die fundamentale Wasserstoffbrückenbindungs-Dynamik von Harnstoff Motifen, welche relvant sind für die Organokatalyse. Hierzu benutze ich eine Kombination von ^{1}H-NMR, linearer IR, nichtlinearer ultrakurzzeit IR und 2D-IR Spektroskopie kombiniert mit DFT-Rechnungen, um Einblicke in die Katalysator-Substrat Bindung unter katalytisch relevanten Bedingungen zu erhalten.

In den Kapiteln 1 bis 3 bette ich diese Dissertation in einen Kontext ein, diskutiere den theoretischen Hintergrund und stelle die experimentellen Aufbauten und Methoden vor, die in den drei Hauptkapiteln benutzt werden.

Um die Grundlagen der Wasserstoffbrückenbindungen des Harnstoffs zu ergünden, untersuche ich in Kapitel 4 Harnstoff-d4/Harnstoff Mischungen in dem Lösungsmittel Dimethylsulfoxid (DMSO) als Modellsystem, um dessen Schwingungsstruktur und -dynamik aufzuklären. Die linearen IR-Spektren enthüllen spektral getrennte Absorptionsbanden mit signifikant unterschiedlichen Linienbreiten für ND_2 und ND Streckschwingungen. Mittels 2D-IR Spektroskopie zeigt sich, dass die signifikant größeren Linienbreiten für ND verglichen mit ND_2 durch inhomogene Verbreiterung hervorgerufen wird, was bedeutet, dass die Wasserstoffbrückenbindungs-Umgebung bei ND Streckschwingungen zu einer breiteren Frequenzverteilung führt als bei ND_2 Streckschwingungen. Der Vergleich zu DFT Rechnungen ergibt, dass diese experimentelle Beobachtung mit einer deutlichen Asymmetrie in der Stärke der beiden Wasserstoffbrückenbindungen einer ND_2 Gruppe erklärt werden kann, welche für eine recht lange Zeit von ~1ps bestehen bleibt. Das Vorhandensein der langlebigen Asymmetrie könnte die hohe Direktionalität der Wassersroffbrückenbindungen von Harnstoffgruppen erklären, welche für die Katalyse, Proteindenaturierung, Selbstorganisation oder DNA-Basenpaarung relevant sein könnten.

In Kapitel 5 erforsche ich den Effekt von Substituenten an Katalysatoren, die CF_3 Gruppen enthalten – welche bekannt dafür sind, die katalytische Umwandlung außerordentlich zu erhöhen – auf die Katalysator-Substrat Bindung in Lösung mit einer Kombination von ^{1}H-NMR und linearer IR Spektroskopie. Genauer gesagt, untersuche ich die Wechselwirkung von drei Diphenylthioharnstoff (DPTU) basierten Katalysatoren mit null (0CF-DPTU), zwei (2CF-DPTU) und vier (4CF-DPTU) CF_3 Substituenten an dem Phenylring mit dem Substrat 1,3-Diphenyl-2-propenon (Diphenylpropenon) in unterschiedlichen Lösungsmitteln. Dazu bestimme ich die Assoziationsstärke der Katalysator-Substrat Bindung und finde, dass die erhaltenen Assoziationskonstanten in

den Lösungsmitteln Dichlormethan und Toluol mit steigender Anzahl an CF_3 Substituenten zunehmen, wobei keine detektierbare Assoziation in Acetonitril gefunden wird. Es wird festgestellt, dass die erhöhte Bindungsstärke bei einer zunehmenden Anzahl an CF_3 Substituenten in Dichlormethan und Toluol mit einer erhöhten katalytischen Aktivität aus der Literatur korreliert und dass dies die erhöhten Reaktionsgeschwindigkeiten für DPTU Katalysatoren mit CF_3 Gruppen erklären kann.

Zuletzt behandle ich die Frage inwiefern ein anderes Substrat die Bindungsstärke beeinflusst und wie die beiden Konformere des Katalysators (trans-trans and trans-cis) die Bindung beeinflussen. Zu diesem Zweck untersuche ich die Wechselwirkung der Katalysatoren 4CF-DPTU, 2CF-DPTU und 0CF-DPTU mit dem Substrat Diphenylpropenon und vergleiche sie mit dem Substrat Acetophenon. Die beiden Konformere können mittels fs-IR Spektroskopie aufgrund ihrer unterschiedlichen Schwingungslebenszeiten unterschieden werden. Durch die Bestimmung der Assoziationsstärke mittels ^{1}H-NMR Spektroskopie entdecke ich ähnliche Assoziationskonstanten für die beiden Substrate, jedoch ist die chemische Verschiebung des Komplexes $\delta_{complex}$ für das Substrat Acetophenon signifikant erniedrigt verglichen mit Diphenylpropenon. Die FT-IR Spektren enthüllen für die NH Region des Katalysators, sowie für die CO Region des Substrates eine rotverschobene Nebenbande verglichen mit den Schwingungen der freien Moleküle. Die rotverschobenen Banden können den wasserstoffbrückengebundenen Spezies zugeordnet werden was eine spektrale Unterscheidung der freien und der wasserstoffbrückengebundenen Spezies ermöglicht. Mischungen von Katalysator und Substrat enthüllen drei molekulare Zustände, welche aufgrund ihrer unterschiedlichen Schwingungslebenszeit aufgelöst werden können: trans-trans, trans-cis und der wasserstoffbrückengebundene Katalysator-Substrat Komplex. Die extrahierten assoziierten Spektren ändern sich nur für das trans-cis Konformer welche Komponenten des Spektrums der wasserstoffbrückengebundenen Komplexes enthalten. Dies legt nahe, dass nur das trans-cis Konformer innerhalb des experimentell zugaenglichen Zeitfensters von ~10ps Wasserstoffbrücken zu dem Substrat bildet. Dieses Ergebnis könnte helfen die Leistung von Thioharnstoffkatalysatoren durch z.B. das Entwerfen von konformativ stabileren Katalysatoren zu verbessern.

This thesis is based on the following publications

Chapter 4:

A. A. Ehrhard, B. Marekha and J. Hunger, Hydrogen-Bonding Asymmetry in Urea *(in preparation)*

Chapter 5:

A. A. Ehrhard, S. Jäger, C. Malm, S. Basaran and J. Hunger, CF_3-groups critically enhance the binding of thiourea catalysts to ketones – a NMR and FT-IR study, *J. Mol. Liq.*, 2019, **296**, 111829

Chapter 6:

A. A. Ehrhard, S. Jäger, A. Sell and J. Hunger, Vibrational dynamics of Thiourea Catalysts in Solution: Influence of Conformation and H-Bonding to Substrates *(in preparation)*

Other publications

C. Dreier, L.A. Prädel, **A. A. Ehrhard**, M. Wagner, J. Hunger, Association equilibria of organo-phosphoric acids with imines from a combined dielectric and nuclear magnetic resonance spectroscopy approach, *Anal. Chem., 2021, **93**, 3914-3921*

CONTENTS

1 INTRODUCTION

1.1 HISTORY OF ORGANOCATALYSIS

The effect of catalysts on chemical reactions is already known since ancient times, for instance the production of alcohol from sugar by fermentation. Another invention was for example the Döbereiner lighter in 1823, which is a reaction of hydrogen and oxygen catalyzed by platinum.[1,2] However, the mechanism of the reactions was poorly understood. The first person who defined a catalyst was Wilhelm Ostwald, who stated that a catalyst can modify the rate of a reaction without any change in the material itself.[3] For his contributions to the understanding of catalysis he received the Nobel Prize in 1909 and even nowadays we still build up on his definition of catalysis and see a catalyst as a material, which lowers the activation energy of a chemical reaction without being consumed and therefore enhancing the reaction rate without influencing the thermodynamic equilibrium.[4,5] Since this discovery, a variety of catalysts have been developed and nowadays nearly 90% of all chemical manufacturing processes in the US involve catalysis.[6] They are used, for instance in chemical synthesis, in refinery of chemicals, pollution reduction or fertilizer production.[6-8] Different fields of catalysis have been developed, such as homogeneous catalysis (the reaction occurs in the same phase, where the catalyst is present), heterogeneous catalysis (the reaction occurs in a different phase) and biocatalysis (the reaction is carried out by enzymes).[4,9,10] For the application of enantioselective reactions, like for instance the synthesis of pharmaceutics, flavors and other fine chemicals, in general homogeneous catalysis is used.[11] The most actively studied synthetic homogeneous catalysts are metal-based catalysts,[12] as the first metal-based asymmetric synthesis was already discovered in 1938. [11] However, many metal-based catalysts are expensive, toxic, and air- or moisture-sensitive. [13] When the first organocatalytic reactions were reported in the late 1990s [14-16], this research area started to grow rapidly, as there are several benefits over the metal-based catalysts: in most cases, they are easier to handle, as they are stable in air and water, they are cheap, available from biological materials, non-toxic and environmentally friendly, yet still providing good stereocontrol.[13,17,18] This is really attractive for the pharmaceutical industry, as chiral compounds (e.g. drugs) can be synthesized cheap, with simpler synthetic pathways and in a selective manner – rather than as mixtures of enantiomers – by using organocatalysis.[13,19] Organocatalysts are defined as organic compounds, consisting of nonmetal elements like carbon, hydrogen, nitrogen, oxygen, sulfur or phosphorus, which enhance the rate of a chemical reaction. [4] A necessity for a good catalyst is that it binds to one of the reactants, forming a catalyst-substrate complex, in order to weaken the bonds, which must be broken. However, the binding should not be too strong, so the product is still energetically favorable over the catalyst-substrate complex. [4] The nature of binding can be different, like for example the

catalyst can interact with the substrate via hydrogen-bonding, ionic interactions, Van-Der-Waals forces etc. [20,21]

1.2 (THIO)UREA CATALYSIS

Hydrogen-bonding donors like (thio)ureas have become popular and were found as efficient organocatalysts.[22-29] They belong to the privileged organocatalysts, which provide a good catalytic activity and/or enantioselectivity for a wide range of reactions.[19] Their application possibilities are very diverse, and there are a lot of reactions reported, which are supported by (thio)urea catalysts like e.g. Strecker reaction, addition, allylation, Michael- and Nitro-Mannich reactions.[20] Important progress in this field has been made by Schreiner and Co-workers, who introduced a very interesting system named 'Schreiner's catalyst', which is totally symmetric but enhances the reaction rates and the stereoselectivity – which is determined by the structure of the two reactants – of Diels-Alder reactions (*Figure 1-1*). [22,23] A combination of NMR, IR and ESI investigations combined with DFT calculations, found that binding interactions between thiourea catalysts and ketones arise from hydrogen-bonding interactions. More specifically, these hydrogen bonds arise between the highly polar NH proton, as well as the ortho-proton from the catalyst with the Lewis base.[30] The catalytically active NH-group of the thiourea catalyst interacts with the C=O group of the ketone via hydrogen-bonding and forms a catalyst-substrate complex. [30] The ketone, which is the substrate, is activated and reacts with the second reactant. In the last step, the thiourea catalyst is released, and the product is formed.

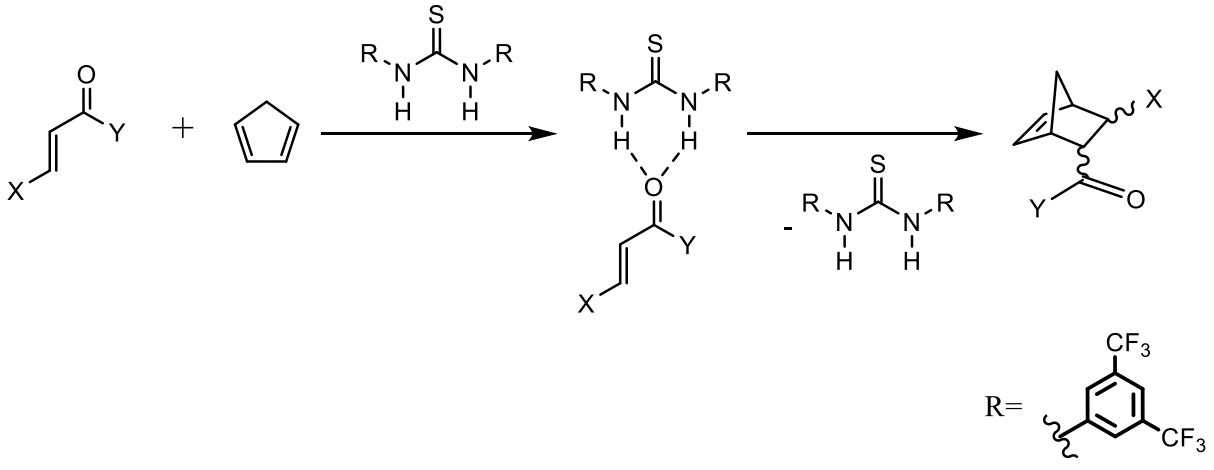

Figure 1-1: Diels-Alder cycloaddition, which is catalyzed by a thiourea catalyst. The ketone is activated by a hydrogen-bonding interaction with the catalyst.[20,23] The famous Schreiner's catalyst exhibits the side group R shown in the figure.

However, the exact nature of this hydrogen-bonding interaction is still not fully understood and might also depend on the different side groups of the substrate (X and Y) and of the catalyst (R). For instance, it was found that substrates, which possess an oxygen atom at the alpha position of the C=O group, can form an additional hydrogen-bond to the ortho-proton of the Schreiner's catalyst and not only to the two NH-groups [30]. Furthermore, it was found that electron-withdrawing groups, particularly the CF_3-group, at the phenylring have a hugely positive effect on reaction time and yield. [23] Since that discovery, the CF_3-group has been established as a common structural motif in (thio)urea organocatalysis and has attracted considerable attention to researchers, who used, for example, spectroscopic methods to determine the acidities of hydrogen-donating organocatalysts, but large areas of hydrogen-bonding organocatalysis is still not fully understood. [31] Further studies involve the determination of pK_a values [32] and relative rate constants, [23] and it was found that the rate constants increase with the acidity of the catalyst. These are two important key findings, which define catalytic properties, but this correlation is only valid for very similar catalytic structures, [33] and the rational design of catalysts and the prediction of catalytic activity and enantioselectivity still remains challenging. There are certain concepts and strategies to develop a catalyst, [34,35] but a clear approach for a rational catalyst design still remains elusive. In order to achieve a rational catalyst design in the future, it is necessary to fundamentally understand the interaction of the catalyst with the substrate. This hydrogen-bonding interaction between catalyst and substrate is also significantly influenced by the solvent, which also influences the reaction rate. For instance, it was found that counterintuitively organic transformations are significantly accelerated in a polar solvent like water, because of enhanced interactions due to 'hydrophobic hydration'.[23,36] Yet, it was also found that nonpolar solvents are crucial for the formation of hydrogen-bonded complexes.[37] Consequently, yield and selectivity are also significantly influenced by the solvent.[23,38-40] In this thesis, different spectroscopic investigations are applied to urea as a model system for (thio)urea catalysts in order to get a fundamental understanding on the structure and dynamics of urea-motifs on a molecular level. Furthermore, three different thiourea catalysts with two different substrates in various solvents are studied, in order to achieve a better understanding on these hydrogen-bonded catalyst-substrate complexes.

1.3 HYDROGEN-BONDING

The NH-groups of the (thio)urea motif bind the substrates via the formation of hydrogen-bonds, which belong to the intermolecular forces, like also dipole-dipole interactions and Van-der Waals forces. Hydrogen-bonds are one of the most fundamental molecular interactions, providing water its unique properties like the density maximum at 4°C, the large heat capacity, the high surface tension and the high

melting and freezing point of water. [41] This is important for our lives, as, for example, the DNA's double helix in our cells is dissolved in water, and solvation in a different solvent could lead to an unzipping of the DNA.[42] Hydrogen-bonding interactions are crucial for the DNA itself, as they are the structural key feature, which is responsible for the right pairing of the Watson Crick base pairs, providing the DNA its double-helical structure. [43-46] Furthermore, hydrogen-bonds play a key role in the folding of proteins to three-dimensional structures.[47,48] It is apparent that hydrogen-bonds play a fundamental role in nature, but they are also crucial in catalysis, like enzyme function. These enzymes operate as a catalyst and activate the molecule for a nucleophilic attack by hydrogen-bonding to an electrophile and reducing its electron density.[20] This mechanism of electrophile activation through hydrogen-bonding is nowadays applied frequently to synthetic catalysts and especially chiral hydrogen-bond donor catalysts have emerged to an important tool and are broadly applicable for enantioselective synthesis. [20,21]

In general, a hydrogen-bond is described as an electrostatic interaction of a hydrogen-bond donor X-H and a hydrogen-bond acceptor Y, where Y is an electron-rich atom and X is an electronegative atom, for instance, O, N, or F. It can occur in the same molecule (intramolecular) or between different molecules (intermolecular).[49,50] The binding energies are smaller than covalent bonds and lie in the range of 1 and 50 kJ mol^{-1}. [51-53] Therefore, in a liquid at ambient temperature, they undergo structural dynamics and fluctuations of hydrogen-bonds leading to the formation and breaking of hydrogen-bonds, which occur in many cases on a picosecond timescale. The fastest structural fluctuations are observed in water and occur on a sub-100fs timescale. [52-54] The length of the hydrogen-bond, which is defined as the distance between the atoms X and Y, lies in the range of 0.25-0.35nm and depends on the strength of attractive interaction between hydrogen-bond donor and acceptor, [52] which correlates with the vibrational frequency in the IR-spectrum. [53,55] The strength of the hydrogen-bond can be classified as weak, medium-strong or strong hydrogen-bond, giving rise to distinct spectral features in linear infrared spectroscopy. [53,56] Consider the example of an OH group. If hydrogen-bonding is absent, the hydrogen-bond distance will be larger than 3 Å, and the free OH-stretching vibration can be found at ~3600cm^{-1}. [53,56] In case of weak hydrogen-bonding the hydrogen-bond distance is between 2.8 and 3 Å and the vibrational frequency of the OH-stretching vibration is broader and located at lower frequencies with respect to the free OH ($\Delta\nu$ = 100-300cm^{-1}). [53,56] A prominent example is the hydrogen-bonding network of water, where weak hydrogen-bonding gives rise to fast structural fluctuations. [53,56] Medium-strong hydrogen-bonds (hydrogen-bond distance of ~ 2.6 and 2.8 Å) reveal an even larger shift to lower frequencies, with the OH-stretching vibration being shifted of 300-1000cm^{-1} with respect to the free OH. These bands are typically very broad, asymmetric and featureless and are assigned to overtones and combination bands. [53,56] If the hydrogen-bond length is smaller than 2.6 Å, strong hydrogen-bonds are present, which exhibit very different spectral features. The OH-stretching vibration is shifted to even lower wavenumbers and it gets very broad by extending over a range

of 1000-1500cm^{-1}, or it even covers the mid-IR region completely. A further decrease of the hydrogen-bond length to less than 2.45 Å, yields again rather small half-widths of ~ 200cm^{-1} centered at 1100cm^{-1}. [56] In general, hydrogen-bonds can exhibit a wide variety of spectral characteristics in the IR-spectrum, but in this thesis, only weak and medium-strong hydrogen-bonds are considered. To investigate the characteristics of hydrogen-bonded species, IR-spectroscopy and NMR spectroscopy have proven to be useful techniques.[57] With NMR spectroscopy, the signal of the proton can be detected upon hydrogen-bonding, which enables to study the strength of attraction by performing a concentration-dependent measurement series.[58,59] However, the timescale of NMR experiments (microseconds) is much shorter than the formation and breaking of hydrogen-bonds (picoseconds), which enables to measure only the average of the investigated system.[57] Therefore, linear IR-spectroscopy is a useful tool to also discriminate between free and hydrogen-bonded species as hydrogen-bonding shifts the frequency of the vibration to lower frequencies. [52,60,61] It also exhibits a better time resolution, as it probes molecular vibrations, which occur on a timescale of 10^{-13} s. [62] To probe molecular motions and interactions, femtosecond IR pump-probe spectroscopy has emerged as an important tool, as it enables to excite a molecular vibration with an ultrashort IR pump pulse and to follow it in real-time with an IR probe pulse, which is variable in time. [62-64] This enables, for instance, to extract the population relaxation and the reorientation time. [63] The femtosecond pulses can resolve the molecular motions and interactions, as these processes take longer than the duration of the laser pulse. [57] In order to also extract properties of different subensembles of hydrogen-bonded molecules, 2D-IR-spectroscopy has proven to be a useful technique, [52,57] as it is similar to femtosecond IR pump-probe spectroscopy, but it provides an additional resolution along the pump frequency axis. [65] By exciting only a small subensemble of hydrogen-bonded molecules, their dynamics and reorientation can be studied. The technique provides as main information vibrational couplings and lineshapes, from which spectral diffusion, the (in)homogeneity of the local environment of the molecule, energy transfer and coupling between functional groups can be determined. [52,56,66-68] A combination of these techniques is applied to the catalyst-substrate complexes and the model system urea in solution in order to study their hydrogen-bonding characteristics like, for instance, the binding strength and the inhomogeneity of the local environment.

2 THEORY

2.1 OVERVIEW

To provide insight into catalyst-substrate binding of (thio)urea catalysts to ketones at catalytically relevant conditions, which is vital to understand and predict catalytic efficiencies, I use a combination of Fourier-transform infrared absorption (FT-IR) spectroscopy, ultrafast infrared pump-probe (fs-IR) spectroscopy, two-dimensional infrared (2D-IR) spectroscopy and nuclear magnetic resonance (NMR) spectroscopy. The underlying theory of these techniques will be discussed in this chapter. To describe the interaction between light and matter, I will use a semiclassical approach, where I describe the light classically (by using the Maxwell equations) and where I describe the material with a quantum mechanical approach. To provide a basic understanding of infrared spectroscopy techniques, I will start with the classical description of a molecule and will move on to the quantum mechanical approach for linear infrared spectroscopy. This is extended to nonlinear infrared spectroscopy and the techniques fs-IR and 2D-IR will be discussed in more detail. Finally, NMR spectroscopy will be introduced, which exhibits certain similarities to 2D-IR spectroscopy, but the used radiation lies in a different frequency range, and therefore the technique probes the nuclear spin of protons instead of molecular vibrations.

2.2 LINEAR INFRARED SPECTROSCOPY

Spectroscopic methods are based on the interaction of light with matter. For example, in IR-spectroscopy, the oscillators of molecules interact with an electromagnetic wave in the infrared region of the electromagnetic spectrum. In simple terms, the energy of the radiation excites the molecules from the vibrational ground state $v = 0$ to the first vibrational excited state $v = 1$, and the molecule starts to oscillate. Before describing this interaction, light and matter will be explained in an individual picture.

2.2.1 DESCRIPTION OF LIGHT

Linear polarized light is frequently used for spectroscopic methods, like for instance infrared spectroscopy. It can be seen as an electromagnetic wave, where the electrical and the magnetic field vector are perpendicular to each other (*Figure 2-1*).

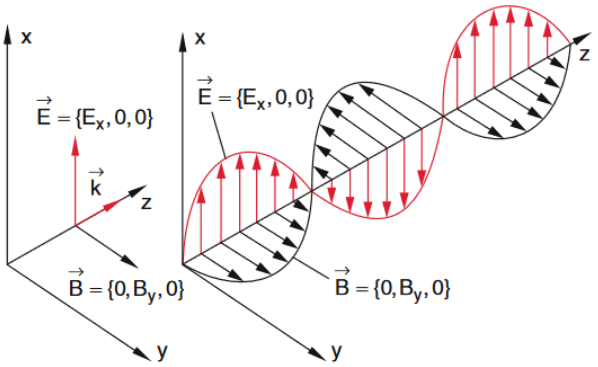

Figure 2-1: Electromagnetic and magnetic field vector of a linear polarized electromagnetic wave. This figure was published in 'Experimentalphysik 2, Elektrizität und Optik', Wolfgang Demtröder, p. 196, Copyright Springer (2013). Reprinted with permission of Springer. [69]

A monochromatic electromagnetic wave can be described as

$$\vec{E}(t) = \overrightarrow{E_0}\cos(\omega t), \tag{2-1}$$

which shows the time-dependence of the electromagnetic field $\vec{E}(t)$. Therefore, the energy of the electromagnetic wave depends on the angular frequency ω, the time t and the amplitude of the electric field $\overrightarrow{E_0}$. The relation of the energy E and the frequency υ of an electromagnetic wave is given by:

$$E = h \cdot \upsilon = h \cdot \frac{\omega}{2\pi}, \tag{2-2}$$

where h is the Planck's constant. By using the speed of light c, the frequency can also be transformed into the wavelength λ:

$$c = \lambda \cdot \upsilon \tag{2-3}$$

To describe the light in a classical picture, one can use the four Maxwell's equations, which describe the propagation of electromagnetic fields. More specifically, they are used to describe the relationship of electric fields $\vec{E}$ and magnetic fields $\vec{B}$ together, as well as their relationship to electric charges and electric current: [69-71]

$$\vec{\nabla} \cdot \vec{E} = \frac{\rho}{\varepsilon_0} \tag{2-4}$$

$$\vec{\nabla} \cdot \vec{B} = 0 \tag{2-5}$$

$$\vec{\nabla} \times \vec{E} = -\frac{\partial \vec{B}}{\partial t} \tag{2-6}$$

$$\vec{\nabla} \times \vec{B} = \mu_0 \vec{j} + \mu_0 \varepsilon_0 \frac{\partial \vec{E}}{\partial t}, \tag{2-7}$$

where ρ is the charge density, $\vec{j}$ is the current density, μ_0 is the vacuum permeability and ε_0 is the vacuum permittivity. Maxwell's equations indicate that given charge densities and changing magnetic fields create electric fields. Given currents and changing electric fields create magnetic fields. [69,71]

By taking the curl of equation (2-6) and assuming that the material is nonmagnetic ($\vec{B} = \mu_0 \cdot \vec{H}$) and that no free charges (ρ=0) and no free currents ($\vec{j}$=0) are contained, one can derive the wave equation in free space. For the monochromatic electric field, which propagates through the medium, it is assumed that an electric displacement field $\vec{D}$ inside the material is created: [72]

$$\vec{D} = \varepsilon_0 \cdot \vec{E} + \vec{P}, \tag{2-8}$$

where $\vec{P}$ is the macroscopic polarization, which originates from the interaction of the material with the electric field. By using these assumptions and inserting equation (2-8) into the curl of equation (2-6), the propagation of the electromagnetic wave through a material can be described: [72]

$$\nabla^2 \vec{E} - \frac{1}{c^2} \frac{\partial^2 \vec{E}}{\partial t^2} = \frac{1}{\varepsilon_0 c^2} \frac{\partial^2 \vec{P}}{\partial t^2}, \tag{2-9}$$

where the macroscopic polarization $\vec{P}$ is the only material-dependent property, which is relevant for light-matter interactions. The wave equation links the motion of the electric field with the polarization of the material. The polarization $\vec{P}$ will be explained in further detail in chapter 2.2.3.2.

2.2.2 DESCRIPTION OF MATTER

To describe the material, a quantum mechanical approach is used, but for an intuitively accessible picture, the classic description is explained first.

2.2.2.1 MODEL OF THE CLASSICAL HARMONIC OSCILLATOR

By considering a molecule with two atoms, one can imagine two point masses, which are connected by a spring (*Figure 2-2*).

The deflection x between the atoms corresponds to the change of distance from the equilibrium position:

$$x = r - r_0 \tag{2-10}$$

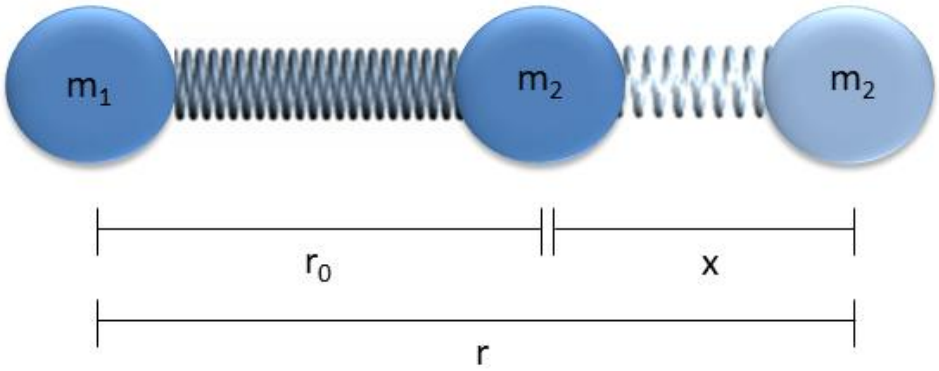

Figure 2-2: Simplified model of a vibration, where two atoms are seen as point masses m_1 and m_2, which are connected by a spring. The force is proportional to the deflection x.

The spring force for small deflections around the equilibrium position in the harmonic case can be described by using the Hooke's law: [73]

$$F = -k \cdot x = -\frac{dV}{dx}, \tag{2-11}$$

which shows that the force F is proportional to the deflection x. The derivative of the potential energy $V(x)$ reveals the force applied to the system, whereas the force constant k is constant and is characteristic of the binding strength, which connects the atoms. Via integration, a parabolic potential between the deflection and the potential energy can be found: [73]

$$V = \frac{1}{2}kx^2. \tag{2-12}$$

It means that the potential energy is required to change the deflection between the two atoms by a distance x. By equating Newton's law

$$F = m \cdot \frac{d^2x}{dt^2} \tag{2-13}$$

with Hooke's law (equation (2-11)), one finds after rearranging and solving the differential equation, the vibrational frequency of the harmonic oscillator υ_0: [73]

$$\frac{1}{t_s} = \upsilon_0 = \frac{1}{2\pi}\sqrt{\frac{k}{m'}}, \tag{2-14}$$

where m' represents the oscillation of the reduced mass around the center of mass. The time t_s is the time needed for one oscillation. Therefore, vibrational frequency υ_0 depends on the masses of the atoms and their binding strength. This makes an absorption at a specific frequency highly characteristic of a certain molecule. This simplified model can be used to study the oscillations of chemical bonds within molecules. [73]

2.2.2.2 THE QUANTUM MECHANICAL HARMONIC OSCILLATOR

With a quantum mechanical consideration of the harmonic oscillator, one needs to take the Schrödinger equation (SE) as ansatz: [5]

$$\hat{\mathrm{H}}\,\boldsymbol{\Psi} = \boldsymbol{E}\,\boldsymbol{\Psi}, \tag{2-15}$$

where the Hamilton Operator $\hat{\mathrm{H}}$ applied to the wave function Ψ, will provide the energy of the system. The wave function describes in which state a system is. It cannot be experimentally observed, but one can determine the probability density function $|\Psi(x)^2|$, which is a measure of the probability to find a particle at a certain position. For the one-dimensional harmonic oscillator, the Hamilton operator $\hat{\mathrm{H}}$ consists of two parts: the first summand describes the kinetic energy, and the second summand describes the potential energy: [5]

$$\hat{\mathrm{H}} = -\frac{\hbar^2}{2\mu}\frac{d^2}{dx^2} + \frac{1}{2}kx^2 \tag{2-16}$$

After inserting the Hamilton operator into the SE, one receives

$$\frac{d^2\Psi}{dx^2} + \frac{2\mu}{\hbar^2}\left(E - \frac{1}{2}kx^2\right)\Psi = 0. \tag{2-17}$$

The solution of this differential equation leads to the occurrence of the quantum number v. With considering equation (2-14), one finds discrete energy levels for oscillations, which leads to quantized energies: [73]

$$E_v = h \cdot \upsilon\left(v + \frac{1}{2}\right), \tag{2-18}$$

where the energy E_v of the harmonic oscillator is dependent on the Planck constant h, the quantum number v and the oscillation frequency υ. Interpretation of this equation yields that only certain energies of the oscillator of a molecular vibration are allowed. Furthermore, the energy difference between two allowed states v and $v + 1$ is always exactly $h \cdot \upsilon$, the energy levels occur in equidistant steps. From the transition dipoles

(see chapter 2.2.3.1), one finds that transitions between energy levels are only allowed if the quantum number changes by 1. This results in the selection rule: [73]

$$\Delta v = \pm 1 \tag{2-19}$$

2.2.2.3 *THE QUANTUM MECHANICAL ANHARMONIC OSCILLATOR*

The model of the harmonic oscillator does not reflect the reality because at small distances between the atoms, one expects a repulsion due to the Coulomb force between the atomic nuclei. The harmonic oscillator cannot accurately describe this, as the left side of the potential, which describes small internuclear distances, will adopt negative distances for large values of the potential energy V. Therefore, the left side of the potential needs to increase steeper than for the harmonic oscillator. Additionally, one would expect a decrease in the binding strength with large deflections pending the complete dissociation. Therefore, the potential energy cannot be described with a parabolic potential, which would be infinitely high at infinitely large distances. A more realistic way to describe this behavior is to use an anharmonic potential. A good approximation for many anharmonic potentials is the Morse potential, which reveals a finite energy at which the bond breaks. The difference can be seen in *Figure 2-3*, which compares the potential of the harmonic oscillator and the Morse potential. It shows the potential energy as a function of internuclear distance. At distances, where both nuclei are close, the harmonic potential adopts negative deflections for large potential energies.

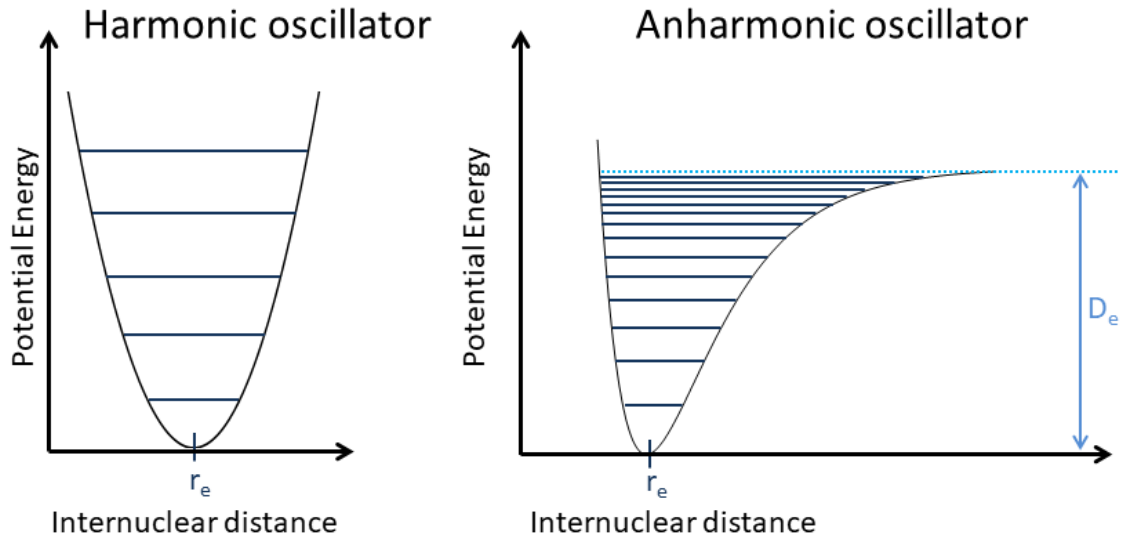

Figure 2-3: Schematic picture of a harmonic and an anharmonic oscillator of a vibration with the internuclear equilibrium position r_e. The potential energy is shown as a function of the internuclear distance r. In case of the harmonic oscillator, the spacings between the energy levels are equal, whereas the anharmonic oscillator shows a decrease in the transition energies with increasing potential energy.

Hence, the steepness of the potential at the left side must be larger than it is for the harmonic oscillator. For larger distances between the nuclei, the potential increases less steeply and approximates the dissociation energy D_e. Above this dissociation limit, the energy is not quantized anymore, there is an energy continuum, which means that the particle is free. The energy difference between the horizontal line (dashed line in *Figure 2-3*) and the minimum of the potential curve corresponds to the dissociation energy D_e. As result, the energy levels occur not in equidistant steps, as it was the case for the harmonic oscillator. In contrast, the distance between the energy levels of the anharmonic oscillator decrease with increasing potential energy. [73]

The potential energy $V(r)$ of the anharmonic oscillator can be described in good approximation with the empirical Ansatz from Morse: [73]

$$V(r) = D_e \left[1 - e^{-\beta(r-r_e)}\right]^2, \tag{2-20}$$

where D_e is the dissociation energy, r_e is the equilibrium position, r is the displacement from that equilibrium position and β is a constant and describes the steepness of the potential. For the energy levels and the vibrational energies of the Schrödinger equation with the Morse function follows: [73]

$$E_v = h \cdot \upsilon \left(v + \frac{1}{2}\right) - h \cdot \upsilon \cdot \beta \left(v + \frac{1}{2}\right)^2 \tag{2-21}$$

In contrast to the harmonic oscillator, also transitions to higher energy levels are allowed. This means for the selection rules of the anharmonic oscillator:

$$\Delta v = \pm 1, \pm 2, \pm 3, \ldots \tag{2-22}$$

The dissociation energy can be approximated by a sum over the finite distances between the energy levels, which was invented by Birge and Sponer (1926): [73]

$$D_e = \frac{h \cdot \mathrm{U}}{4 \cdot \beta} \tag{2-23}$$

To study the vibrational transition between these energy levels, one can use infrared (IR) radiation, because the energy that is needed to excite a molecular vibration corresponds to light in the IR region of the electromagnetic spectrum (see equation (2-18). By using weak IR light and assuming that all molecules are in the vibrational ground state, the transition from the vibrational ground state to the first vibrational excited state can be investigated by linear infrared spectroscopy. However, to also examine transitions from higher energy levels, e.g. the transition from the first to the second vibrational excited state, and determine the anharmonicity of the potential, one can choose nonlinear infrared spectroscopy, which will be discussed in section 2.3. Additionally, one needs to consider the selection rules, as not every vibration is IR-

active. Which vibrations are IR-active and how the electric field interacts with the material will be discussed in the following section.

2.2.3 *INTERACTION OF LIGHT WITH MATTER*

To do infrared spectroscopic investigations, one needs to consider the interaction of the electric field with the material, whereas the electric field interacts with the transition dipole moment of the material and creates a macroscopic polarization inside the material. Therefore, the existence of a transition dipole moment is a prerequisite for infrared spectroscopic investigations and the requirement needs to be fulfilled that the dipole moment during the vibration is changing ($\frac{d\mu_0}{dx} \neq 0$). The dipole moment, the polarization, and the interaction between light and matter are discussed in this section.

2.2.3.1 *TRANSITION DIPOLE MOMENT*

In a classical picture, the static dipole moment μ_0 of a molecule arises from the separation of partial charges within the molecule and is defined by the product of their charge q and their distance x and is given for a heteronuclear diatomic molecule by [5]

$$\mu_0 = q \cdot x. \tag{2-24}$$

If a weak electric field propagates through the medium, it exerts a force on the valence electrons and creates a separation of the bound charges, which induces a dipole moment μ_{ind}. Thus, the resulting induced electric dipole μ is given by the sum of the static dipole moment μ_0 and the induced dipole moment μ_{ind}:

$$\mu = \mu_0 + \mu_{ind} = \mu_0 + \alpha\, \vec{E}(t), \tag{2-25}$$

The induced dipole moment can be calculated by multiplying the electric field with the polarizability α, which is a measure of the tendency to acquire a dipole moment. It indicates the easiness of shifting charges within a molecule in an electric field $\vec{E}(t)$. [73,74]

Quantum mechanically, one needs to consider for a transition between two states the transition dipole moment, which can be imagined as a charge redistribution during the vibrational transition. The transition is allowed, if the transition dipole moment $\overrightarrow{R_v}$ is non-zero. It is calculated by: [5,75]

$$\overrightarrow{R_v} = \int \Psi_v'^{*}\, \hat{\mu}\, \Psi_v''\, dx, \tag{2-26}$$

where $\Psi_v'^*$ and Ψ_v'' are the wavefunctions of the two states, x is the deflection from the internuclear equilibrium distance during the vibration and $\hat{\mu}$ is the operator of the electric dipole moment. In the classical picture, one can imagine a temporary dipole moment, oscillating with a frequency υ at least for a short time, so it can interact with a photon of the same frequency υ [5]. By doing a Taylor expansion and considering only the first non-zero term of the approximation, on receives: [75]

$$\overrightarrow{R_v} = \frac{d\mu}{dx} \int \Psi_v'^* \, x \, \Psi_v'' \, dx \tag{2-27}$$

In the bra-ket notation, the transition dipole moment can be written as:

$$\overrightarrow{R_v} = \langle n|\hat{\mu}|m\rangle = \frac{d\mu_0}{dx} \langle n|\hat{x}|m\rangle, \tag{2-28}$$

where x is the coordinate of the vibrating bond and n, m are the quantum numbers of the respective states. The change of the static dipole moment $\frac{d\mu}{dx}$ when the bond is stretched or compressed, is also called the transition dipole strength and is a decisive factor for the peak intensity in the IR spectrum, whereas $\langle n|\hat{x}|m\rangle$ gives rise to the vibrational selections rules of $\Delta\upsilon = \pm 1$. [67] This equation reveals that the transition dipole moment will be nonzero, if $\frac{d\mu}{dx}$ and $\langle n|\hat{x}|m\rangle$ are nonzero. It shows the requirements that the dipole moment needs to change during the vibration ($\frac{d\mu}{dx} \neq 0$) and that transitions are only allowed between even functions, because only then $\langle n|\hat{x}|m\rangle \neq 0$.

2.2.3.2 Macroscopic Polarization

To describe the interaction of light with matter, one can imagine an electromagnetic wave $E(t)$, which exerts a force on the nuclei and the electron clouds of atoms or molecules. This induces a displacement of the nuclei and the electrons, creating induced dipole moments μ_{ind}. On a macroscopic average, the static dipole moment μ_0 is zero for most materials due to cancelling of static dipoles pointing in opposite directions. In contrast, the induced dipole moments do not necessarily cancel out but lead to the macroscopic polarization $\vec{P}$. Macroscopically this can be seen as the density of induced dipole moments: [5,70,74]

$$\vec{P} = \langle \mu_{ind} \rangle \, N = \sum \mu_{ind}, \tag{2-29}$$

where the polarization is the product of the number density N and the mean induced microscopic dipoles $\langle \mu_{ind} \rangle$, which can also be seen as the ensemble-averaged induced

dipole moments. This product is equal to the sum of all induced dipole moments μ_{ind}. The polarization, therefore, describes the average dipole moment per unit volume. [74]

For weak electric fields, one can find a linear relationship between the applied electric field strength $\vec{E}$ and the induced polarization $\vec{P}$: [74,76]

$$\vec{P}(t) = \varepsilon_0 \, \chi^{(1)} \, \vec{E}(t), \tag{2-30}$$

where ε_0 is the permittivity of the free space and $\chi^{(1)}$ is the linear susceptibility, which is material-specific and is a macroscopic average of the polarizability ($\mu_{ind} = \alpha \, \vec{E}(t)$, see equation (2-25)). This first-order susceptibility is a material-dependent constant, which is used to describe interactions between light and matter in linear spectroscopy. The macroscopic polarization can be seen as a nonequilibrium charge distribution created by the electric field and can be measured by detecting the emission field that was created by the oscillating time-dependent vibrational dipole (according to Maxwell's equations, compare to section 2.2.1).

To apply this to our system, which interacts with the electric field, we will consider the polarization quantum mechanically: [77]

$$P(t) = \langle \mu \, \rho(t) \rangle \tag{2-31}$$

With the dipole moment operator μ and the density matrix $\rho(t)$ (see chapter 2.3), which describes the system at the time t. By assuming that the radiation fields are weak compared to the electric fields in the molecules, we can use the perturbative expansion of the density matrix and get: [77]

$$P^{(n)}(t) = \int_0^\infty dt_n \int_0^\infty dt_{n-1} \dots \int_0^\infty dt_1 \, R^{(n)}(t_n, t_{n-1}, \dots, t_1) \times E(t - t_n) E(t - t_n - t_{n-1}) \dots E(t - t_n - t_{n-1} \dots - t_1), \tag{2-32}$$

where $R^{(n)}$ is the response function

$$R^{(n)}(t_n, t_{n-1}, \dots, t_1) = \left(\frac{i}{\hbar}\right)^n \langle \mu(t_n + \dots + t_1) \, [\mu(t_{n-1} + \dots + t_1), \dots \, [\mu(0), \rho(-\infty)(t)] \dots] \rangle. \tag{2-33}$$

In linear IR spectroscopy, the response is described by setting n=1. For Pump-Probe IR and 2D-IR spectroscopy, we need to choose n=3 as we need to consider a three times interaction with the electric field (see chapter 2.3). The measured quantity is the macroscopic polarization $P^{(n)}$ in order to extract the molecular response $R^{(n)}$. [67]

2.3 NONLINEAR INFRARED SPECTROSCOPY

If a strong electric field, like for instance laser light, is interacting with matter, nonlinear effects can occur. It means that the response of a material to an applied optical field depends nonlinearly on the strength of the optical field. Therefore, the macroscopic polarization (equation (2-30)) needs to be extended, and also higher-order terms need to be taken into account: [76]

$$\begin{aligned}\vec{P}(t) &= \varepsilon_0 \left(\chi^{(1)}\vec{E}(t) + \chi^{(2)}\,\vec{E}^{(2)}(t) + \chi^{(3)}\vec{E}^{(3)}(t) + \cdots \right) \\ &= \vec{P}^{(1)}(t) + \vec{P}^{(2)}(t) + \vec{P}^{(3)}(t) + \cdots ,\end{aligned} \tag{2-34}$$

where the second-order susceptibility $\chi^{(2)}$ and the third-order susceptibility $\chi^{(3)}$ are the higher-order terms, and the electric field $\vec{E}^{(n)}(t)$ implies a n-times interaction with the electric field. It can also be summarized as a sum of the first-order polarization $\vec{P}^{(1)}$, the second-order nonlinear polarization $\vec{P}^{(2)}$ and the third-order nonlinear polarization $\vec{P}^{(3)}$. For Pump-Probe IR and 2D-IR spectroscopy, which will be discussed in chapter 2.4 and chapter 2.5, the third-order nonlinear polarization $\vec{P}^{(3)}$ is the relevant term. [76]

To describe the interaction of an isolated molecule with a laser pulse, we will use a semi-classical approach, where we will describe the light-molecule interaction by considering the time-dependent electric field classically and the vibrational states of the molecule quantum mechanically. It is assumed that the molecule has two vibrational states, more specifically, the vibrational ground state $|0\rangle$ and the first vibrational excited state $|1\rangle$. The time evolution of the wavefunction $|\Psi\rangle$ of the molecule is described by the time-dependent Schrödinger equation: [67]

$$i\hbar\frac{\partial}{\partial t}|\Psi\rangle = \hat{H}\,|\Psi\rangle, \tag{2-35}$$

where ħ is the reduced Planck constant, t the time and $\hat{H}$ is the total Hamiltonian. It can be expressed as a sum of the time-independent Hamiltonian $\hat{H}_0$ of the isolated molecule and the operator $\hat{W}(t)$, which describes the interaction between the laser pulse and the molecule and can be considered as perturbation: [67]

$$\hat{H} = \hat{H}_0 + \hat{W}(t) \tag{2-36}$$

In the case of light-matter interaction, the interaction Hamiltonian is the product of the dipole moment operator $\hat{\mu}$ and an external electrostatic field $\vec{E}$: [67]

$$\hat{W}(t) = -\hat{\mu}\,\vec{E}(t) \tag{2-37}$$

Before the arrival of the pump pulse, the probability is very high that the molecule is in its vibrational ground state $|0\rangle$. In the absence of a laser pulse, there is no external electric field, so the interaction term will be zero ($\widehat{W}(t) = 0$). Upon the arrival of the laser pulse, the system will be in a linear combination of eigenstates, more specifically, the vibrational ground state $|0\rangle$ and the first vibrational excited state $|1\rangle$. For the wave-function of the two-state system results: [67]

$$|\Psi\rangle = c_0 e^{-\frac{iE_0 t}{\hbar}}|0\rangle + ic_1 e^{-\frac{iE_1 t}{\hbar}}|1\rangle \tag{2-38}$$

One can imagine that the laser pulse is pushing and pulling the charges, which leads to a vibration of the molecule. The molecules will be vibrating in phase and also synchronized to the phase of the laser pulse. During the laser pulse interaction with the molecule, the laser field will couple the molecular eigenstates, and the wavefunction is altered. The coefficients c_0 and c_1 are time-dependent in this case: [67]

$$\frac{\partial}{\partial t}\, c_1(t) = +\frac{i}{\hbar} c_0(t)\, e^{-i\omega_{01}t}\, \langle 1|\hat{\mu}|0\rangle\, E(t) \tag{2-39}$$

$$\frac{\partial}{\partial t}\, c_0(t) = +\frac{i}{\hbar} c_1(t)\, e^{+i\omega_{01}t}\, \langle 0|\hat{\mu}|1\rangle\, E(t), \tag{2-40}$$

where $\frac{\partial}{\partial t}\, c_1(t)$ and $\frac{\partial}{\partial t}\, c_0(t)$ are the time-dependent coefficients of the states $|0\rangle$ and $|1\rangle$, which become time-dependent as a result of the interaction of the laser pulse with the molecule. They can be seen as a weight of the wavefunction in which state the system is present, indicating how many molecules are in the ground state and in the first vibrational excited state, respectively. Here, the energy difference between the two states is defined as $\omega_{01} = \frac{E_1 - E_0}{\hbar}$. [67] The change of the coefficients over time $\frac{\partial}{\partial t}\, c_1(t)$ and $\frac{\partial}{\partial t}\, c_0(t)$ depends on the transition dipole moment $\langle 1|\hat{\mu}|0\rangle$ and $\langle 0|\hat{\mu}|1\rangle$, which are shown here in the bra-ket notation (see chapter 2.2.3.1). The term $\langle 0|\hat{\mu}|1\rangle$ is oscillating at the frequency difference of the two eigenstates and will emit an electric field at the fundamental frequency of the vibrator. In a classical picture, the charges oscillating at the vibrational frequency create the emitted field, which is consistent with Maxwell's equations. In a quantum mechanical picture, the coherent superposition of eigenstates creates the macroscopic polarization (see chapter 2.2.3.2). The coefficients can be used to arrange the density matrix, which is defined as:

$$\rho = \begin{pmatrix} \rho_{00} & \rho_{01} \\ \rho_{10} & \rho_{11} \end{pmatrix} = \begin{pmatrix} \langle c_0'(t) c_0'^*(t)\rangle & \langle c_0'(t) c_1'^*(t)\rangle \\ \langle c_1'(t) c_0'^*(t)\rangle & \langle c_1'(t) c_1'^*(t)\rangle \end{pmatrix}, \tag{2-41}$$

with $c_0'(t) = c_0(t)$, $c_1'(t) = ic_1(t)$ and $c_0'^*(t)$ and $c_1'^*(t)$ are the complex conjugates. The off-diagonal density matrix elements ρ_{01} and ρ_{10} are called coherences and the diagonal density matrix elements ρ_{00} and ρ_{11} are called populations. One can see that both coefficients need to be changed to create a population in the first vibrational excited state. Therefore, two interactions with the electromagnetic field of the pump pulse are

required, where the first one creates a polarization and the second one creates a population in the first vibrational excited state.

The off-diagonal density matrix elements ρ_{01} and ρ_{10} can be seen as a linear superposition of eigenstates created by the laser pulse. They are the relevant terms, which are responsible for the time-dependent vibrational dipole. In fact, the coherences are the origin of the signal which can be detected, as they oscillate with the frequency ω_{01} around the z-axis, which leads to the emission of an electric field $E_{sig}(t)$. With increasing time after the interaction with the laser pulse, the matrix elements ρ_{01} and ρ_{10} will decay due to homogenous dephasing, because the molecules will have different oscillatory frequencies, which leads to destructive interference. By using the homogeneous dephasing time T_2, we obtain for the density matrix elements ρ_{01} and ρ_{10}

$$\rho_{01}(t) = -c_0 c_1 e^{+i\omega_{01}t} e^{-\frac{t}{T_2}} \tag{2-42}$$

$$\rho_{10}(t) = i c_0 c_1 e^{-i\omega_{01}t} e^{-\frac{t}{T_2}}. \tag{2-43}$$

The diagonal density matrix elements ρ_{00} and ρ_{11} correspond to the population of the ground state $|0\rangle$ and to the population of the first vibrational excited state $|1\rangle$, respectively. With progressing time after the excitation of the laser pulse, population relaxation will occur. This means that due to energy transfer, the diagonal element ρ_{11} will decay back to the vibrational ground state with the population relaxation time constant T_1, whereas the ground state ρ_{00} is refilled from the excited state:

$$\rho_{11}(t) = \rho_{11}(0)\, e^{-\frac{t}{T_1}} \tag{2-44}$$

$$\rho_{00} = 1 - \rho_{11}(t). \tag{2-45}$$

The homogeneous dephasing time T_2 and the population relaxation T_1 time are linked by

$$\frac{1}{T_2} = \frac{1}{2T_1} + \frac{1}{T_2^*}, \tag{2-46}$$

where T_2^* is the pure dephasing time caused by fluctuations of the environment.

In a Bloch vectorial picture, one can visualize the quantum mechanical coherences, populations, and the macroscopic polarization by using a vector diagram. Therefore, we look at the vector of a dipole of a single molecule, which is in a coherent superposition of two states (see eq. (2-38)) and plot it in a coordinate system (*Figure 2-4*).

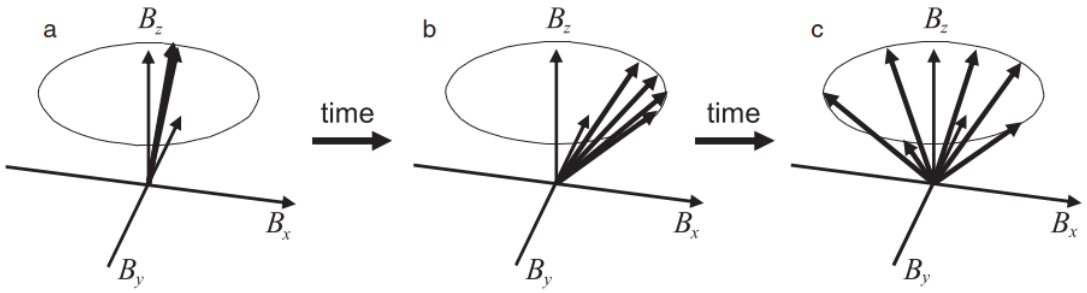

Figure 2-4: Bloch vectorial picture for an ensemble of molecules with the same coefficients $\boldsymbol{c_0}$ *and* $\boldsymbol{c_1}$*, but different frequencies. (a) At* $\boldsymbol{t = 0}$ *the vectors lie in the (y,z)-plane, giving rise to constructive interference. (b) With increasing time, the projections onto the* $\boldsymbol{B_x}$ *axis start to differ, which leads to destructive interference. (c) At some point, the vectors are completely randomized and the projections onto the* $\boldsymbol{B_x}$ *axis will sum to zero. Reproduced from 'Concepts and Methods of 2D Infrared Spectroscopy' by Peter Hamm and Martin Zanni. Copyright P. Hamm and M. Zanni 2011. Reproduced with permission of the Licensor through PLSclear.* [67]

The three components of the so-called Bloch vector are defined as: [67]

$$B_z(t) = c_0(t)c_0^*(t) - c_1(t)c_1^*(t) \tag{2-47}$$

$$B_x(t) = i\big(c_0(t)c_1^*(t) - c_0^*(t)c_1(t)\big) = c_0c_1\sin(\omega_{01}t) \tag{2-48}$$

$$B_y(t) = c_0(t)c_1^*(t) + c_0^*(t)c_1(t) = c_0c_1\cos(\omega_{01}t), \tag{2-49}$$

with the coefficients $c_0(t)$ and $c_1(t)$ being time-dependent, which gives rise to the vectors shown in *Figure 2-4a*. When the laser pulse arrives, it pushes the vector towards the x,y-plane and with progressing time, it will precess around the z-axis (compare to equations (2-48) and (2-49)). This rotation is responsible for the emission of the signal field and the macroscopic polarization can be calculated from equation (2-48), as $P(t) \propto B_x(t)$. The vectors B_x and B_y correspond to the coherence of a state, as the superposition of two states corresponds to a vector, which is rotating in the (x,y)-plane, whereas the deviation of B_z from 1 corresponds to the population of a state. In reality, the sample consists of an ensemble of molecules, which slightly differ in their vibrational frequencies, giving rise to an individual Bloch vector, respectively. Therefore, the macroscopic polarization is the ensemble average of the projections onto the B_x axis: [67]

$$\vec{P}(t) = \langle\mu\rangle = \langle B_x\rangle = i(\langle c_0(t)c_1^*(t)\rangle - \langle c_0^*(t)c_1(t)\rangle), \tag{2-50}$$

where $\langle \dots \rangle$ indicates the ensemble average. At $t = 0$ the electric fields generated by the individual molecules will constructively interfere.

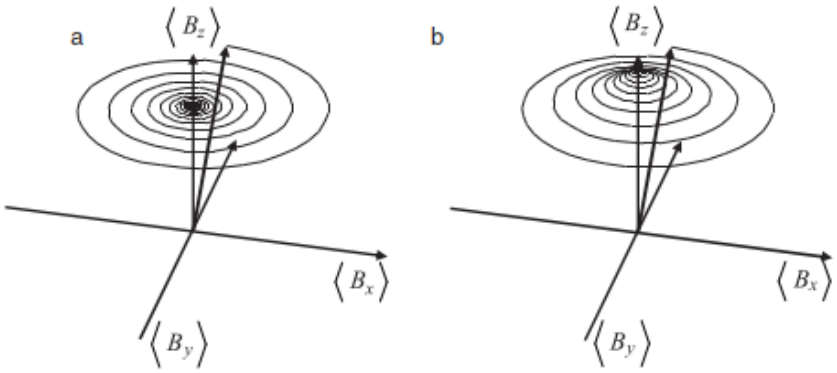

Figure 2-5: Bloch vectorial picture for an ensemble of molecules, where the averaged vector is shown. (a) By only including dephasing, the vector will spiral towards the B_z axis. (b) By additional including population relaxation, the vector will also converge to $B_x = 1$. Reproduced from 'Concepts and Methods of 2D Infrared Spectroscopy' by Peter Hamm and Martin Zanni. Copyright P. Hamm and M. Zanni 2011. Reproduced with permission of the Licensor through PLSclear. [67]

However, as time progresses, their projections onto the B_x axis will differ, leading to destructive interference. The averaged vector of the individual molecules that is responsible for the macroscopic polarization is shown in *Figure 2-5*. The destructive interference leads to a loss of the macroscopic polarization with progressing time. The macroscopic polarization will decay with time due to homogenous and inhomogeneous dynamics. By only considering dephasing, the vector will spiral towards the z-axis as the projection on the x- and y-axis decays (*Figure 2-5a*), due to destructive interference and the decrease of the macroscopic polarization.

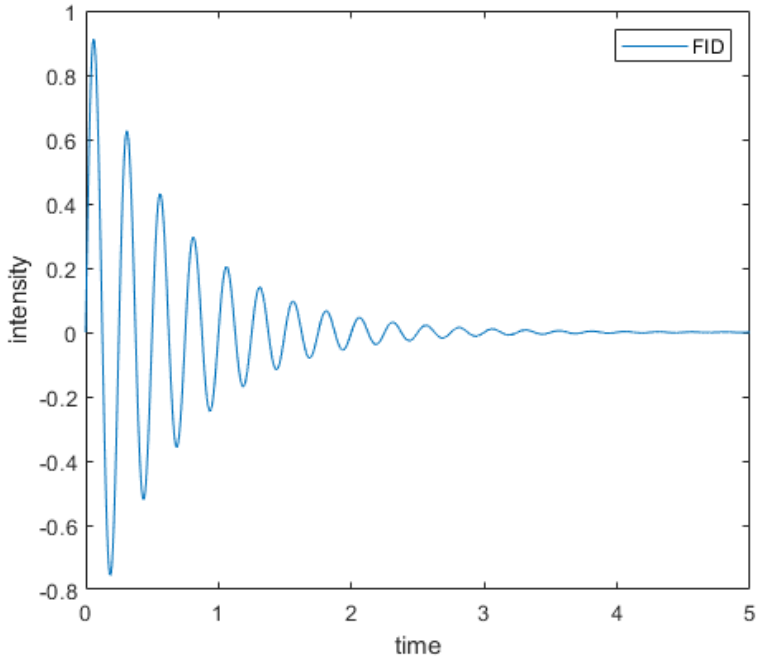

Figure 2-6: Schematic picture of the free induction decay (FID) for the response of a sample at one probe frequency as a function of the dephasing time.

By also including population relaxation, the z-component will increase additionally until it reaches B_z=1 (*Figure 2-5b*). Due to this precessional motion of the vector of the macroscopic polarization, the emitted signal field (FID), which is detected, will oscillate with time, and it will also decay with time due to the population relaxation and the dephasing (*Figure 2-6*). The coherences and population relaxations can be investigated by non-linear spectroscopy, e.g. Pump-Probe IR spectroscopy and 2D-IR spectroscopy, which will be explained in more detail in the next chapter.

2.4 PUMP-PROBE IR SPECTROSCOPY

Ultrafast infrared pump-probe (Pump-Probe IR) spectroscopy enables to monitor the coherences of the ground state and the first vibrational excited state and of the first and the second vibrational excited state. It enables to investigate the population relaxation (=vibrational energy relaxation) from the first vibrational excited state to the ground state. This can be done by using an ultrashort IR pump pulse, which excites a molecular vibration from the ground state to the first vibrational excited state (*Figure 2-7a*). The resonant interaction of one oscillator with the laser pulse (two interactions with the electric field) creates a population in the first vibrational excited state. With a variable time delay τ, a second laser pulse (probe pulse) arrives at the sample to probe the population of the first vibrational excited state. This can either lead to an excited state absorption ($|1\rangle \rightarrow |2\rangle$) or to a stimulated emission ($|1\rangle \rightarrow |0\rangle$). The moment at which both pulses appear simultaneously at the sample is called time zero. The excited state population will decay to the ground state with increasing time due to the energy relaxation. This process can be monitored with the probe pulse. Typically, every second spectrum is measured without a pump pulse, which enables to plot the transmission difference of the pumped and the unpumped spectrum. The transient signal $\Delta\alpha$ can be determined with:

$$\Delta\alpha = -\ln\left(\frac{T(\omega)}{T_0(\omega)}\right), \tag{2-51}$$

where $T(\omega)$ is the signal of the pumped spectrum and $T_0(\omega)$ is the signal of the unpumped spectrum. The negative transient signal appears in the spectrum due to the stimulated emission ($|1\rangle$ to $|0\rangle$) and that there are fewer molecules in the vibrational ground state, as before the excitation of the pump pulse (ground state bleach) (*Figure 2-7b*). The excited-state absorption (ESA) has a positive sign because the transition from the first to the second vibrational excited state can only occur in the case of the pumped spectrum, when the first vibrational excited state is populated. Assuming that we consider an anharmonic potential, the signal of the ESA is red-shifted compared to the

signal of the bleach, because the transition energy of $|1\rangle$ to $|2\rangle$ is lower than the transition energy of $|0\rangle$ to $|1\rangle$. [57]

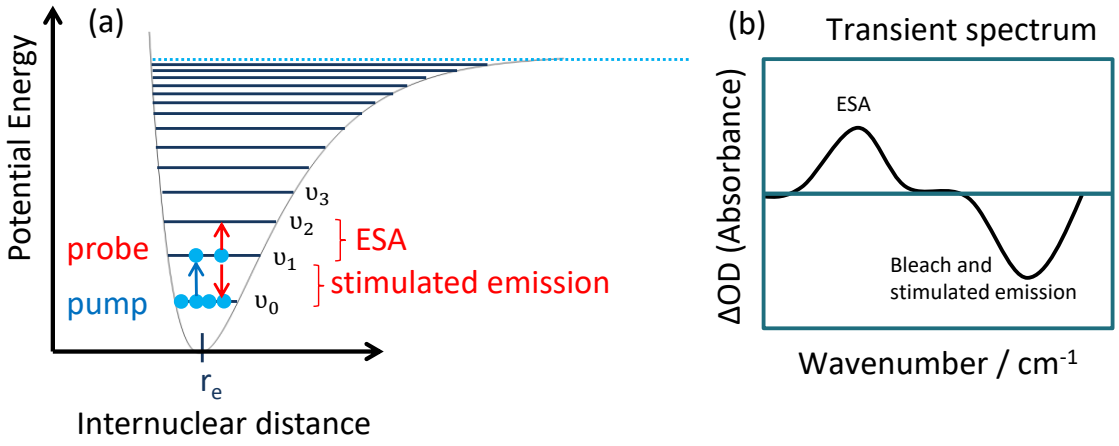

Figure 2-7: Basic principle of pump-probe spectroscopy. (a) The anharmonic potential of the vibration is shown, where most molecules are in the vibrational ground state. Interaction with the pump pulse creates a population in the first vibrational excited state (blue arrow). The probe pulse can lead to an excited state absorption (ESA, $|1\rangle$ to $|2\rangle$) or to stimulated emission ($|1\rangle$ to $|0\rangle$)(red arrows). (b) In the resulting transient spectrum, a negative peak can be observed at the spectral position of the vibrational band due to the bleach and the stimulated emission. The red-shifted positive peak results from the ESA.

The time delay between pump and probe pulse can be changed with a delay stage in the pump path, by changing the path length of the laser beam. With increasing delay time between pump and probe pulse, the excited state will relax to the ground state and the modulated signal in the transient spectrum will decrease. From this decay, the population energy relaxation can be determined. The time and the probe frequency resolution of this method are quite good; hence it only allows to measure the response with a broadband excitation. To receive also a resolution along the pump frequency axis, one needs to use a pump excitation pulse, which is narrow in frequency. This can, for instance, be achieved with 2D-IR spectroscopy and will be explained in more detail in the following chapter.

2.5 2D-IR Spectroscopy

Two-dimensional infrared (2D-IR) spectroscopy is similar to pump-probe spectroscopy, but one will obtain an additional resolution along the pump frequency axis, which enables one to gain more structural information, not accessible with pump-probe spectroscopy: for instance, vibrational couplings and line shapes. The response of the

system is studied by selectively exciting the vibrational modes and plotting them as a function of the pump and the probe frequencies. Therefore, the probe frequency is measured in the frequency-domain, by spectrally dispersing it in a spectrograph, but the pump frequency can be resolved by measuring it in the frequency-domain or in the time-domain. Measuring in the frequency-domain requires a pump pulse, which is narrow in frequency, to selectively excite the different frequencies. One can envision that for each of the narrow pump frequencies, the whole probe frequency range is measured, so it is like a pump-probe measurement, where the whole probe frequency range is monitored for each of the narrow pump pulses. The center frequency of the pump pulse is then scanned through the frequency range of interest. When the narrow pump frequency is equal to the resonance frequency of an oscillator, it is excited, and a signal can be detected. The requirement that the pump pulse needs to be narrow in frequency, leads to the fact that it will be stretched in time (a picosecond pulse instead of a femtosecond pulse). That involves the problem that one loses temporal resolution as the pump pulse will be in the picosecond range. To overcome this problem, one can resolve the pump pulse by measuring it in the time-domain and replacing the picosecond (but narrow in frequency) pump pulse by two pump pulses which are short in time but broad in frequency, so that all resonance frequencies of the sample are contained in each of the two pump pulses. Conceptually, this means that we choose two narrow pump pulses in the time-domain, and vary their time delay. By changing the temporal spacing between the two narrow pump pulses (in the time domain), the corresponding period of the sinusoidal wave in the frequency domain will change. The period of the sinusoidal wave is inversely proportional to the time delay between the two femtosecond pump pulses in the time domain. By scanning different time delays of the femtosecond pulses, one always brings different sets of frequencies in resonance. Finally, a Fourier transformation will convert our time-domain response to the frequency-domain, which gives us the second dimension for the 2D-IR spectrum – the pump frequency axis – and where we will observe a signal from the excited oscillators. [67]

Along the diagonal in a 2D-IR spectrum, the pump frequency is equal to the probe frequency (*Figure 2-8*). Oscillators, which are excited at their resonance frequency, will appear on this diagonal with a negative peak (blue) due to the ground state bleach and stimulated emission. Red-shifted to the ground state bleach (along the probe frequency axis), one will observe (similar to pump-probe IR spectroscopy) a positive peak (red) due to the excited state absorption, which is present at the same pump frequency as the bleach, but at lower probe frequencies, due to the anharmonicity of the potential. Changing the delay time between pump and probe pulse, typically referred to as waiting time, enables measurement of the 2D-IR spectra time-dependent. Hence, it is possible to collect the response of the system as a function of the pump and the probe frequency for each desired waiting time.

By taking a look at the diagonal peaks in a 2D-IR spectrum, one will notice the advantages over Pump-Probe IR spectroscopy, which is getting information about spectral diffusion and about the broadening of a peak, for instance, if the vibration is

inhomogeneously broadened. If there is a diagonally elongated peak along the diagonal present at early waiting times, the vibrational band is inhomogeneously broadened (*Figure 2-8b*).

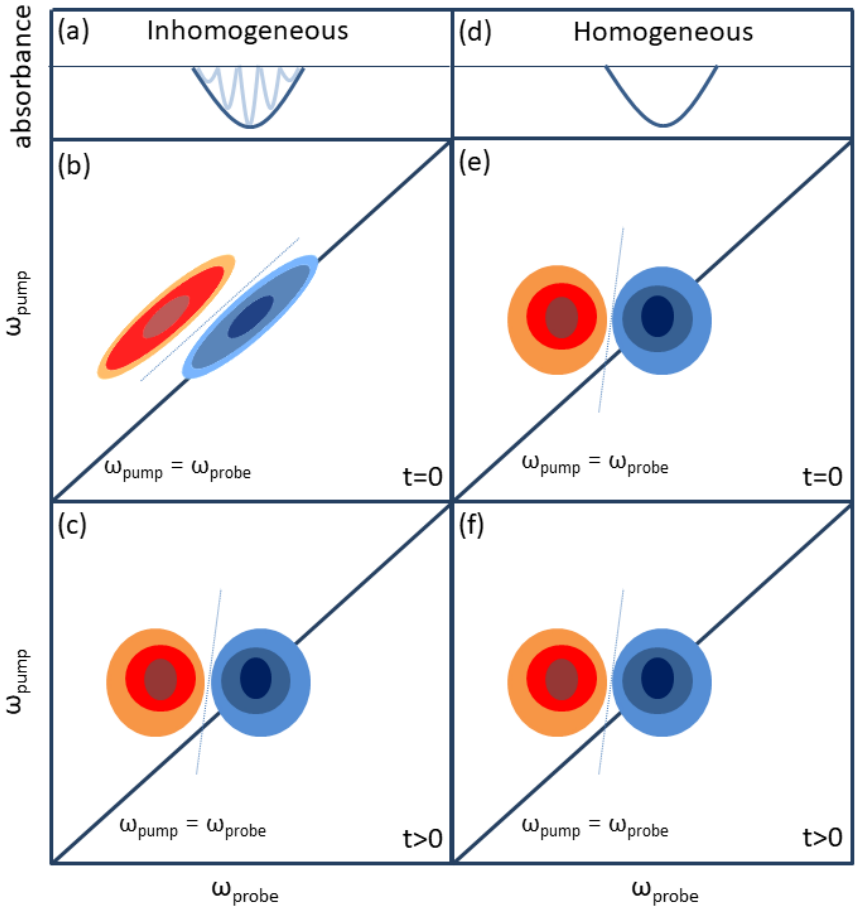

Figure 2-8: (a), (d) FT-IR spectra of an inhomogeneously and a homogeneously broadened band look quite similar. 2D-IR spectrum of an inhomogeneously broadened band at an early waiting time (b) reveals an elongation along the diagonal and gets more roundish at later waiting times (c). 2D-IR spectrum of a homogeneously broadened band reveals a round shape already at early waiting times (e) and will stay roundish also at later waiting times (f).

It means that one kind of oscillator is present in different local environments, whereby the frequency of each oscillator is slightly altered. More specifically, the band consists of many small bands, which represent the oscillator in different environments. A prominent example is water: water will reveal a rather broad distribution of different hydrogen-bonded geometries, which leads to a distribution of different vibrational frequencies. [78,79] By exciting with a narrow pump pulse, only a small subensemble of molecules, the excited molecules, will own similar hydrogen-bond lengths and angles and therefore similar vibrational frequencies. But different subensembles might have different vibrational frequencies. With increasing waiting time, the oscillators will have time to rearrange, which means that they move into different environments, e.g. they

will exhibit different hydrogen-bond lengths and angles, which results in a shift in their resonance frequency. This phenomenon is called „spectral diffusion“, which causes the peak to get more spherical with increasing waiting time (*Figure 2-8c*). If there is only one kind of oscillator and all of them are located in the same local environment, a round peak on the diagonal is already observed for early waiting times (*Figure 2-8e*) and will stay spherical also at later waiting times (*Figure 2-8f*). This is called homogenous broadening and can be imagined as the intrinsic lifetime, which cannot be smaller than determined by the vibrational relaxation. At early waiting times, the homogenous and the inhomogenous linewidths can be determined, as there the difference between homogeneous and inhomogeneous broadening is most prominent, because the oscillators did not have the time to reorient: for the inhomogeneous linewidths, one takes the diagonal cut along the diagonal of the 2D-IR spectrum and for the homogenous linewidths, one takes the cut perpendicular to the diagonal and through the minimum of the bleach of the 2D-IR. [80]

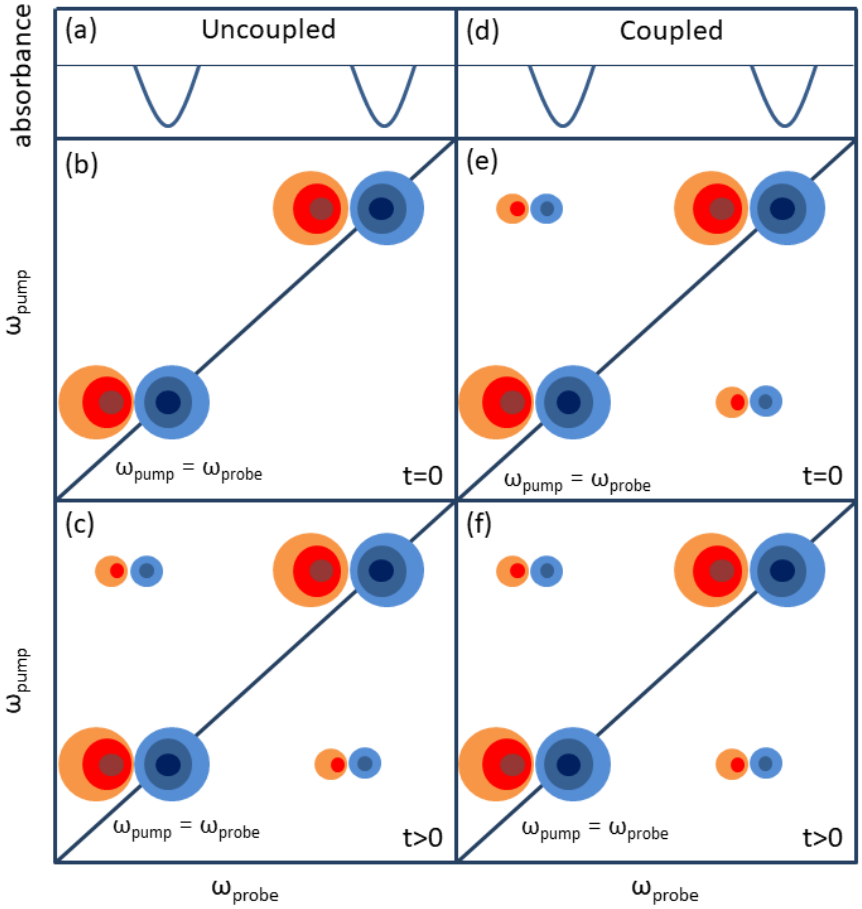

Figure 2-9: (a), (d) FT-IR spectra of two oscillators, which are homogeneously broadened. (b) At early waiting times, the 2D-IR spectrum reveals two bleaches (blue) on the diagonal at the spectral position of the vibration and two red-shifted excited state absorptions (red). (c) At later waiting times two cross-peaks appear due to chemical exchange. (e), (f) In case the two oscillators are coupled, the cross-peaks will already be present at early waiting times and will also stay at later waiting times.

Additional information, which can be extracted from a 2D-IR spectrum are contained in cross-peaks (*Figure 2-9*). If cross-peaks are present, they will always appear between two diagonal peaks, but their origin can be different: they can be caused by coupling or by population transfer (e.g. chemical exchange). If we look at two coupled oscillators, where oscillator A gives rise to a diagonal peak at its resonance frequency $\omega_A = \omega_{Pump,A} = \omega_{Probe,A}$ and oscillator B gives rise to a diagonal peak at its resonance frequency $\omega_B = \omega_{Pump,B} = \omega_{Probe,B}$, then we will observe two cross-peaks at $\omega_{Pump,A} = \omega_{Probe,B}$ and $\omega_{Pump,B} = \omega_{Probe,A}$, respectively. Therefore, the excitation at the resonance frequency of oscillator A will result in the appearance of an off-diagonal peak at the resonance frequency of oscillator B.

The cross-peak is located at the same pump frequency as oscillator A, but at the probe frequency of the resonance of oscillator B. Hence, the two oscillators are not independent of each other. In the following, we describe the principles from which the cross-peaks can arise. If the cross-peaks already exist at time zero, their presence is caused by coupling (*Figure 2-9e,f*). It means that an excited molecule interacts with a similar molecule in close proximity (not a solvent molecule), which is typically called an exciton state. It can be imagined that the charges of the electrons and the nuclei create an electrostatic potential, which surrounds the molecule. If two molecules are close enough, their potentials will influence each other and will alter their molecular orbitals and their vibrational frequencies will shift. Therefore, the transition frequency of one oscillator depends on the excitation level of the other oscillator. This so-called transition-dipole coupling is frequently observed within a molecule, e.g., between the symmetric and the antisymmetric N-D_2 stretching vibration. The coupling between the two modes is determined by the potential energy surface $V(r_i, r_j)$, which is a sum of the potentials $V_i(r_i)$ and $V_j(r_j)$ and the coupling constant $ß_{ij}$ and is given in the weak coupling limit as: [67,81,82]

$$V(r_i, r_j) = V_i(r_i) + V_j(r_j) + ß_{ij} r_i r_j. \tag{2-52}$$

The simplest model that relates the coupling constant $ß_{ij}$ to the structure is the model of the transition-dipole coupling, which can be used to calculate the coupling between the two modes: [67,81,82]

$$ß_{ij} = \frac{1}{4\pi\varepsilon_0}\left(\frac{\overrightarrow{\mu_i}\cdot\overrightarrow{\mu_j}}{r_{ij}^3} - 3\frac{(\overrightarrow{r_{ij}}\cdot\overrightarrow{\mu_i})(\overrightarrow{r_{ij}}\cdot\overrightarrow{\mu_j})}{r_{ij}^5}\right), \tag{2-53}$$

where $\overrightarrow{\mu_i}$ and $\overrightarrow{\mu_j}$ are the directions of the transition dipoles, r_{ij}^3 are the vectors, which connect the two sites. [67,81,82]

In some cases, the cross-peaks are not there at time zero, but they appear at later waiting times (*Figure 2-9b,c*). That can be caused by energy transfer (or population transfer) or by chemical exchange. Energy transfer means, that the excited oscillator

loses energy and another oscillator in close proximity, which has a different resonance frequency, receives the energy. Mostly this energy transfer occurs downhill. It is mediated by a constantly changing local environment, which leads to a pushing and pulling of the molecules, resulting in a deformation of the potential energy surface and thus a change of the vibrational frequencies. After excitation, resonance energy transfer can lead to a movement of the excited state of a molecule to another oscillator, which results in a flip of the quantum states. For instance, population transfer reveals an excited population state $|1\rangle_{aa}\langle 1|$, which flips to another excited population state $|1\rangle_{bb}\langle 1|$. In this mechanism no photons are emitted; it is a non-radiative process and reduces the lifetime of the excited state α. The energy transfer can occur intra- or intermolecularly, but is mediated by a quantum-mechanical coupling between the two modes. [67,81,82]

In the case of chemical exchange, there are two states, which are separated by a reaction barrier (e.g., from bound to unbound or from isomer A to isomer B), the probability of finding the molecule in the transition state is very low. Therefore, at time zero, the two oscillators will be either in state A or in state B, giving rise to two signals on the diagonal. At later waiting times, some of the oscillators will be converted to the other state, for instance, a molecule that was pumped with a hydrogen-bond might be probed without a hydrogen-bond, giving rise to two cross-peaks at later waiting times. The change of the environment of the excited oscillator will result in a change in its resonance frequency. In the limit that there is no reaction barrier, but rather a broad distribution of hydrogen-bond environments, the single oscillators cannot be resolved in the 2D-IR spectrum, as they lie quite close in frequency. That results in the appearance of an elongated peak along the diagonal. With increasing waiting time, the oscillators move to different hydrogen-bonded environments causing the peak to get more roundish. This is called spectral diffusion and the emerging round peak can be seen as a superposition of many emerging cross-peaks. [67,81,82]

2.6 Nuclear Magnetic Resonance Spectroscopy

In Nuclear Magnetic Resonance (NMR) spectroscopy, the split spin states of a nucleus are probed with a radiofrequency pulse in an external magnetic field. The technique can be used to obtain information about the electronic environment of a nucleus, as nuclei in different electronic environments will be shielded differently, which results in different resonance frequencies. It enables to determine the chemical structure, by taking into account the different electron densities of different chemical bonds. The theoretical principle of NMR spectroscopy is explained in the following. [5] Nuclei of certain isotopes possess an intrinsic spin, which can be associated with the angular momentum $\vec{L}$. It can only adopt certain values, which means that it is quantized and it depends directly on the magnetic quantum number m: [83]

$$|\vec{L}| = \frac{h}{2\pi} m\,, \tag{2-54}$$

with the Planck constant h. The magnetic quantum number is related to the nuclear spin quantum number I, which is determined by the respective nucleus (only nuclei with a spin-quantum number of $I > 0$ will be NMR-active): [83]

$$m = 2I + 1 \tag{2-55}$$

More specifically, the spin quantum number I indicates the number of energy states of a nucleus in an external magnetic field. For instance, for a proton with nuclear spin quantum number $\frac{1}{2}$, the magnetic quantum number will be $m = 2$. It means that the proton has two different magnetic quantum numbers, spanning the range from $-I$ to $+I$ with $\Delta m = 1$ (including zero for integer quantum numbers). Consequently, we obtain for the proton $m_1 = +\frac{1}{2}$ and $m_2 = -\frac{1}{2}$. One can imagine that the spin has two different alignments in a static magnetic field, corresponding to m_1 and m_2. Nuclei with an angular momentum will also have a magnetic (dipole) moment $\vec{\mu}_M$: [83]

$$\vec{\mu}_M = \gamma\, \vec{L}, \tag{2-56}$$

with the gyromagnetic ratio γ, which is a constant specific to the respective nucleus. [83] By placing the nucleus in an external static magnetic field $\vec{H}_0$, some spins will align parallel and some other spins will align antiparallel to the external field. Consequently, the two degenerate spin states split into a high-energy spin state and a low-energy spin state. This splitting of energy states under the influence of a magnetic field (caused by the interaction of the external magnetic field and the magnetic moment of the nucleus) is called the Zeeman-effect. [5] The potential energy E of the nucleus in the magnetic field is given by:

$$E = \vec{\mu}_M \vec{H}_0, \tag{2-57}$$

with the static magnetic field $\vec{H}_0$ and the magnetic dipole moment of the nuclei $\vec{\mu}_M$. By taking into account equations (2-54) and (2-56), the equation can be rearranged to: [83]

$$E = \frac{\gamma h \vec{H}_0}{2\pi} m. \tag{2-58}$$

As the gyromagnetic ratio γ is nuclei specific, the Planck constant h is a constant and – in this approach – the strength of the magnetic field $\vec{H}_0$ is not varied, the energy of a magnetic dipole in a static magnetic field only depends on the magnetic quantum number m. The proton exhibits magnetic quantum numbers of $m_1 = +\frac{1}{2}$ and $m_2 = -\frac{1}{2}$, which enables to calculate the potential energies E_1 and E_2 (by inserting the magnetic

quantum number m into equation ((2-58) and their energy difference ΔE between the high energy state and the low energy state: [83]

$$\Delta E = \frac{\gamma h \vec{H}_0}{2\pi}. \tag{2-59}$$

In NMR spectroscopy, the nuclei are irradiated with electromagnetic radiation (a radiofrequency pulse), leading to energy absorption, and the lower energy state will flip to the higher energy state. The nuclei are in resonance with the electromagnetic radiation. Therefore, it is important to know the exact energy difference between the two states. For a given nucleus with the gyromagnetic ratio γ, the energy difference between the states only depends on the magnetic field $\vec{H}_0$: an increased strength of the magnetic field will lead to an increase in the energy difference between the states. By equating equation ((2-2), which describes the propagation of light (here the radiofrequency), with equation ((2-59), we find the fundamental NMR equation. It is valid for an isolated nucleus and represents the radiofrequency υ (that can also be expressed as the angular velocity ω_0), which is needed for the energy transition between the two states for a given nucleus with the gyromagnetic ratio γ and the magnetic field $\vec{H}_0$: [83,84]

$$\upsilon = \frac{\omega_0}{2\pi} = -\frac{\gamma \vec{H}_0}{2\pi} \tag{2-60}$$

Hence, the radiofrequency υ is the resonance frequency, which is required to excite the nucleus from the lower spin state to the higher spin state and depends (for a given nucleus) on the magnetic field $\vec{H}_0$. For a given nucleus, equation (2-60) reveals, that there are two parameters, which can be varied: the radiofrequency υ and the magnetic field $\vec{H}_0$. Therefore, two methods for measuring are possible. The first method is the frequency sweep method, where the magnetic field strength is kept constant, and the radiofrequency is varied until resonance is achieved. In the second method, the field-sweep method, the frequency is kept constant, while the magnetic field strength is varied. Both methods are called continuous-wave (CW) spectrometry, as one parameter is varied, while the other parameter is kept constant. Nowadays, mostly pulsed Fourier-transform (FT) instruments are used, due to higher sensitivity and faster collection time.[5] This can be achieved by simultaneously exciting all of the nuclei. Therefore, a short pulse is needed, which contains various frequencies, in order to excite the different types of nuclei simultaneously.

To achieve a resonant transition from the lower to the higher energy state, the population of the energy levels needs to be different. According to the Boltzmann distribution, this is possible, as, in thermal equilibrium within the magnetic field, the number of nuclei, which populate the lower energy level, will be larger than the number

of nuclei, which populate the higher energy level. The Boltzmann distribution indicates the ratio of the number of nuclei in the excited spin state α (N_α) to the number of the nuclei in the ground spin state ß ($N_ß$): [83]

$$\frac{N_\alpha}{N_ß} = e^{-\frac{\Delta E}{k_B T}}, \tag{2-61}$$

with the Boltzmann constant k_B, the temperature T and the energy difference between the two states ΔE. By inserting equation ((2-59), we find: [5,83]

$$\frac{N_\alpha}{N_ß} = e^{-\frac{\gamma h \vec{H}_0}{2\pi k_B T}} \tag{2-62}$$

$$N_\alpha - N_ß \approx e^{-\frac{N\gamma h \vec{H}_0}{k_B T}}. \tag{2-63}$$

The energy difference between the two states is small, which results also in a very small population difference ($N_\alpha - N_ß$). As the transition probability increases with a larger population excess of the lower energy level, a way to increase the signal strength is by increasing the magnetic field $\vec{H}_0$. This leads to an increased energy difference between the two states. Consequently, the population of the lower energy state will also increase, as well as the transition probability [83]. However, an increased magnetic field strength $\vec{H}_0$ will also lead to a larger transition frequency υ. As NMR spectrometers with different magnetic field strengths are available, it is necessary to introduce the chemical shift δ as an independent scale for the shielding. For ^{1}H-NMR spectroscopy, it is quite common to use Tetramethylsilane (TMS) as specified standard, which will exhibit for a given magnetic field strength a peak at a certain position that is defined as $\delta = 0\ ppm$ (parts per million). The chemical shift is defined as the frequency difference between the sample υ_{sample} and the TMS υ_{TMS}, divided through the frequency of the spectrometer $\upsilon_{Spectrometer}$: [84,85]

$$\delta = \frac{\upsilon_{sample} - \upsilon_{TMS}}{\upsilon_{Spectrometer}} \cdot 10^6 \tag{2-64}$$

The division through the frequency of the spectrometer results in a scale, that is also independent of the magnetic field strength and therefore enables to compare measured samples independent of the used NMR spectrometer and the used magnetic field strength. As the chemical shift difference is small compared to the frequency of the spectrometer, the factor 10^6 is multiplied to obtain simpler numerical values. The chemical shift δ is then expressed in parts per million (ppm). [5,85]

In practice, not all protons have the same resonance frequency and chemical shift. According to equation (2-59), the resonance frequency only depends on the magnetic field $\vec{H}_0$ and the gyromagnetic constant γ. However, the magnetic field $\vec{H}_0$ is kept constant and the gyromagnetic constant γ is nuclei specific. Hence, the reason for

different resonance frequencies of a given nucleus is that they are located in different chemical environments, where they are exposed to different magnetic fields. It means that the external magnetic field $\vec{H}_0$ is not equal to the local magnetic field. The different magnetic fields are a consequence of the electrons, which are surrounding the nucleus. The electrons are charges, whereby the applied magnetic field induces currents in the electron cloud and according to Lenz's law an opposed induced magnetic field is created. Consequently, the induced magnetic field reduces the field strength of the external magnetic field around the nucleus. This is called shielding. Therefore, the nucleus will be exposed to an effective magnetic field H_{eff}, which is the opposed induced magnetic field ($H_{ind} = \sigma H_0$) subtracted from the external magnetic field H_0: [85]

$$H_{eff} = H_0 - \sigma H_0, \tag{2-65}$$

where σ is the shielding constant and its value depends on the electron density around the nucleus. Hence, the resonance frequency is determined by the shielding constant, which is the result of the protons residing in different chemical environments. Vice versa, the resonance frequency, observed in NMR spectroscopy contains information about the chemical environment of the nucleus. [85] Therefore, the resonance condition for nuclei of the same type, which are located in different chemical environments, are different. This means that resonance occurs at different frequencies, and for nuclei located in a shielded external magnetic field, equation ((2-60) needs to be modified to: [5]

$$\upsilon_L = \frac{\gamma H_{eff}}{2\pi} = (1-\sigma)\frac{\gamma H_0}{2\pi}, \tag{2-66}$$

where υ_L is the Larmor frequency. It is the frequency at which nuclei rotate around the axis of the applied magnetic field and at which resonance occurs. This precessional motion is caused by the interaction of the external magnetic field with the magnetic moment of the nucleus because the magnetic moment is forced to align with the direction of the magnetic field and experiences a torsional movement. Together with the angular momentum of the nucleus, this causes the precessional motion around the axis of the magnetic field. As not all nuclei rotate in phase, the nuclear magnetic moments are randomly distributed over a conical area, and a net magnetization vector M_0 can be introduced, which describes the net magnetization in the z-direction. Parallel and antiparallel aligned nuclei experience both this precessional motion, but in opposite directions and along the +z axis and along the –z axis, respectively. From the Boltzmann distribution, it is known, that there is a slight excess of parallel aligned nuclei. Therefore, parallel and antiparallel aligned nuclei do not cancel out, instead a net magnetic moment M_0 remains along the z-axis in the parallel aligned direction (see *Figure 2-10*). By using a radiofrequency pulse, a resonant interaction can be observed, if the frequency of the rotating magnetic field of the rf field is equal to the Larmor frequency of the nucleus. This causes a tipping of the magnetization vector M_0 towards the xy-plane, where it will rotate in that plane along the external magnetic field. The magnetic component in the xy-plane (which is an electrical current) is the NMR signal, which can be detected by a

receiver. [83,85,86] This principle is similar to the Bloch vectorial picture, which is explained for nonlinear IR-spectroscopy (see chapter 2.3).

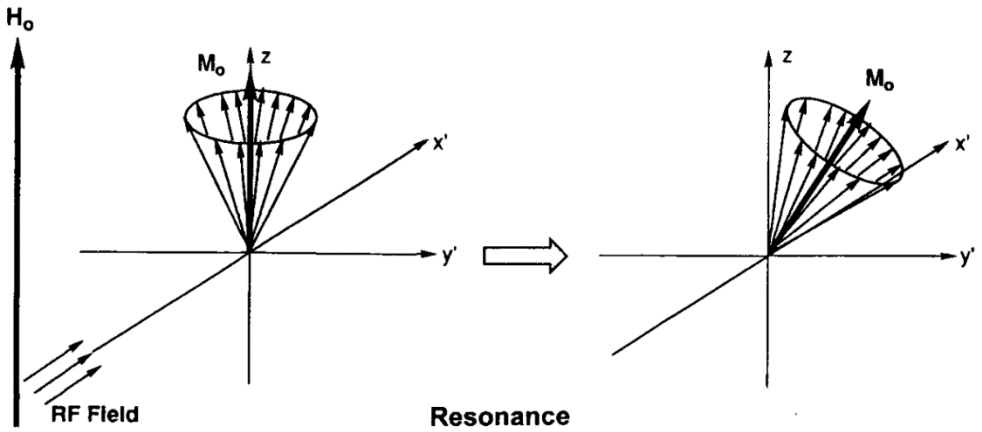

Figure 2-10: (a) The magnetic moments of the nuclei, which precess around the z-axis create a net magnetization vector M_0, which interacts with a radiofrequency field. (b) After the resonant interaction with the radiofrequency field, the magnetization vector M_0 is tipped towards the xy-axis. This figure was published in '1H-NMR and 13C-NMR spectroscopy', Metin Balci, p. 246, Copyright Elsevier (2005). Reprinted with permission of Elsevier. [86]

The resulting signal in NMR spectroscopy will also reveal a free induction decay (FID), as the magnetization vector M_0 precesses around the z-axis. The detected signal is the induced magnetization M_y in the y-direction, which is the projection of the magnetization vector onto the y-axis. It induces an electric current, which can be detected as NMR signal by a receiver coil. Consequently, the detected signal will be a sinusoidal signal that also decays with increasing time due to an exponential decrease of the magnetization, which is a result of the relaxation of the nuclei back to equilibrium.

Here, we use ^{1}H-NMR spectroscopy to probe the electronic environment of protons, more specifically the protons of the NH-group of urea- and thiourea motifs. As a model system for catalyst-substrate binding, we explore the binding of (thio)urea derivatives to the substrate. Upon binding of the (thio)urea group to the substrate, the formation of a hydrogen-bond leads to a decreased electron density around the NH-proton, which results in a downfield-shift of the chemical shift of the NH-proton. One needs to consider that the NH-proton will change between two environments, free and hydrogen-bonded. If a nucleus exchanges rapidly (compared to the timescale of a NMR measurement, which is in the range of milliseconds [84,87]) between two environments, the observed chemical shift will be a mole fraction weighted average between the chemical shift of environment A and the chemical shift of environment B: [58,84]

$$\delta_{obs} = p_A\delta_A + p_B\delta_B, \tag{2-67}$$

where p_A and p_B are the fractions of the nuclei in environment A and B.

3 METHODS

In this chapter, the equipment and the experimental setups of the techniques are described, which are used in this thesis: the infrared setups FT-IR, Pump-Probe IR and 2D-IR spectroscopy and NMR spectroscopy.

3.1 INFRARED SETUPS

3.1.1 LINEAR FT-IR SPECTROSCOPY

To measure linear IR absorption spectra, I used Fourier-transform infrared spectroscopy (FT-IR), by using a Bruker Vertex 70 spectrometer and a Nicolet Magna 850 spectrometer. The measurements were performed in transmission geometry and the resolution of the obtained spectra was 4 cm^{-1}. The samples were solutions and were kept between two CaF_2 windows within a demountable sample cell from Merck. The thickness was adjusted to achieve an absorbance of ~0.2-0.8 in the FT-IR spectrum, by choosing a suitable spacer (ranging from 0.05 mm to 0.5 mm thickness). The same sample preparation and sample cell were also used for Pump-Probe IR spectroscopy and for 2D-IR spectroscopy.

3.1.2 PUMP-PROBE IR SPECTROSCOPY

To measure time-resolved and to study the vibrational dynamics of the systems, I used broadband femtosecond infrared pump-probe spectroscopy (Pump-Probe IR), which is schematically shown in *Figure 3-1*. A Ti:sapphire regenerative amplifier (Spitfire Ace, Spectra Physics or Coherent Astrella) was used to generate 800nm pulses (~50 fs pulse duration, 1.5 mJ or 3 mJ pulse energy, 1 kHz repetition rate). The beam was guided to an optical parametric amplifier (OPA), generating signal and idler radiation. These were guided to a non-collinear difference frequency generation stage (NDFG) to generate infrared pulses (Topas Prime with NDFG stage, Light Conversion, Spectra Physics or Coherent). The mid-IR pulses (~ 20 µJ pulse energy, ~ 200 fs long and a FWHM of ~ 400 cm^{-1}) were centered at the frequency range of interest (3000nm, 4000nm and 6000nm, respectively), in order to excite molecular vibrations in this frequency range. Residuals of signal and idler radiation were removed with an iris. A wedged ZnSe window splits the beam in a pump and a probe path, whereby the pump beam contains

most of the energy and is transmitted through the ZnSe window. The probe and reference beams are divided by a 50:50 ZnSe beamsplitter, whereas the reference beam is transmitted and the probe beam is reflected and guided to the sample.

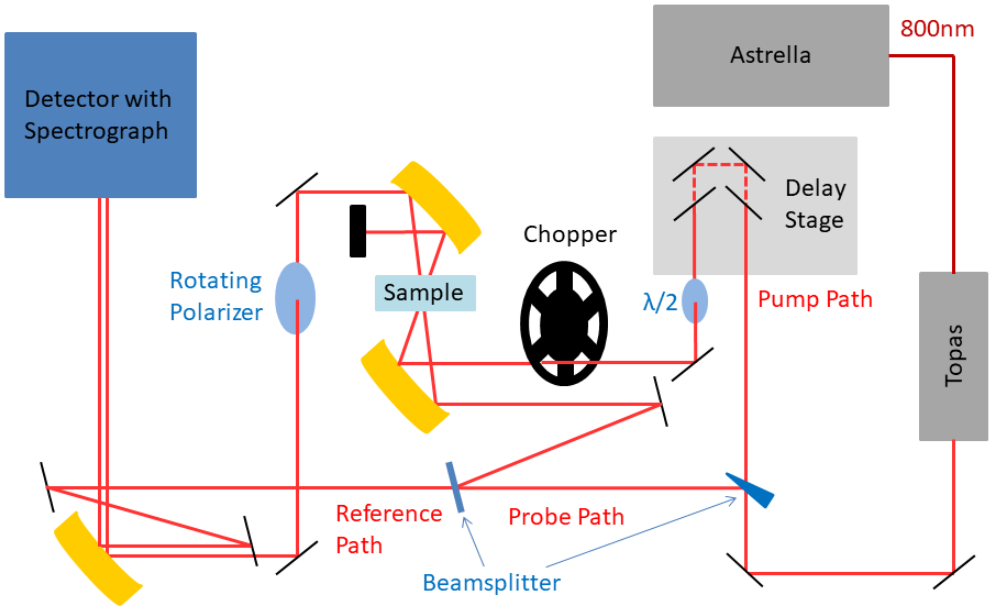

Figure 3-1: Schematic picture of a Pump Probe setup. A Ti:sapphire regenerative amplifier (Astrella) creates and amplifies 800nm radiation. The OPA and NDFG stage (Topas, Light Conversion) generates the IR pulses. A wedged window splits the beam path in pump and probe path. Every second IR pulse in the pump path is blocked by the chopper. The delay stage is used to control the time delay between pump and probe pulse. The sample is placed between two parabolic mirrors, where pump and probe pulse are spatially and temporally overlapped. The polarization is controlled with the $\frac{\lambda}{2}$ *plate and the rotating polarizer. To detect the probe and reference pulse, a spectrograph and a MCT detector are used.*

The pump beam is guided to a delay stage to control the time delay between pump and probe pulse, which is a prerequisite to measure time-resolved. It further passes a $\frac{\lambda}{2}$ plate to control the polarization (tuned to 45° with respect to the probe pulse) and a chopper, which blocks every second IR pulse. This is necessary to obtain the pump induced modulation of the infrared absorption Δα, to measure a difference spectrum by measuring a probe spectrum alternately with and without pump pulse, by collecting the transmitted intensities I on the detector: [63]

$$\Delta\alpha = -\ln\left(\frac{I_{probe}/I_{reference}}{I_{probe,0}/I_{reference,0}}\right), \tag{3-1}$$

where I_{probe} and $I_{reference}$ refer to the IR intensities with a pump excitation pulse and $I_{probe,0}$ and $I_{reference,0}$ refer to IR intensities without pump pulse. The advantage of the reference beam is that it cancels out pulse-to-pulse fluctuations. After the chopper, the pump beam is focused with a parabolic mirror into the sample, where it overlaps with

the probe beam. The beams are re-collimated after the sample with a second parabolic mirror. To find temporal and spatial overlap of pump and probe pulse, we used a thin germanium plate. The pump beam is blocked after the sample and the probe beam is guided to a polarizer, which can be automatically rotated by 90°. This enables to measure the modulation of the probe pulse with parallel $\Delta\alpha_{\parallel}$ and perpendicular $\Delta\alpha_{\perp}$ orientation with respect to the pump pulse. The probe beam is focused into the spectrograph, spectrally dispersed and detected with a liquid-nitrogen-cooled mercury cadmium telluride (MCT) array detector. The reference beam is directly guided to the spectrograph, where it is also detected with the MCT detector. Similar experimental setups are described in the literature. [63,64,88,89] The isotropic modulation can be constructed with: [63]

$$\Delta\alpha_{iso} = \frac{(\Delta\alpha_{\parallel} - 2\Delta\alpha_{\perp})}{3} \tag{3-2}$$

The signal is rotation-free and reveals vibrational population dynamics. To also obtain information on rotations and energy transfer, one needs to construct the anisotropy R:[63]

$$R = \frac{\Delta\alpha_{\parallel} - \Delta\alpha_{\perp}}{\Delta\alpha_{\parallel} + 2\Delta\alpha_{\perp}} \tag{3-3}$$

As preferentially molecules are excited, whose transition dipole is parallel aligned to the polarization of the pump pulse, the distribution of excited molecules is anisotropic at early delay times. With increasing delay time, the anisotropy will decay to zero, due to reorientation of the molecules and energy transfer; the distribution becomes isotropic.

3.1.3 2D-IR SPECTROSCOPY

To also resolve the pump frequency axis, I used two-dimensional infrared (2D-IR) spectroscopy, which is shown schematically in *Figure 3-2*. Therefore, a regenerative amplifier (Coherent, Astrella) was used to generate 800nm pulses (~ 3mJ, ~ 35 fs pulse duration, 1kHz repetition rate). The pulses were used to pump an optical parametric amplifier (OPA, Topas Prime, Coherent) to generate signal and idler radiation. Then the signal and idler radiation were guided to a non-collinear difference frequency generation (NDFG) stage (Coherent) to generate IR pulses centered at 4000 nm or 6000nm (~ 23 µJ pulse energy, ~ 200fs duration, ~ 400cm^{-1} FWHM), respectively. The IR radiation was then guided to a commercial 2D-IR (2D-Quick IR, Phasetech Inc.) spectrometer, in which a wedged ZnSe window was used to divide the beam in a pump and probe path (most energy is contained in the pump pulse). The probe beam was further separated with a beamsplitter in a probe and a reference path. They propagate

on top of each other and are guided to the sample. The pump beam was guided to a pulse shaper based on spectrally dispersed diffraction from a Germanium acousto-optic modulator (AOM), [68,90-93] which modulates the pump beam and is explained in more detail in chapter 3.3. It creates a pair of two pump pulses (~ 2 µJ) for 2D-IR measurements, but it can also be used in the chopping mode for Pump-Probe IR measurements, which blocks every second pump pulse. The pump beam was then guided to a motorized delay stage, which controls the time delay T_w between probe and pump pulses. The polarization of the pump pulse was adjusted with a half-wave plate to a 45° orientation with respect to the orientation of the probe pulse. The pump and probe beams were spatially overlapped and focused in the sample. A thin germanium plate was used to find temporal and spatial overlap and to optimize group velocity dispersion (GVD) correction of the pulse shaper. The reference beam and the third-order non-linear signal from the sample heterodyned with the probe pulse were collected in the frequency domain by spectrally dispersing them in a spectrograph (SP2156 spectrograph, Princeton Instruments, 75 l/mm grating) and detecting with a 128 × 128-pixel liquid-nitrogen-cooled mercury cadmium telluride (MCT) array detector.

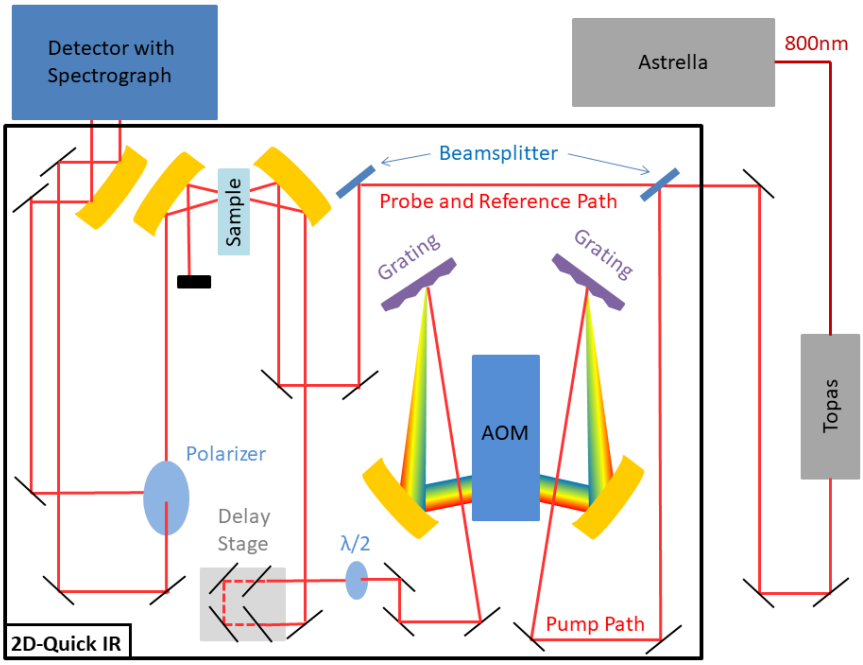

Figure 3-2: Schematic picture of a 2D-IR setup. A Ti:sapphire regenerative amplifier (Astrella) creates and amplifies 800nm radiation. The Topas (with OPA and NDFG stage) generates the IR pulses. In the 2D-Quick IR setup, a beam splitter splits the pump path from the probe and reference path. The AOM shapes the pump pulse as desired and can be used e.g. in the pump-probe mode similar to a chopper or to create a pump pulse pair for 2D-IR measurements to resolve the pump frequency axis. The delay stage within the pump path controls the time delay between pump and probe pulses. Between two parabolic mirrors, pump and probe pulse are spatially and temporally overlapped in the sample. A $\frac{\lambda}{2}$ *plate and a polarizer are used to control the polarization. Probe and reference pulses are detected with a spectrograph and an MCT detector.*

To split the third-order non-linear signal from the sample in its parallel and perpendicular contributions (with respect to the pump pulse), a wire-grid polarizer after the sample was used, which reflects one polarization and transmits the other polarization. The excitation frequencies were resolved in the time domain. Therefore we used two temporally separated pump pulses with controlled coherence times and phases. Subsequently, a Fourier-Transformation of the transient signals at different probe frequencies is performed, enabling the frequency resolution along the pump axis.[67,68,93-95] The 2D-IR spectra were then recorded for multiple waiting times. The data collection was performed in the rapid scan mode using four-frame phase cycling, in order to suppress background scattering and transient absorption contributions. A rotating frame was used to reduce the number of scanned coherence times and phases. For the measurements at 4000nm, the raw data contained 68 coherence times at increments of 30 fs step size. It was apodized with a Hamming window and zero-padded to 128 data points in the time-domain. After Fourier- Transformation to the frequency-domain, we obtain a pump frequency resolution of ~ 4 cm^{-1}. For the measurements at 6000nm, the data contained 134 coherence times at increments of 60fs step size and they were apodized with a Hamming window and zero-padded to 256 data points in the time domain. The spectra were also smoothened along the probe axis, by using a Gaussian window function. The data collection and analysis is described in more detail in chapter 3.3.

3.2 Nuclear Magnetic Resonance Spectrometer

To study the strength of interaction between catalyst and substrate, I used NMR spectroscopy, in order to obtain information on the chemical environment of the functional group of the catalyst. ^{1}H-NMR spectroscopy was performed on a Bruker 300 MHz AVANCE III spectrometer. The ^{1}H-NMR spectra were measured in deuterated solvents (dichloromethane (DCM), toluene and acetonitrile) and were referenced to the residual toluene peak at 2.09 ppm, the residual DCM peak at 5.32 ppm or the residual acetonitrile peak at 1.94 ppm. The chemical shift was determined by using the chemical shift value at the peak maximum.

3.3 Analysis

To analyze the time-dependent 2D-IR data and plot the transient signal as a function of the pump frequency and the probe frequency, one has to apply a Fourier-transformation on the free-induction decay (FID) of the third-order response, which is measured in the time-domain (compare to chapter 2.3). The data, which is collected along the probe

frequency axis is measured in the frequency domain, whereas the data along the pump axis is collected in the time domain and needs to be Fourier-transformed to the frequency domain. The definition of the Fourier-transformation of a time-domain function to the frequency domain is: [67]

$$f(\omega) = FT(f(t)) \equiv \frac{1}{\sqrt{2\pi}} \int_{-\infty}^{\infty} f(t) e^{i\omega t} dt \tag{3-4}$$

To enhance the frequency resolution of the spectrum, zero-padding in the time-domain with the FFT-algorithm can be applied, before Fourier-transforming to the frequency domain. Zero-padding implies, that zeros are added to the time-domain data, in order to increase the number of time points. Therefore, also the integration window t_{max} is increased, which results in a higher frequency resolution after the Fourier-transformation. [67] However, if the emitted signal in the time domain is not decayed to zero at the end of the scan, truncation artefacts will appear due to the limited measuring window. To eliminate truncation effects, window functions can be applied. Usually, the time-domain data is multiplied with a square function. The Fourier-transformation is the sinc function, which can give rise to a lineshape with side-bands in the frequency domain. These side-bands can easily be misinterpreted as cross-peaks. Hence, truncation artefacts should be minimized. A solution is to apply a window function, which smoothens the transition of the emitted signal to zero. In this work, I use a Hamming window function for the time-domain data along the pump axis before the Fourier-transformation to the frequency domain in order to remove truncation effects:[67]

$$s(t) = 0.54 + 0.46 \cos\left(\pi \frac{t}{t_{max}}\right), \tag{3-5}$$

with t being the time delay between the two pump pulses and t_{max} is the maximum scanned time delay. In order to smooth the data, a Gaussian window function along the probe axis was used.

To resolve the pump frequency axis, a Germanium acousto-optic modulator (AOM) is used, in order to shape the mid-IR pulses (see *Figure 3-2*). It enables to choose the amplitude and phase for each wavelength as desired. This works as follows: The IR beam is guided to the first grating, where it is spectrally dispersed at Littrow angle. The parabolic mirror then collimates the beam in the Fourier plane into the AOM with a Bragg angle of ~2°, where each frequency is located at a different position at the AOM. Along the germanium crystal inside the AOM propagates an acousto-optic wave (almost perpendicular with respect to the incoming IR beam), which is generated by an arbitrary waveform generator (AWG) with piezo transducer and amplifier. The acoustic wave appears static to the IR pulse, because of the notable lower velocity of the acoustic wave. Therefore, it acts to the pulse like a static Bragg diffraction grating and can be applied as a mask. It diffracts the respective mid-IR frequencies and enables to individually tune the amplitude and phase of each frequency. After the AOM, the diffracted beam is guided to a second parabolic mirror, which focuses the beam onto a second grating. The grating

collimates the beam again. In this thesis, the AOM is used to generate two pump pulses with variable time delay τ out of the original pulse. The time delay τ between the two pump pulses can be shifted by changing the phase of the mask. Here, the later pump pulse is kept constant in time with respect to the probe pulse. Therefore, changing the time delay between the two pump pulses τ does not affect the time delay between pump and probe pulse T_W, which is known as waiting time and follows the response of the sample at different times. It is the interference of both pump pulses at the sample, which creates the desired spectrum. [67,90,94,96] Consequently, the AOM can apply a different modulated grating for each pump pulse pair (at a repetition rate of 1 kHz). This enables to measure each individual probe pulse at different excitation frequencies.

The AOM offers various advantages, such as the control of the phase of the two pump pulses and faster data collection. To control the phase of the two pump pulses enables phase cycling, which offers several benefits: it can be used to remove scatter and transient absorption background, to measure in the chopping mode (which enables to measure one-dimensional pump-probe spectra), to select certain Feynman pathways and the use of applying a rotating frame. In the following, phase cycling and rotating frame will be explained in more detail. Phase cycling can be applied, because the phase of the transient third-order signals depend on the phase shift between the pump pulses Φ, whereas the transient absorption background is independent of the phase of the pump pulses. Hence, the signal is collected with two different phase shifts of the pump pulses ($\Delta\Phi = 0$ and $\Delta\Phi = \pi$) for each time delay and then they are subtracted ($I(\Delta\Phi = 0) - (\Delta\Phi = \pi)$). The two signals have different phase shifts and will remain, but the background stays the same and is removed due to the subtraction. Therefore, only the desired signal remains and the signal size is enhanced by a factor of two, because of the opposite sign of $\Delta\Phi = 0$ and $\Delta\Phi = \pi$. The following phase cycling sequence can be used to remove additionally pump scattering:

$$S_{PC} = S(\Phi_1 = 0, \Phi_2 = 0) - S(\Phi_1 = 0, \Phi_2 = \pi) + S(\Phi_1 = \pi, \Phi_2 = \pi) - S(\Phi_1 = \pi, \Phi_2 = 0) \quad (3\text{-}6)$$

Hence, transient absorption background and pump scattering are subtracted, whereas the desired signal S_{PC} is enhanced through the summation of the four measurements.[67,68]

Phase control also offers the advantage of collecting data in the rotating frame mode. This enables to reduce the number of data points, which need to be measured, in order to resolve the FID. The FID contains the fundamental frequency of the oscillation of the molecule ω_0, but the desired information like for instance the lineshape or the broadening are contained in the envelope of the oscillation. Measuring in a full rotating frame enables to only measure the envelope, while removing the oscillation (*Figure 3-3*). For this purpose, the delay between the pump pulses τ and also their phase difference $\Delta\Phi$ needs to be changed simultaneously. As the measured signal depends on the time delay τ and the phase difference $\Delta\Phi$, one can choose their combination in such a way,

that the signal will still decay, but it will stop to oscillate. This enables to measure the envelope of the emitted signal, but not the fundamental frequency. In practice, a partially rotating frame is applied in many cases. It means that the rotating frame is set to a frequency below the frequency of interest (ω_i), which shifts the frequency of the emitted signal to $\omega_0 - \omega_i$ and one will observe a reduced frequency of the FID. Therefore, less data points are needed and the data acquisition will be faster. [67,68]

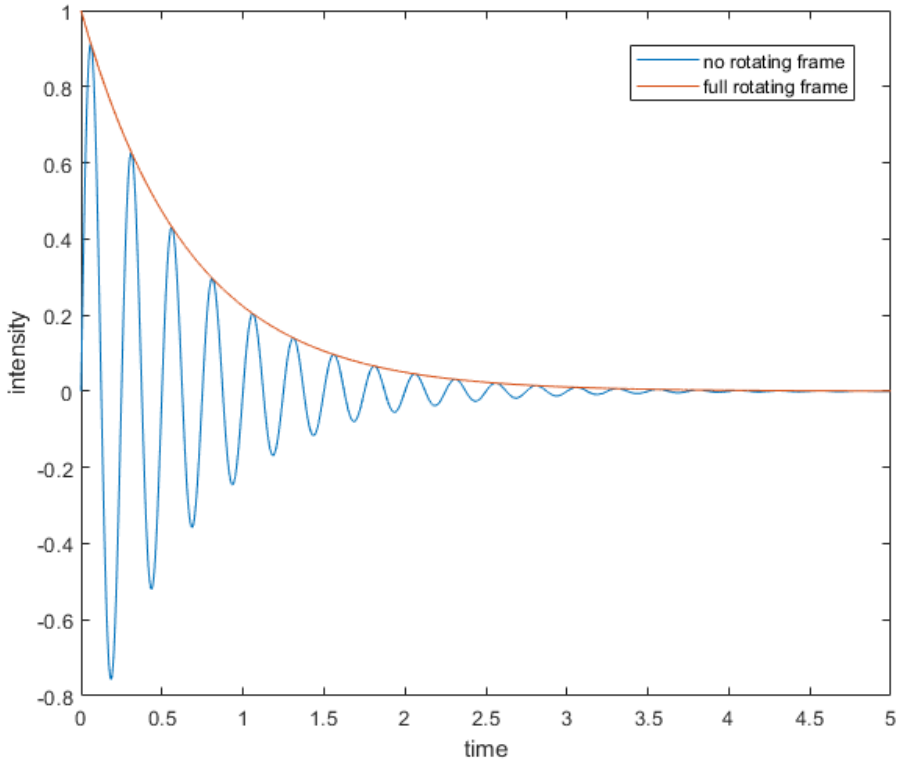

Figure 3-3: The free induction (FID) of a sample is shown schematically, which is the response at one probe frequency for different time delays between the pump pulses (blue). By applying a rotating frame (red) less data points in the time domain are needed to resolve the envelope of the FID.

4 HYDROGEN-BONDING ASYMMETRY OF UREA

A. A. Ehrhard, B. Marekha and J. Hunger, “Hydrogen-Bonding Asymmetry in Urea”. This Paper manuscript is in preparation.

[redacted]

Author contributions: [redacted]

4.1 ABSTRACT

Hydrogen-bond donation of urea is frequently used as a structural motif in molecular self-assembly, catalysis, or to denature proteins. Although the effect of urea on the hydrogen-bonded network of water has been studied in great detail, the structure and dynamics of H-bonds formed by urea itself have remained elusive. To investigate the hydrogen-bonds donated by urea, we study urea-d4/urea mixtures in dimethylsulfoxide (DMSO) using vibrational spectroscopies. We find that the symmetric and antisymmetric ND_2 stretching modes of ND_2 groups and the N-D stretching modes of NHD groups give rise to spectrally separated infrared absorption bands, with the linewidth of the N-D absorption band being much broader than those of the ND_2 modes. 2D-IR spectroscopy experiments reveal that homogeneous linewidths and the vibrational lifetimes of all three modes are similar. Yet, the inhomogeneous width of the N-D stretching mode is ~1.5-2 times larger than of the ND_2 modes, indicating that the hydrogen-bond environments give rise to a broader frequency range for the N-D compared to the ND_2 modes. Density functional theory calculations show that a marked asymmetry in the hydrogen-bond strengths of the two N-D groups of an amine can explain the experimental observations. This asymmetry may provide a rationale for the high directionality of urea hydrogen-bonds, relevant to its applications.

4.2 INTRODUCTION

Urea is an efficient protein denaturant. The controversy on whether urea affects proteins indirectly via altering the structure of water [97-100] or via direct interactions,[101-105] has led to in-depth studies of aqueous urea solutions.[106-114] In recent years urea-protein interactions,[115-117] including hydrogen-bonding of urea to carbonyl groups of amides,[113] have been suggested to underlie the denaturing activity. This hydrogen-bonding of urea-motifs has also been utilized in many applications, like e.g. catalysis,[20,25,118-120] molecular self-assembly,[121,122] ion coordination, or crystal engineering.[123] Remarkably, despite its biological and technological relevance, urea's hydrogen-bonding structure and dynamics have remained largely elusive.

To study the hydrogen-bonding structure and dynamics, vibrational spectroscopies are the method of choice.[63,64,67,124,125] Yet, in the presence of OH moieties, like e.g. OHs of water in aqueous solution, studying hydrogen-bonding of urea's NH groups is experimentally challenging, as urea's NH and OH stretching vibrations spectrally overlap.[106] Also, fast isotopic exchange upon isotopic labelling prevents isolating urea's hydrogen-bonds: Both, NH and OH protons, are prone to isotope exchange and N-D groups of isotopically substituted urea have both, a lower cross-section and a shorter vibrational lifetime [106] as compared to water's OD groups. Thus, besides some studies of neat liquids containing N-H groups,[64,126-129] most of our understanding of N-H hydrogen-bonding dynamics stems from bonding within DNA base pairs or peptides – often studied in non-hydrogen-bonding solvents.[43,130-135] In general, these studies have revealed that vibrational population relaxation is accelerated upon hydrogen-bonding,[132] evidencing enhanced coupling of the N-H groups to lower-frequency modes, like e.g. C=O modes,[135] yet the two N-H oscillators of NH_2 moieties become "decoupled" upon hydrogen-bond formation. In turn, the hydrogen-bonded N-H groups show both marked inter- and intra-mode coupling, resulting in a rather complex vibrational structure that prevents a straightforward interpretation of the vibrational observables.[133] Despite the obvious differences between DNA base pairs and urea, such as rigid bonding within DNA[43] as opposed to the dynamic hydrogen-bonds of urea,[136] DNA base pairs and urea share common chemical structural motifs.

To study hydrogen-bonding of urea we perform linear and ultrafast nonlinear vibrational spectroscopy experiments on urea dissolved in dimethylsulfoxide (DMSO), which has been shown to be a good proxy for a highly polar environment.[137,138] Linear absorption spectra – after isotopic exchange – reveal the presence of ND_2, (symmetric and antisymmetric) and N-D (of NDH groups) stretching modes for urea-d4/urea mixtures. Using two-dimensional infrared spectroscopy, we find that the homogeneous linewidths and the vibrational population lifetimes for all stretching modes are similar and that the antisymmetric and symmetric ND_2 modes are coupled. Remarkably, the inhomogeneous linewidths are much broader for the N-D stretching mode as compared

to the ND_2 vibrations. The different homogeneous linewidths can be explained by antisymmetric hydrogen-bond strengths of the two hydrogen-bond donor sites of ureas ND_2 moiety, which is supported by density functional theory calculations.

4.3 Experimental Methods

Sample preparation
Urea (ACS reagent) and urea-d4 (98% D) were purchased from Sigma-Aldrich (Germany) and used without any further purification. The samples were prepared by weight in glass vials using an analytical balance. The total molal concentration (c_{total} = c_{urea} + $c_{urea\text{-}d4}$) of urea (c_{urea}) and urea-d4 ($c_{urea\text{-}d4}$) was kept constant at c_{total} = 0.36 mol/kg. We study three different isotopic compositions of urea-d4:urea: urea-3:7 ($c_{urea\text{-}d4}$ = 0.11 mol/kg and c_{urea} = 0.25 mol/kg), urea-7:3 ($c_{urea\text{-}d4}$ = 0.25 mol/kg and c_{urea} = 0.11 mol/kg), and urea-1:0 ($c_{urea\text{-}d4}$ = 0.36 mol/kg). To minimize water impurities, we used dimethylsulfoxide (DMSO, extra dry, Acros Organics, 99.7%, water content: <0.005%) and prepared all samples in an Ar-filled glovebox to prevent uptake of moisture. Demountable sample cells for infrared spectroscopy were assembled and filled in the glovebox.

FT-IR experiments
FT-IR spectra were recorded in transmission using a Bruker Vertex 70 IR spectrometer at a resolution of 4 cm^{-1}. The spectra were collected with a "Specac demountable Omni Cell" from Sigma Aldrich with the sample positioned between two CaF_2 windows and an optical path length of 0.1 mm (urea-d4), 0.2 mm (urea-3:7) and 0.3 mm (urea-7:3) to ensure a comparable absorbance of ~0.5 to 0.9 in the 2500 cm^{-1} spectral region.

2D-IR experiments
For the fs-IR and the 2D-IR experiments, a Ti-sapphire-based regenerative amplifier (Coherent Astrella) was used to generate 800 nm pulses. ~3 mJ of the 800 nm pulses were used to pump an optical parametric amplifier (TOPAS Prime, Coherent). The resulting signal and idler pulses were used to generate mid-IR pulses (~23µJ pulse energy, ~200 fs long, ~400 cm^{-1} FWHM, centered at 2500 cm^{-1}) in a non-collinear difference-frequency generation (NDFG) stage based on a KTA crystal. In the 2D-IR spectrometer (2D-Quick, PhaseTech Inc.) a wedged ZnSe window was used to split off a small fraction of the IR pulses, which is divided with a beam splitter into a probe and a reference beam. The transmitted pulse was guided to a pulse shaper based on a Germanium-based acousto-optic modulator (AOM). [67,68] The modulated pump beam (~2 µJ) was guided to a motorized delay stage to control the time delay between probe and pump pulses (T_w) and the polarization was controlled using a half-wave plate. The pump and the probe beams were focused and spatially overlapped in the sample. We used the IR-induced absorption in a thin Germanium plate to find temporal overlap and

optimize group velocity dispersion (GVD) correction using the pulse shaper. For the 2D-IR experiments, the third-order non-linear signal from the sample heterodyned with the probe pulse was collected in the frequency domain, by dispersing the probe beam using a 75 l/mm grating onto a 128x128 pixel liquid-nitrogen-cooled mercury cadmium telluride (MCT) array detector. A wire-grid polarizer after the sample was used to split the probe beam in its parallel and perpendicular components with respect to the pump pulse. Excitation frequencies were resolved in the time-domain, by controlling pump-pulse pairs with controlled coherence times and phases. [67,68] The spectra were collected in the rapid-scan mode using four-frame phase cycling to reduce background scattering and transient absorption contributions. To reduce the number of scanned coherence times, phases were controlled using a rotating frame.[93] Raw data containing 68 coherence times at increments of 30 fs were apodized using a Hamming window and zero-padded to 128 data points in the time domain before Fourier transformation to the frequency domain (excitation frequency resolution of ~4 cm^{-1}). Similar to the pump axis, spectra were smoothened along the probe axis using a Gaussian windowing function in the time domain.

Density functional theory calculations

All calculations were performed using Orca[139] 4.1.1 (BLYP [140,141]-D3(BJ) [142,143]/def2-TZVPP [144,145] level of theory) applying a polarizable continuum model [146] (dimethylsulfoxide). Geometries of one urea molecule, donating four hydrogen-bonds to four DMSO molecules were optimized, while the two hydrogen-bond distances of one amine group were constrained to 1.8-2.2Å at increments of 0.05 Å. Coupled (harmonic) ND_2 frequencies of one of urea's amine groups were obtained from calculations of a urea-d2t2 molecule with 4 DMSO molecules, with the hydrogen-bonding distances to the ND_2 groups being varied. Uncoupled N-D frequencies were obtained based on urea-h1d1t2.

4.4 Results and Discussion

To study hydrogen-bonding of urea, we use the N-D stretching vibration of isotopically substituted urea in DMSO as the N-D (or N-H) stretching vibration sensitively reports on intermolecular hydrogen-bonding.[147] Given the two NH_2 groups of urea, which nominally results in four coupled normal modes with N-H stretch character, the N-H and N-D stretching bands in the infrared absorption spectra of urea are often reported to be rather complex.[148] To vary coupling, we use isotopic substitution by mixing urea and urea-d4. To this end, we use three different isotopic mixtures urea-1:0, urea-7:3, and urea-3:7, for which urea-d4, urea-d3, and urea-d1 are the dominant deuterated species, respectively (*Figure 4-1*, more details on the distribution of species based on a binomial distribution are given in the Supporting information, SI, *Table 4-1*). To ensure complete isotopic exchange, samples were prepared 24h prior to the experiments (see SI, *Figure 4-6*).

Linear FT-IR spectra of Urea

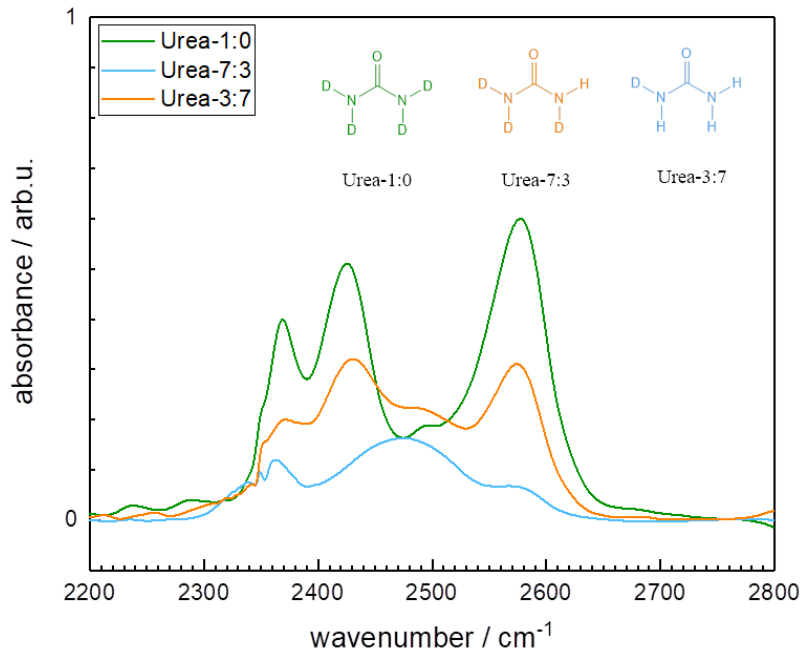

Figure 4-1: Infrared absorption spectra for solutions of urea-1:0 (green), urea-7:3 (orange), and urea-3:7 (blue) dissolved in DMSO. The absorbance of the solvent has been subtracted from all spectra and spectra are normalized to the sample thickness.

In *Figure 4-1*, we show the solvent subtracted infrared absorption spectra for solutions of urea-1:0 (green), urea-7:3 (orange), and urea-3:7 (blue) in DMSO at frequencies characteristic to the ND stretching modes (~2300 – 2700 cm^{-1}). The absorption spectrum of urea-1:0 exhibits two well-separated vibrational modes at 2420 cm^{-1} and 2560 cm^{-1}, due to the symmetric and antisymmetric ND_2 stretching vibrations, respectively. [149,150] Upon isotopic exchange, the N-D stretching band at 2480 cm^{-1} emerges, [149] which signifies itself as a small peak between the two ND_2 modes in the urea-7:3 sample and becomes the main spectral feature in *Figure 4-1* for the urea-3:7 sample (with the symmetric and antisymmetric ND_2 stretching bands still present as shoulders). Remarkably, the linewidth of the ND stretching vibration (~2480cm^{-1}) is much broader than the linewidths of the ND_2 stretching vibrations (~2420cm^{-1} and 2560cm^{-1}). These different linewidths point at different line broadening mechanisms for the studied vibrations.

Adjacent to the symmetric ND_2 stretching vibration, we find for all samples a narrow band at ~2360 cm^{-1}, which is also present in the solid state[149,151]. A similar red-shifted band has been observed at NH stretching frequencies and has been assigned to a combination band of the symmetric NH_2 deformation vibration and the C=O stretching vibration. [148] Yet, the combination band (ND_2 deformation + C=O stretching) would be expected at >2600cm^{-1} and can thus not explain the band at 2360 cm^{-1}. [149] Given that this band is still present in the urea-7:3 sample, for which species with ND_2 moieties are

minor, ND_2 deformation modes seem to not contribute to the band at 2360 cm^{-1}. Rather, the scaling of the intensity of the 2360cm^{-1} band with deuterium concentration (see *Figure 4-1* and *Figure 4-6*, SI) points at a Fermi resonance (e.g. with symmetric + antisymmetric C-N stretching). As such, the lineshape of the symmetric stretching mode at ~2420 cm^{-1} will be distorted.

2D-IR spectroscopy

To explore the origins of the markedly different linewidths [131,152] of the ND_2 and N-D stretching bands, we perform 2D-IR spectroscopy experiments. [67,153,154] Conceptually, 2D-IR allows one to experimentally disentangle the different contributions to the linear IR spectrum by measuring the transient absorption over a broad range of detection frequencies (υ_{probe}) after excitation with υ_{pump}. In a typical 2D IR spectrum, excitation of a specific mode results in a decrease in absorption corresponding to the negative $|0\rangle\leftrightarrow|1\rangle$ ground-state bleach at the diagonal ($\upsilon_{probe} = \upsilon_{probe}$) and the positive $|1\rangle\rightarrow|2\rangle$ excited-state absorption (ESA, at $\upsilon_{probe} < \upsilon_{pump}$ for anharmonic vibrations). Thus, homogeneous broadening can be separated from inhomogeneous linewidths as excitation of a subensemble of oscillators of an inhomogeneously broadened band will change the absorption of the sample only at probing frequency similar to the excitation frequency. As such, inhomogeneous broadening results in elongation of the 2D-IR signals along the diagonal. Coupling of spectrally separated vibrations additionally leads to off-diagonal peaks, and variation of the waiting time between excitation and probing can interrogate molecular dynamics.

In *Figure 4-2*, we show the 2D-IR spectra for the urea-1:0, urea-7:3, and urea-3:7 samples at a waiting time T_w = 200 fs. The 2D-IR spectrum for urea-1:0, shows two well-separated bleaching signals (blue) on the diagonal at ~2420 cm^{-1} and 2560 cm^{-1} due to the symmetric and the antisymmetric ND_2 stretching vibration. Adjacent to the bleaching signal due to the symmetric ND_2 stretching, we detect a ~ 100 cm^{-1} red-shifted induced absorption (red) due to the excited state absorption (ESA). The ~ 100 cm^{-1} anharmonic shift is similar to what has been reported for the N-D group in non-hydrogen-bonded peptides. [134] The symmetric off-diagonal bleaching signals at υ_{pump} = 2420 cm^{-1} / υ_{probe} = 2560 cm^{-1} and υ_{pump} = 2560 cm^{-1} / υ_{probe} = 2420 cm^{-1} evidence coupling between the symmetric and antisymmetric ND_2 modes (see SI, *Figure 4-7*). The absence of any signals due to the lower wavenumber band at 2360 cm^{-1} in the linear IR spectra can partly be explained by reduced pump intensity at lower wavenumbers (see SI, *Figure 4-8*). Upon isoptopic substitution, the lower wavenumber diagonal peak becomes elongated along the diagonal for the urea-7:3 sample, which suggests overlapping bleaching signals due to the antisymmetric ND_2 band at ~2420 cm^{-1} and the N-D stretching band at ~2500 cm^{-1}. Besides the cross peaks of the ND_2 bands as already observed for the urea-1:0 sample, a cross peak at υ_{pump} = 2500 cm^{-1} / υ_{probe} = 2560 cm^{-1} evidences coupling between the ND_2 and the ND stretching vibration, presumably within urea-d3 isotopomers. For the urea-3:7 sample, for which singly deuterated urea (urea-

d1) dominates, we observe a broad main diagonal peak centered at ~2500 cm^{-1} with a red-shifted ESA and only a weak bleaching signal at ~2560 cm^{-1} due to residual ND_2 groups (see SI, *Table 4-1*). Remarkably, the N-D signal in the urea-3:7 sample is significantly elongated along the diagonal, while the ellipticity of ND_2 bleaching signals in the urea-1:0 sample is much less pronounced. Conversely, the width perpendicular to the diagonal, a measure for the homogeneous linewidth, [155] appears fairly similar for all detected vibrations.

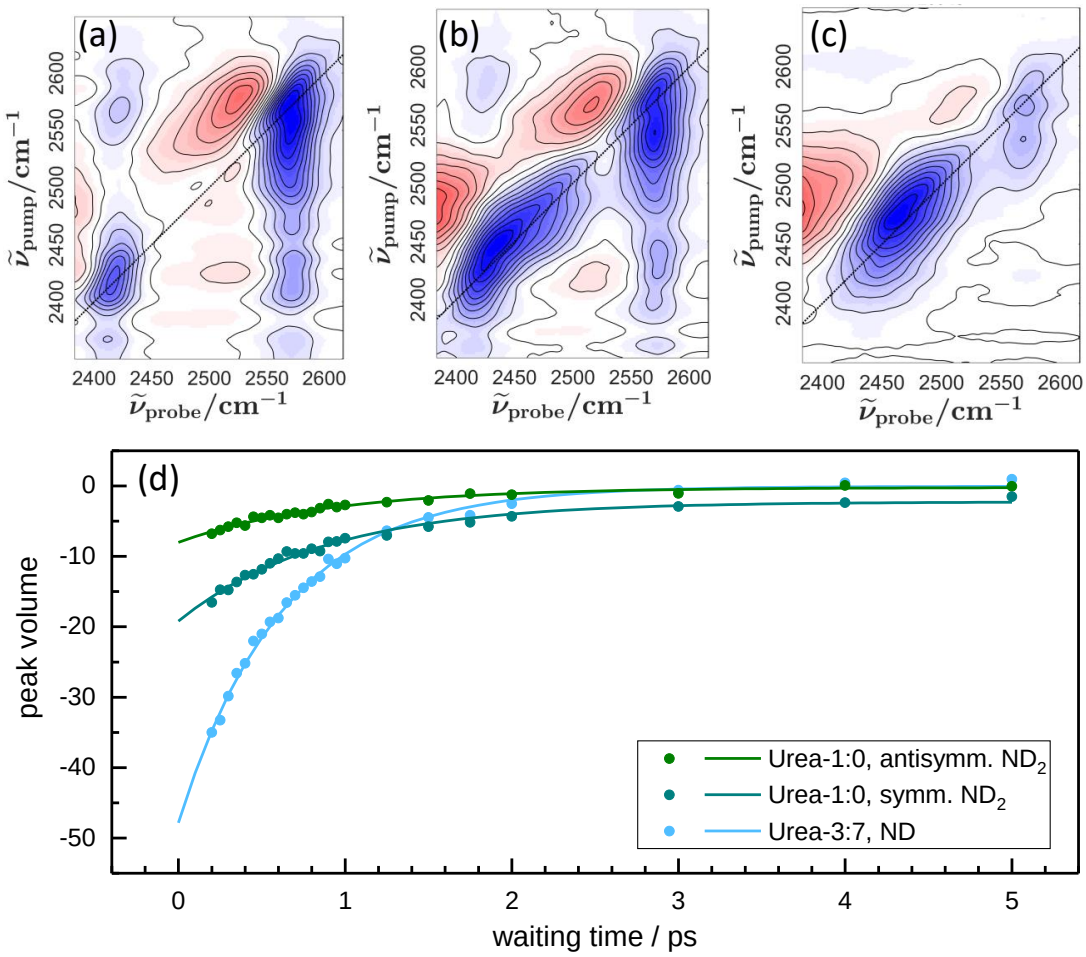

Figure 4-2: Isotropic 2D-IR spectra for solutions of $\boldsymbol{c_{total}}$ = 0.36 mol/kg urea-1:0 (a), urea-7:3 (b) and urea-3:7 (c) in DMSO at T_w=200 fs. The negative (bleaching) signals are shown in shades of blue, and the positive signals are shown in shades of red. The data in each spectrum are normalized to the maximum bleaching amplitude. The diagonal line is shown to guide the eye. (d) Integrated peak volumes (elliptical integration limits are given in Figure 4-9 and Table 4-2, SI) for the N-D stretching (light blue), antisymmetric ND_2 stretching (green), and symmetric ND_2 stretching (blue) vibrations as a function of waiting time. Symbols in (d) show the experimental data, and solid lines show the fits with the kinetic model (eq (4-1)).

One contribution to homogeneous broadening is the population lifetime [80]: longer-lived vibrations give rise to narrower bands. Additionally, accelerated population relaxations for certain modes may indicate contributions from Fermi resonances to the overall line

shapes, as Fermi resonances involving lower-frequency modes can provide efficient relaxation pathways. [156,157] Thus, we quantify the population relaxation via the temporal evolution of the on-diagonal bleaching signals of the different vibrational modes. The integrated bleaching volumes $V(T_w)$ (see SI, *Table 4-2*, *Figure 4-9*) of the symmetric and the antisymmetric ND_2 stretching vibration of the urea-1:0 (*Figure 4-2a*) and the ND stretching vibration of the urea-3:7 sample (*Figure 4-2c*) decay similarly as a function of waiting time and level off at T_w > ~2ps. We model the bleaching volumes assuming that the contribution of the excited state decays with a relaxation time τ and that the dissipation of the vibrational energy in the course of the relaxation leads to a small and persistent modulation of the oscillator (transient signal due to heat):

$$V(T_w) = V_{exc} \cdot e^{\frac{-T_w}{\tau}} + V_{heat} \cdot (1 - e^{\frac{-T_w}{\tau}}) \tag{4-1}$$

with V_{exc} and V_{heat} the magnitude of the contributions of the excitation and the heat, respectively. This model describes the experimental data very well (*Figure 4-2d*) and we obtain for the relaxation of the three modes very similar relaxation times ($\tau_{symm} = 0.91 \pm 0.17\,p$, $\tau_{antisymm} = 0.88 \pm 0.11\,ps$, and $\tau_{ND} = 0.62 \pm 0.04\,ps$). These relaxation times are in fact comparable to the population relaxation time of the N-D group of peptides, [134] or of the N-H mode of N-methylacetamide or DNA base pairs,[134,158,159] which may indicate that the relaxation pathways in these molecules proceed via a common lower-frequency mode (e.g., the C=O stretching or C-N stretching mode) to which they are strongly coupled. [135] Such a common relaxation pathway could also explain the similar lifetimes of the ND_2 and N-D stretching modes of the present study. The similarity further suggests that the contribution of the population relaxation to the homogeneous linewidth is similar for all three bands.

As opposed to the similar dynamics of the three ND/ND_2 stretching modes, their lineshape in both the FT-IR and the 2D-IR spectra is remarkably different. To quantify homogeneous and inhomogeneous contributions to the modes, we consider the diagonal and antidiagonal cuts of the 2D-IR spectra (*Figure 4-3*): In line with the similar population relaxation of all three modes, we find a similar antidiagonal linewidth for all three modes. The FWHMs of the antidiagonal cuts of the 2D-IR spectrum, which is a measure for the homogeneous linewidth, [80] fall in the range of 22-30 cm^{-1} (*Figure 4-3*). This similarity suggests that besides the similar population relaxation, also the pure dephasing is similar for the three modes. Conversely, the FWHM of the diagonal cuts, which also contain broadening due to an inhomogeneity of environments (e.g., distribution of hydrogen-bond strengths), is much broader for the N-D stretching modes (68 cm^{-1}) than for the antisymmetric (45 cm^{-1}) and symmetric (34 cm^{-1}) ND_2 vibrations.

Note that the width of the symmetric band is likely reduced due to the Fermi resonance discussed above. Yet, for both ND_2 modes the high-frequency side of the bleaching signal coincides with the linear absorption band. Only at lower red-shifted frequencies the

absorption spectra and the diagonal slices of the 2D spectra deviate, which is however a result of the superposition of the GSB and the ESA. As such, the ND_2 bands appear to be mostly homogeneously broadened. Further, a Gauss and Lorentz fit to our data confirms that the diagonal linewidths of the ND_2 modes is very similar to the homogeneous linewidths (see SI, *Figure 4-10* and *Figure 4-11*). This observation contrasts the findings for the N-D stretching vibration, for which we find significant inhomogeneous broadening: The FWHM of the diagonal cut is much broader than of the antidiagonal cut and the diagonal and antidiagonal cut do not coincide at higher frequencies.

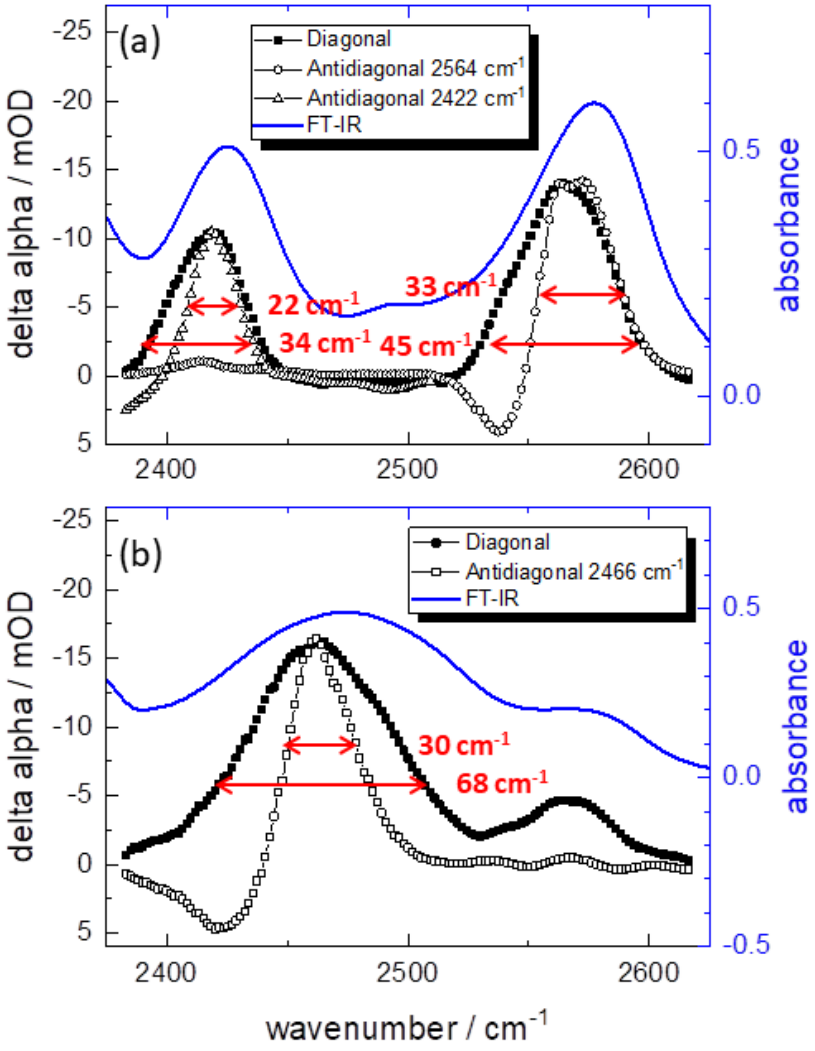

Figure 4-3: Diagonal (filled black symbols) and antidiagonal cuts across the 2D-IR spectra of the (a) urea-1:0 and (b) urea-3:7 sample at T_w= 0 fs (left-hand axis) together with the linear infrared absorption spectra (blue solid lines, right-hand axis). The antidiagonal cuts were chosen such that they intersect the respective minimum bleaching signal. Red arrows indicate the FWHM of the bleaching signals.

As there is no ESA interference at higher frequencies, we conclude that there is significant inhomogeneous broadening, which is also in line with the FWHM determined from fits to the experimental data (see SI, *Figure 4-11*). These differences are also

reflected in higher values of the center-line-slopes [67,160-162] for the N-D stretching mode as compared to the ND_2 modes (see SI, *Figure 4-12*). As such, the lineshape analysis peculiarly suggests that the local N-D stretching vibration is sampling a broader distribution of hydrogen-bonding microenvironments, while the distribution of hydrogen-bonded microenvironments as detected via the ND_2 vibrations is narrower.

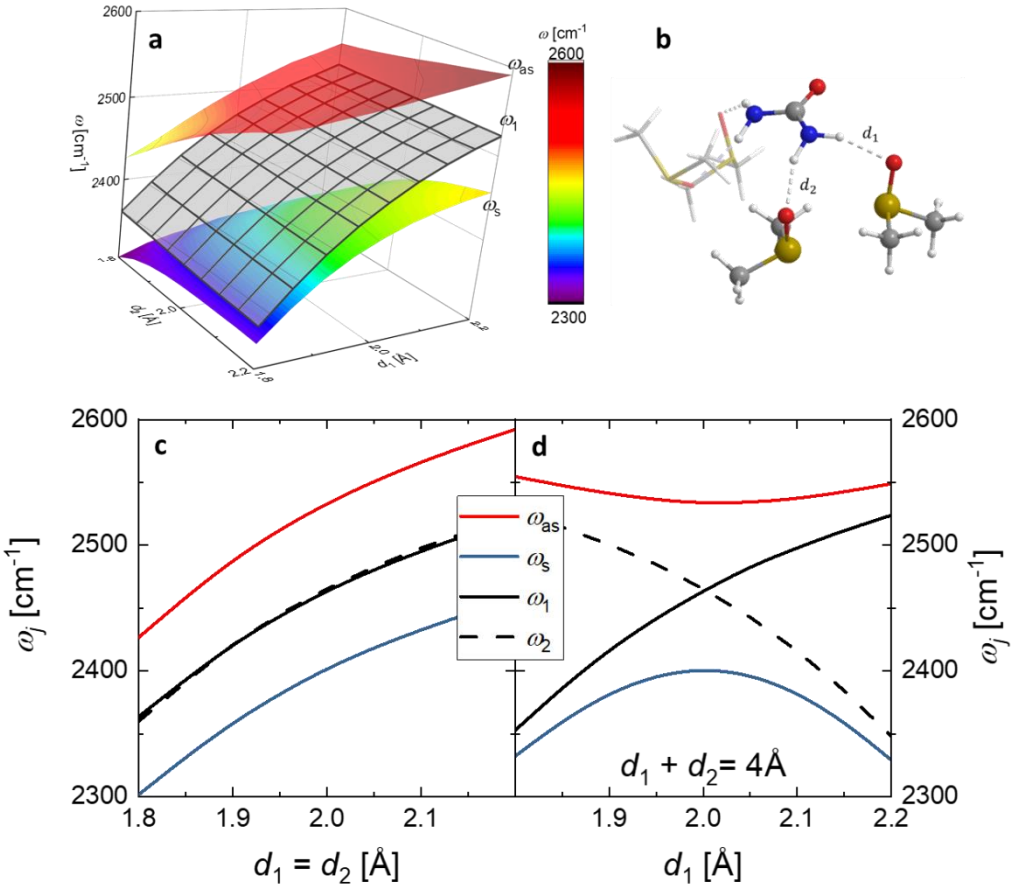

Figure 4-4: (a) Vibrational frequency map for the symmetric ($\boldsymbol{\omega_s}$) and antisymmetric ($\boldsymbol{\omega_{as}}$) stretching vibrations (colored 3D plots) as a function of hydrogen-bond distances $\boldsymbol{d_1}$ and $\boldsymbol{d_2}$ as obtained from relaxed surface scans using density functional theory (see methods section for details). Also shown is the frequency of the local (decoupled) vibration of the N-D$^{(1)}$ group, $\boldsymbol{\omega_1}$, as grey contour plot. (b) Molecular structure of the urea + 4 DMSO complex, for which the hydrogen-bond distances $\boldsymbol{d_1}$ (D$^{(1)}$ - O) and $\boldsymbol{d_2}$ (D$^{(2)}$ - O) were constrained. (c) Diagonal ($\boldsymbol{d_1 = d_2}$) and (d) antidiagonal ($\boldsymbol{d_1 + d_2 = 4}$ Å) cuts through the vibrational frequency map. The frequency of the local (decoupled) N-D$^{(2)}$ mode, $\boldsymbol{\omega_2}$ is shown as dashed line.

To pinpoint the molecular-level origins of the different spread of hydrogen-bonding environments sampled by the N-D and the ND_2 vibrations, we performed density functional theory calculations. To this end, we perform geometry optimizations of a urea molecule donating four hydrogen-bonds to the oxygen atom of four DMSO molecules (*Figure 4-4*). We constrain the hydrogen-bond lengths (D – O distance) of the two

deuteriums of a single ND_2 group at values ranging from 1.8 to 2.2 Å, which are typical hydrogen-bonding distances to DMSO, [163] and map the harmonic frequencies for the coupled ND_2 and uncoupled N-D$^{(1)}$ and N-D$^{(2)}$ oscillators. These frequency maps are shown in *Figure 4-4a*.

Based on these frequency maps, we consider two limiting cases in more detail: (i) correlated and (ii) anticorrelated hydrogen-bonding distances. For (i) correlated hydrogen-bond distances (symmetric elongation of d_1 and d_2, *Figure 4-4c*) the uncoupled N-D frequencies vary from ~2350 to ~2520 cm^{-1} for the studied hydrogen-bond distances. Coupling of both N-D groups in a ND_2 group results in splitting into the symmetric and antisymmetric stretching vibrations, (red and blue lines in *Figure 4-4c*) and the coupled frequencies parallel the resonance frequency of the uncoupled modes. As such, if the distribution of hydrogen-bond distances for both N-D groups would be correlated (e.g. spanning 1.8-2.2Å), the spread of vibrational frequencies sampled by the ND_2 and the N-D vibrations would be the same: As intuitively expected, for correlated hydrogen-bond strengths, the inhomogeneous linewidths of the N-D and the ND_2 stretching vibrations would be the same.

The second limiting case is (ii) anti-correlated hydrogen-bond distances, where a ND_2 group donates preferably one strong and one weak hydrogen-bond. The vibrational frequencies of the ND stretching modes for such anti-correlated hydrogen-bond distances ($d_1 + d_2 = 4$ Å, *Figure 4-4d*) indicate that the local mode frequencies ω_1 and ω_2 are largely determined by d_1 and d_2, respectively and span the full 2350-2520 cm^{-1} range. In turn, for the coupled ND_2 vibrations, the range of the corresponding ω_s and ω_{as} frequencies is significantly smaller: Coupling leads to a splitting of the local modes and avoided-crossings[164] reduces the full range of stretching frequencies (red and blue curves in *Figure 4-4d*) to ~20 cm^{-1} (ω_{as}) and 70 cm^{-1} (ω_{as}) for d_1 ranging from 1.8 to 2.2 Å. Thus, for an anti-correlated symmetric distribution of hydrogen-bonds centered at 2 Å, the inhomogeneous linewidths of the symmetric and antisymmetric stretching modes are expected to be ~2 and ~8 times narrower than the width of the uncoupled N-D vibrations.

Obviously, the ~1.5-2 times broader inhomogeneous linewidth of the N-D stretching mode relative to the ND_2 stretching bands as observed in the experiments, lies somewhere between the limiting scenarios (i) and (ii). To relate the experimental observations for urea to the calculated frequency map, we assume that the distribution of vibrational frequencies of ω_{as}, ω_1, and ω_2 and the distribution of conformations (d_1 and d_2) are uniquely related. Thus, we obtain the hydrogen-bond conformation distribution $p(d_1, d_2) \propto p_{as}(\omega_{as}(d_1, d_2)) \cdot p_1(\omega_1(d_1, d_2)) \cdot p_2(\omega_2(d_1, d_2)$. For the distributions p_{as}, p_1, and p_2 we assume Gaussian distributions with the experimental FWHMs of 45 cm^{-1}, 68 cm^{-1}, and 68 cm^{-1}, respectively. The values for $\omega_{as}(d_1, d_2)$, $\omega_1(d_1, d_2)$, and $\omega_2(d_1, d_2)$ are taken from the calculations shown in *Figure 4-4*. Note, that we do not take the symmetric stretching frequency into account, as the above discussed Fermi resonance may distort the lineshape significantly, and we also neglect frequency-

dependent transition dipole moments. Based on these assumptions, we obtain the hydrogen-bond distribution $p(d_1, d_2)$. The thus obtained distribution (*Figure 4-5*) displays a clear negative correlation (the centerline of the distribution has a negative slope), i.e. the two hydrogen bonds donated by the two N-D groups of urea's ND_2 are anti-correlated. This anti-correlation is in fact further supported by the energy surface obtained from the DFT calculations, which is also elongated along $d_1 + d_2 = 4$ Å.

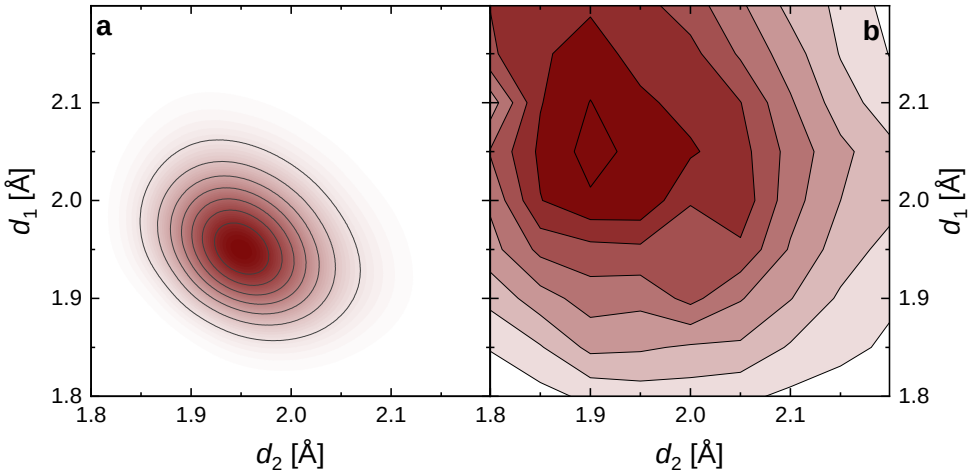

Figure 4-5: (a) Distribution of hydrogen-bond conformations $\boldsymbol{p(d_1, d_2)}$ *as obtained from the calculated frequencies and the experimental widths of the frequency distributions (see text). For comparison in (b) the distribution based on the relative energies of the density functional theory calculations (*$\boldsymbol{e^{-\Delta E/k_B T}}$*) at* $\boldsymbol{T = 298}$ *K are shown.*

Thus, both the experimental linewidths and the DFT calculations provide evidence for urea's hydrogen-bonds being asymmetric, with each ND_2 group donating preferentially one strong and one weak hydrogen-bond – in analogy to what has been found for water based on molecular dynamics [165-167]. In fact, the origin of the hydrogen-bonding anticorrelation can be traced to the hydrogen-bonding potential energy landscape for the formation of two hydrogen-bonds (*Figure 4-5b*). Starting from the energetically most favorable configuration at $d_1 \approx 2.05$ Å and $d_2 \approx 1.9$ Å (Note that the asymmetry originated predominantly stems from dispersive interactions between DMSO molecules, which is presumably less pronounced in the liquid phase where urea is solvated by more than four DMSO molecules), the total energy increases only weakly upon elongating only one hydrogen-bond (at constant d_1 or d_2). Conversely, the energy increases more steeply when weakening both bonds, or shortening one or two bonds. As such, the hydrogen-bonding potential energy surface for a molecule that can donate two hydrogen-bonds is intrinsically asymmetric. As such, the resulting Boltzmann distribution of hydrogen-bonding configurations also displays a slight elongation along the antidiagonal (*Figure 4-5b*).

Our 2D-IR experiments also suggest that this asymmetry persists for urea over remarkably long timescales: The centerline slopes, a measure for the asymmetry of the detected infrared peaks,[161] hardly decay within the accessible time window of 1 ps (*Figure 4-12*, SI) and the frequency-frequency correlation seems to persist over much longer timescales. Hence, despite the overall dynamics – as judged by the viscosity – of DMSO and water differ only by a factor of 2, [168] frequency-frequency correlations persist for urea-d4 much longer than for heavy water, where such correlations have already decayed at <1 ps. [169] Hence, as opposed to water, the hydrogen-bond asymmetry of urea seems to persist over remarkably long timescales.

4.5 Conclusion

As the most direct consequence, our findings imply that – similar to water[167] – molecular forces field models for urea should be re-visited, with potential consequences on understanding the biological activity of urea towards e.g. proteins. [170-172] As urea has two ND_2 groups and each of them can form one strong bond, the herein observed asymmetry may be the key to understand the high directionality of urea's hydrogen-bond properties, [123] which is the key to the function of urea motifs. Such asymmetry may also be used by nature, where the asymmetric bonding is intrinsic to DNA base pairing.[132]

4.6 Supporting Information

Isotopic composition of urea-d4/urea mixtures

Table 4-1: Isotopologues in the studied urea-d4/urea mixtures in DMSO based on a binomial distribution. For the urea-7:3 sample urea-d3 is the main species. For the urea-3:7 sample urea-d1 prevails.

	Urea	Urea-d1	Urea-d2	Urea-d3	Urea-d4
100 % Urea-d4	0 %	0 %	0 %	0 %	100 %
70 % Urea-d4	1 %	8 %	26 %	41 %	6 %
30 % Urea-d4	6 %	41 %	26 %	8 %	1 %
0 % Urea-d4	100 %	0 %	0 %	0 %	0 %

Time-dependent FT-IR spectra revealing NH/ND exchange

In *Figure 4-6* we show the FT-IR spectrum of urea-d4/urea (50% / 50%) in DMSO measured over a time period of 2 weeks after preparation. The solution was stored in a glovebox over this time period to avoid uptake of moisture during NH/ND exchange. We find a marked change of the IR spectrum during the first day (different shades of grey). The measured spectrum after two weeks (blue dashed line) is nearly identical to the spectrum after 1 day (red line). We conclude that the NH/ND exchange is in equilibrium after 1 day. Therefore, all of the samples measured in this study were prepared at least one day prior to the experiment. The peak at ~2360 cm^{-1} decreases with isotope exchange. During exchange the amount of fully deuterated urea decreases, which supports the assignment of the 2360 cm^{-1} peak to a Fermi resonance.

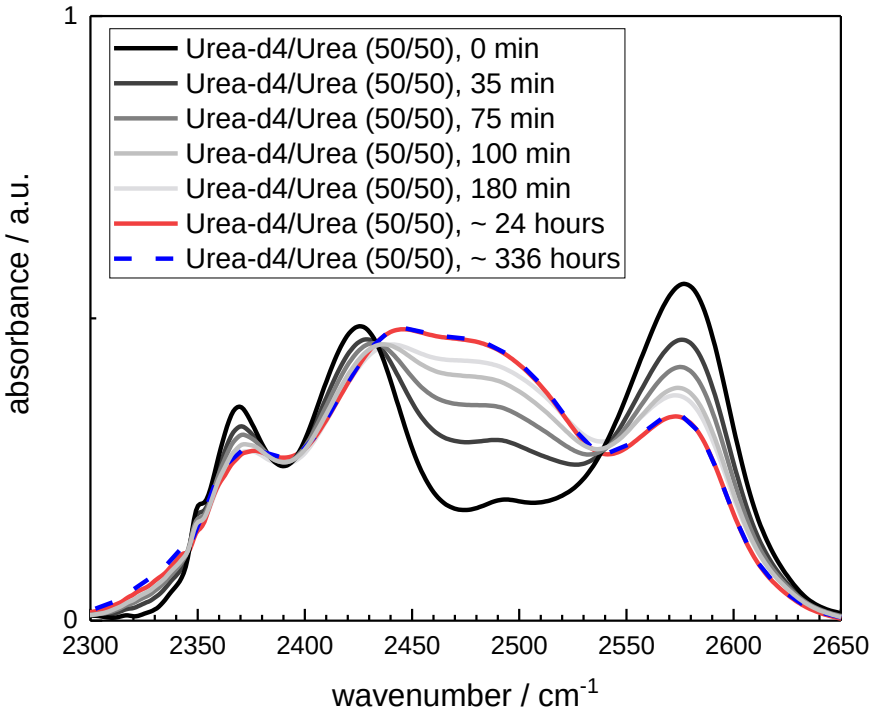

Figure 4-6: Solvent-subtracted FT-IR spectra of an isotopic mixture of urea-d4/urea (50% / 50%) in DMSO as a function of time after mixing. Solutions in DMSO contained a constant concentration of c(urea) + c(urea-d4) = 0.36 mol/kg.

Comparison of decay dynamics of diagonal and antidiagonal peaks

In *Figure 4-7*, we show the peak volume of the diagonal peak (orange) and the peak volume of the corresponding cross peak (same pump frequency, green). In the bottom panel, we plot the peak volumes as a function of waiting time. This reveals that the cross peak is already present at time zero with its highest intensity. As such, the cross peak is predominantly due to coupling between the symmetric and the antisymmetric ND_2 stretching vibration for urea-1:0 and to a coupling between the ND_2 and the ND stretching vibration for urea-7:3. Given the somewhat faster decays of the diagonal peaks compared to the decays of the cross peaks, energy transfer may also contribute to a minor extent to the cross peak.

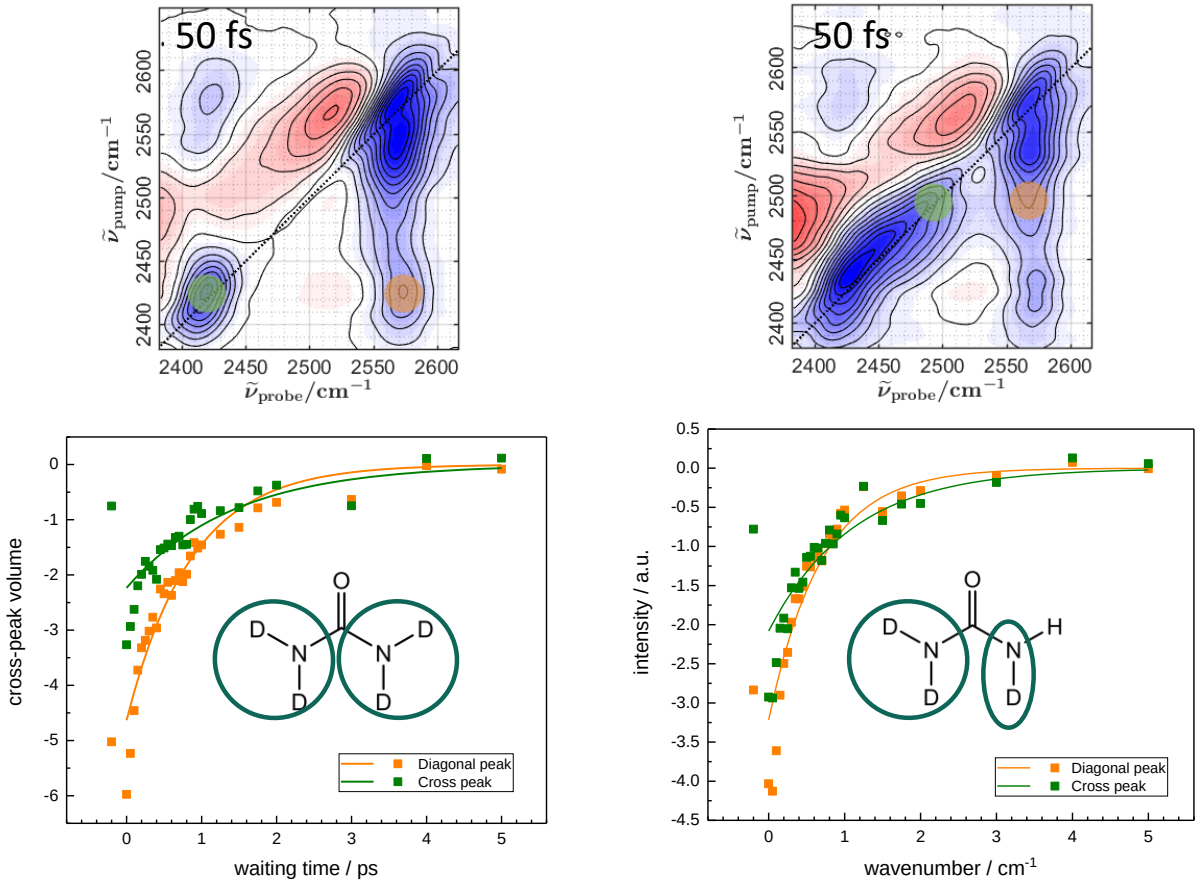

Figure 4-7: 2D-IR spectra (top) of urea-1:0 (left) and urea-7:3 (right) at a waiting time of 50fs. The colored circles illustrate the integration ranges, which were used for the integrated peak volumes shown in the bottom panels for the diagonal peak (green) and the cross peak (orange).

Infrared absorption spectra compared to pump pulse

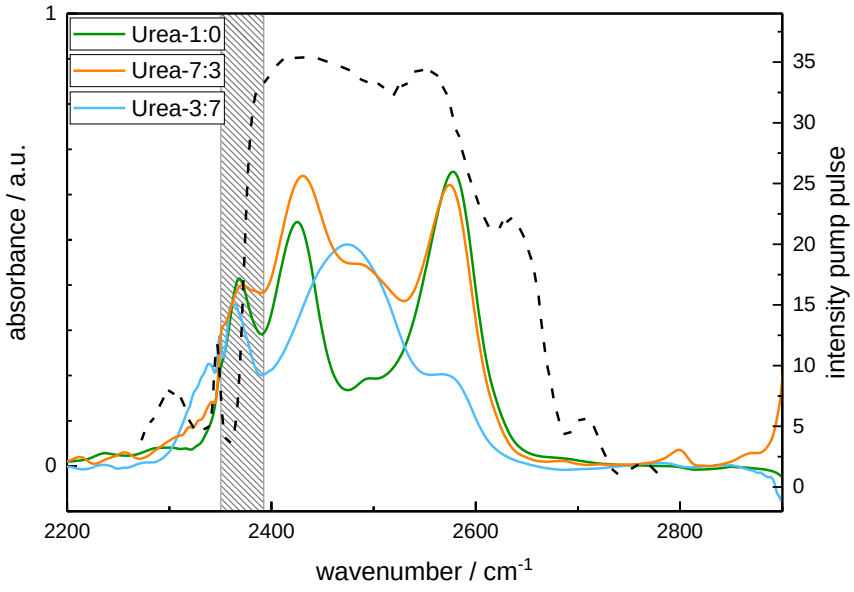

Figure 4-8: Infrared absorption spectra for solutions of $\boldsymbol{c} = 0.36$ *mol/kg, urea-1:0 (green), urea-7:3 (orange) and urea-3:7 (blue) in DMSO. The absorbance of the solvent has been subtracted from all spectra. For comparison, the intensity of the pump pulse is shown. The band at 2360cm-1 overlaps with the* CO_2 *absorption where the pump intensity is reduced. The reduced pump intensity can explain the absence of the 2360 cm-1 band in the 2D-IR spectra.*

Integration of the diagonal signals

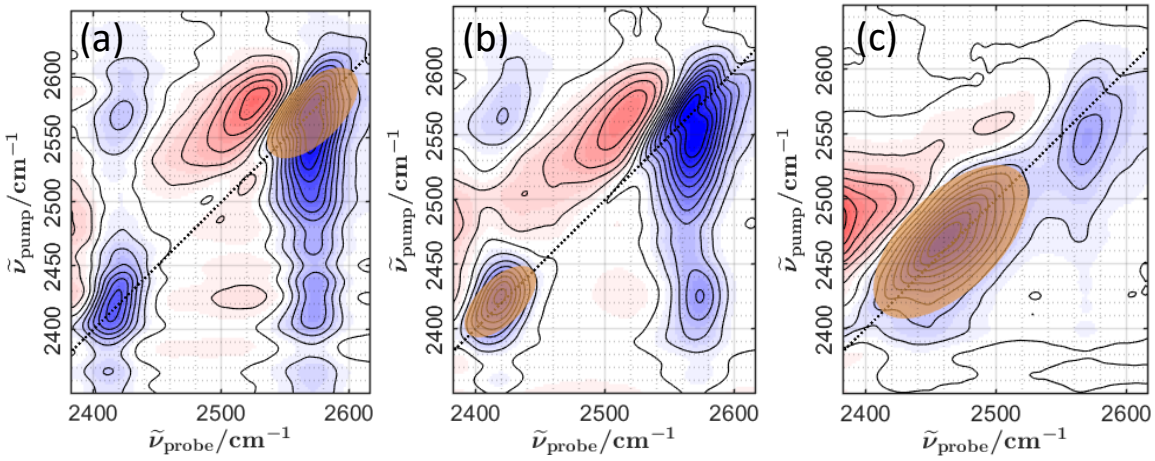

Figure 4-9: Isotropic 2D-IR spectra for solutions of $\boldsymbol{c} = 0.36$ *mol/kg urea-1:0 (a) and urea-3:7 (b and c) in DMSO at* T_w*=200 fs. The ellipses show the integration areas used to obtain the peak volumes shown in Figure 4-2d of the main manuscript.*

To determine the peak volumes for each vibration, we use an elliptical integration range at all waiting times (*Figure 4-9*). The ellipses were defined by the center along the pump axis *X0*, center along the probe axis *Y0,* major diagonal radius *R*, the ratio between the radii of the minor and the major axes *E*, and the tilt angle *Phi*. All ellipse parameters are summarized in *Table 4-2*. The intensities within the ellipses were integrated numerically.

Table 4-2: Parameters of the ellipses, which were used to determine the peak volumes shown in Figure 4-2d of the main manuscript.

Ellipse Parameters	Asymm. ND_2	Symm ND_2	ND
X0	2571.0 cm^{-1}	2419.0 cm^{-1}	2465.1 cm^{-1}
Y0	2569.6 cm^{-1}	2421.0 cm^{-1}	2467.1 cm^{-1}
R	45	35	75
E	0.5	0.5	0.5
Phi	0.7854	0.7854	0.7854

Gaussian and Lorentzian modelling of the 2D-IR slices

In *Figure 4-3* of the main manuscript we limit the discussion of the linewidths to the FWHMs of raw signals. For the antidiagonal slice, however, the superposition of the positive excited state absorption and the negative ground state bleaching signals may bias the thus determined linewidths. To estimate this bias we model the slices. For the diagonal slices we use a Gaussian peak:

$$g(\omega) = A \cdot e^{-(\frac{\omega-\omega_0}{\sqrt{2}\sigma})^2} \tag{4-2}$$

with the amplitude A, the center frequency ω_0, and the width σ. To model the antidiagonal cuts we use a combination of two Lorentzian bands:

$$l(\omega) = -C \cdot \frac{1}{(\omega-\omega_0)^2 + \left(\frac{\Gamma}{2}\right)^2} + D \cdot \frac{1}{(\omega-\omega_1)^2 + \left(\frac{\Gamma}{2}\right)^2} \tag{4-3}$$

with C and D the amplitudes of the ground state bleach and the excited state absorption, respectively. ω_0 and ω_1 are the resonance frequencies of the ground state bleaching

signal and of the excited state absorption, respectively. To reduce the parameter space, we assume the widths, Γ, of both signals to be the same.

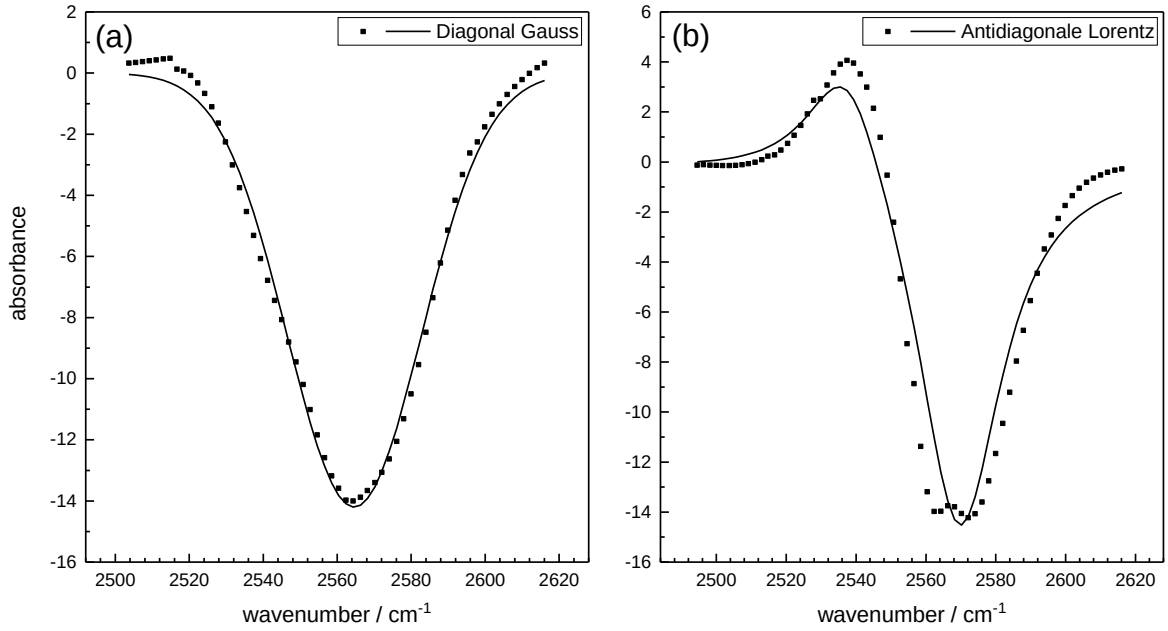

Figure 4-10: Modelling the 2D-IR slices for the antisymmetric ND_2 stretching band as shown in Figure 4-3a of the main manuscript: (a) Gaussian (solid blue line) fit to the diagonal slice (red symbols). (b) Double Lorentzian fit (solid blue line) to the antidiagonal cut (red symbols). The thus determined FWHM of 43 cm^{-1} (diagonal) and 29 cm^{-1} (antidiagonal) are close to those determined from the raw data (Figure 4-3a in the main manuscript).

As can be seen from *Figure 4-10* & *Figure 4-11*, the thus determined linewidths are nearly identical to the linewidths determined from the raw data (*Figure 4-3* of the main manuscript). As the limited probing frequency range does not allow for a reliable fitting of the linewidth of the symmetric stretching vibration (where the excited state absorption is not fully covered by our probe frequency range) we limit the discussion in the main manuscript to the FWHMs determined from the raw data.

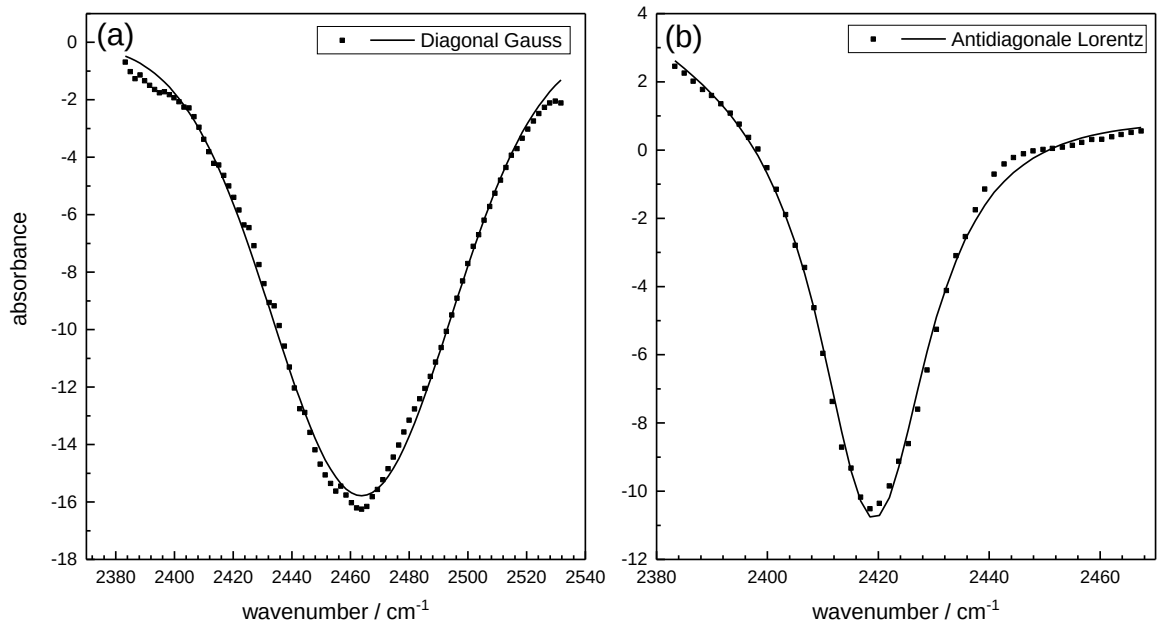

Figure 4-11: Modelling the 2D-IR slices for the ND stretching vibration shown in Figure 4-3b of the main manuscript: (a) Gaussian (solid blue line) fit to the diagonal slice (red symbols). (b) Double Lorentzian fit (solid blue line) to the antidiagonal cut (red symbols). The thus determined FWHM of 72 cm^{-1} (diagonal) and 32 cm^{-1} (antidiagonal) are close to those determined from the raw data (Figure 4-3b in the main manuscript).

Center line slopes

In *Figure 4-12a* we show the temporal evolution of the center line slopes (CLS) for the excited state absorption of the antisymmetric ND_2 vibrations of the urea-1:0 sample, for the bleaching signal of the symmetric ND_2 vibration in the urea-1:0 sample and for the N-D stretching vibration in the urea-3:7 sample. At T_w=0 the values of the CLS are all significantly lower than 1 and the value at T_w=0 for the different vibrations differ. This spread in instantaneous correlations can be explained by different contributions of intermolecular coupling between two ND_2 groups of urea-d4 molecules, depending on the studied frequency range. Notably, the CLS values for the N-D stretching mode in the urea-3:7 sample are significantly higher and decay somewhat slower, than for the ND_2 vibrations. This difference can be explained by reduced intermolecular coupling for the N-D vibration. Nevertheless, the CLS decay similarly. However, the bleaching signal of the antisymmetric ND_2 mode of urea-1:0 decays somewhat faster with T_w than the ESA (*Figure 4-12b*), which is perfectly reproducible in the urea-7:3 sample and can be explained by a slight distortion of the detected signals due to scattered pump light at early times. The CLS decay of the bleaching signal of the antisymmetric ND_2 mode for the urea-1:0 and the urea-7:3 samples are, within experimental error, the same. Overall, all

CLS decay indicate that frequency-frequency correlations decay slowly and persist longer than the experimentally accessible time window of ~1 ps.

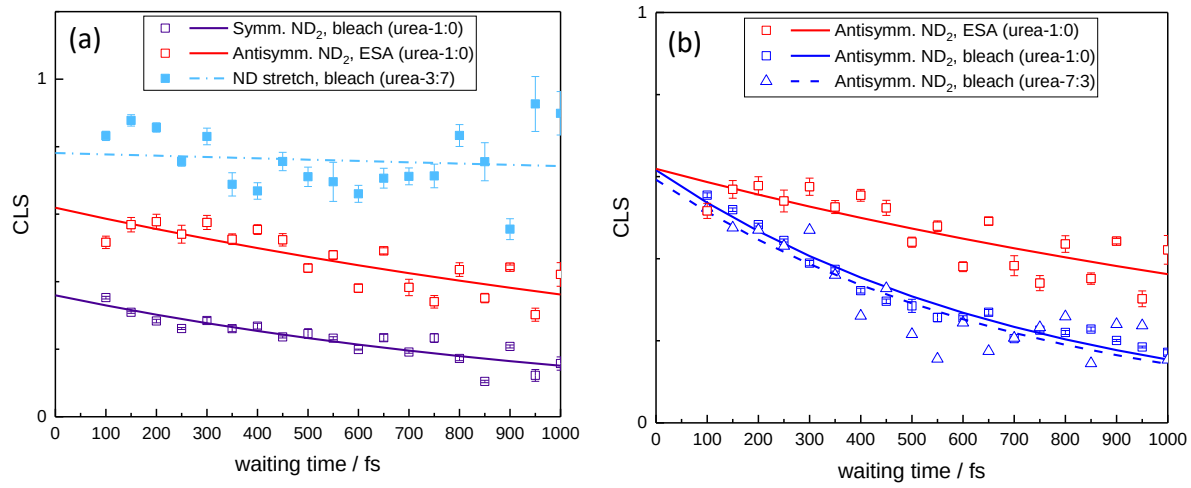

Figure 4-12: (a) The calculated center lines slopes (CLS) of the bleaching signal of the symmetric ND_2 stretching vibration for urea-1:0 (empty purple squares), for the bleaching signal of the ND stretching vibration for urea-3:7 (filled blue squares) and the ESA of the antisymmetric ND_2 stretching vibration for urea-1:0 (empty red squares). (b)The CLS values of the ESA of the antisymmetric ND_2 stretching vibration (empty red squares) for urea-1:0 compared to the bleaching signal of the antisymmetric ND_2 stretching vibration for urea-1:0 (empty blue squares) and the bleaching signal of the antisymmetric ND_2 stretching vibration for urea-7:3 (empty blue triangles). Single exponential fits to the experimental data are shown as function of waiting time (solid and dashed lines). The pump wavenumber ranges, which were used to fit the minima along the pump axis were: 2420-2440 cm^{-1} (bleach of the symmetric ND_2 stretching vibration for urea-1:0), 2575-2600 cm^{-1} (bleach for the antisymmetric ND_2 stretching vibration for urea-1:0), 2560-2590 cm^{-1} (ESA of the antisymmetric ND_2 stretching vibration for urea-1:0), 2575-2600 cm^{-1} (bleach of the antisymmetric ND_2 stretching vibration for urea-7:3), and 2475-2500 cm^{-1} (bleach of the ND stretching vibration for urea-3:7).

5 CF_3-GROUPS CRITICALLY ENHANCE THE BINDING OF THIOUREA CATALYSTS TO KETONES – A NMR AND FT-IR STUDY

Reproduced with permission and minor changes from "A. A. Ehrhard, S. Jäger, C. Malm, S. Basaran and J. Hunger, CF3-groups critically enhance the binding of thiourea catalysts to ketones – a NMR and FT-IR study, *J. Mol. Liq.*, 2019, 296, 111829". Copyright 2019, The Authors.

[redacted]

Author contributions: [redacted]

5.1 ABSTRACT

Substituted phenylthioureas have been established as efficient organocatalysts and substituents containing electron withdrawing CF_3 groups have been shown to enhance catalytic efficiency. The effect of the CF_3 groups on binding of catalysts to substrates in solution has however remained elusive. Here, we report on the effect of CF_3 substituted diphenylthioureas on the association with the substrate 1,3-diphenyl-2-propenone in solution by using a combination of nuclear magnetic resonance (NMR) and Fourier-transform infrared (FT-IR) spectroscopy. We use the ensemble-averaged chemical shift of the thiourea proton as function of substrate concentration to determine the association constants between catalyst and substrate. To experimentally discriminate between free and bound catalyst we use infrared absorption spectra, which show a red-shift of thiourea's N-H stretching vibration upon association with the substrate. With both methods, we find the association constant K to increase from $\sim$1 L/mol to $\sim$20 L/mol with increasing number of CF_3 substituents. This enhanced binding can explain the increased reaction rates observed for CF_3 substituted diphenylthiourea catalysts. For the efficient catalyst containing four CF_3-groups (Schreiner's catalyst), the strongest association is observed in toluene as a solvent, while the binding strength is somewhat weaker in dichloromethane, and association to the substrate is not detectable in acetonitrile. Our results thus demonstrate that even weak association between the thiourea catalysts and the ketone can facilitate efficient catalytic conversion. However,

the association with the ketone substrates is very susceptible to competing interactions with the solvent.

5.2 INTRODUCTION

Hydrogen-bonding donors like thioureas have been established as efficient organo-catalysts.[22-29,31,123] In particular, the wide range of catalyzed reactions, including addition, allylation, Strecker, Michael- and Nitro-Mannich reactions,[20] renders thioureas promising catalysts, which are available at relatively low costs. In particular, substituted diphenylthioureas, pioneered by Schreiner and co-workers, have been shown to provide fast reaction rates and high stereoselectivity for e.g. Diels-Alder reactions (*Figure 5-1*).[22,23]

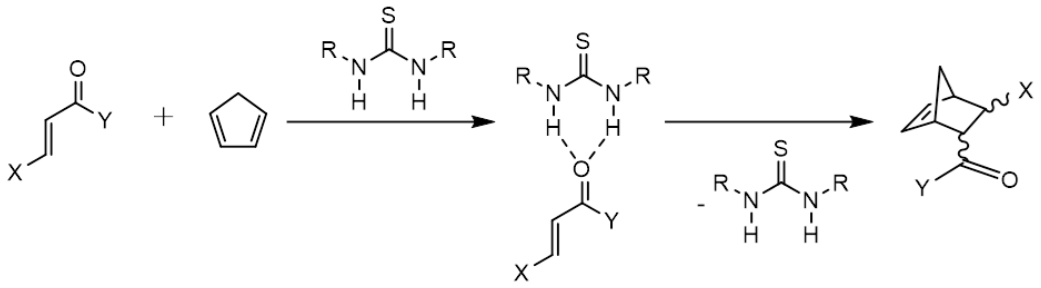

Figure 5-1: Reaction scheme of the thiourea catalyzed Diels-Alder cycloaddition. The catalyst hydrogen-bonds to the ketone, which activates the ketone. The catalyst can enhance the reaction rate and the stereoselectivity, which is determined by the electron density of the reactants and the nature of reaction (thermic or photolytic).

Electron-withdrawing CF_3-groups have been demonstrated to enhance reaction rates and yields in diphenylthiourea catalysis.[23] The enhanced catalytic activity has been related to an increase in hydrogen-bond donor ability, i.e. a reduction of the pK_a values of thiourea's N-H groups.[32] Indeed, nuclear magnetic resonance (NMR) and infrared (IR) spectroscopy experiments together with mass spectrometry and density functional theory calculations have shown that hydrogen-bonding between thiourea and ketones are the relevant interaction motif for catalysis. Remarkably, not only hydrogen-bond donation of the highly polar N-H group, but also of the ortho-proton of the phenyl group of phenylthiourea was suggested to contribute to the activation of the substrates.[30] Despite the importance of hydrogen-bonding, other contributions including dual activation, secondary interactions, and steric effects have been suggested to affect catalytic activity.[33]

Since catalyst-substrate aggregates are the relevant reactive intermediates, which determine amongst others e.g. reaction rates, energetic barriers etc., the binding strength between these thiourea catalysts and the substrates is important for catalytic activity. In principle, an enhanced catalytic activity may originate from stronger binding (substrate activation) or by the formation of more catalyst-substrate complexes. Even though these two effects are not completely independent – as a stronger hydrogen-bonding results in enhanced complex formation – the formation of catalyst-substrate bonds depends on the solvation of the catalyst, the substrate, and the complexes. For instance, reaction rates have been – rather counterintuitively – shown to be enhanced in hydrogen-bonded water, which has been ascribed to 'hydrophobic hydration'.[23,36] Thus, to understand catalytic activity and to allow for a rational catalyst design, it is vital to understand solvation and study binding strength in solution.

Here, we report on the association[173,174] of diphenylthioureas with 1,3-diphenyl-2-propenone, relevant to Diels-Alder cycloaddition (*Figure 5-1*), in solution. To study the effect of electron withdrawing CF_3-groups, we study the association of diphenylthioureas with zero, two, and four CF_3 substituents at the phenyl rings. We determine the rather weak molecular association using the motionally averaged signals of the free and the bound catalyst in the NMR spectra, which shift upon hydrogen-bond formation. [59,175,176] The thus obtained association constants are confirmed, using the N-H stretching vibration of the catalyst in the infrared absorption spectra, in which the bound and free catalyst can be spectrally resolved. Our results show, that CF_3-groups indeed enhance the binding to 1,3-diphenyl-2-propenone, however, the association markedly depends on the solvent with rather weak association in toluene and dichloromethane and virtually no interaction between catalyst and substrate in acetonitrile.

5.3 Experimental Methods

Sample preparation

Diphenylthiourea (0CF-DPTU, Fluka, >98%), N,N′-bis[4-(trifluoromethyl)phenyl]-thiourea (2CF-DPTU, TCI, >97%), N,N′−bis[3,5−bis(trifluoromethyl)phenyl]−thiourea (4CF-DPTU, TCI, >98%) and 1,3-diphenyl-2-propenone (Sigma-Aldrich, >98%) were used without further purification. The deuterated solvents used for the NMR experiments dichloromethane (DCM-d2, Deutero, 99.6%), toluene (toluene-d8, Aldrich, 99.6%), and acetonitrile (ACN-d3, Merck, 99.96%) were dried over 4 Å molecular sieves, yielding water contents of ~20 ppm (determined for DCM using Coulometric Karl Fischer titration). To remove solid residuals from the molecular sieves the deuterated solvents were filtered using a 0.2 µm Omnipore membrane filter prior to sample preparation. The non-deuterated solvents dichloromethane (DCM, Fischer Chemical, 99.98%), toluene (Fischer Chemical, 99.8%), acetonitrile (ACN, Fischer Chemical,

99.99%), which were used for infrared experiments, were used without any further purification. Solutions were prepared by weight using an analytical balance, assuming that the solution density is that of the solvent. For the NMR experiments the concentration of the catalyst was kept constant at c^0_{cat} = 0.01 mol/L (c^0_{cat} = 0.015 mol/L for 0CF-DPTU) and the concentration of the substrate was varied from c^0_{subs} = 0.005 mol/L to 0.4 mol/L. For the infrared experiments the catalyst concentration was kept constant at c^0_{cat} = 0.02 mol/L and the concentration of the substrate was increased from c^0_{subs} = 0.01 mol/L to 0.4 mol/L.

FT-IR experiments

FT-IR spectra were recorded using a Bruker Vertex 70 and the Nicolet 850 Magna IR spectrometer at a resolution of 4 cm^{-1}. The spectra were collected with a "Specac demountable Omni Cell" with the sample positioned between two CaF_2 windows separated by a 0.5 mm thick spacer.

NMR experiments

To study the strength of interaction between catalyst and substrate, we use NMR-spectroscopy, which provides information about the chemical environment. ^{1}H-NMR spectra were recorded using a Bruker 300 MHz AVANCE III spectrometer. Spectra were referenced to the residual DCM peak at 5.32 ppm, the residual toluene peak at 2.09 ppm, or the residual acetonitrile peak at 1.94 ppm. To determine the chemical shift we used the chemical shift value at the peak maximum.

5.4 Results and Discussion

Molecular association using NMR spectroscopy

To study the origin of the different catalytic activities for CF_3 substituted diphenylthioureas, we explore the association of 0CF-DPTU, 2CF-CPTU, and 4CF-DPTU with 1,3-Diphenyl-2-propenone (association equilibria are shown in *Figure 5-2*).

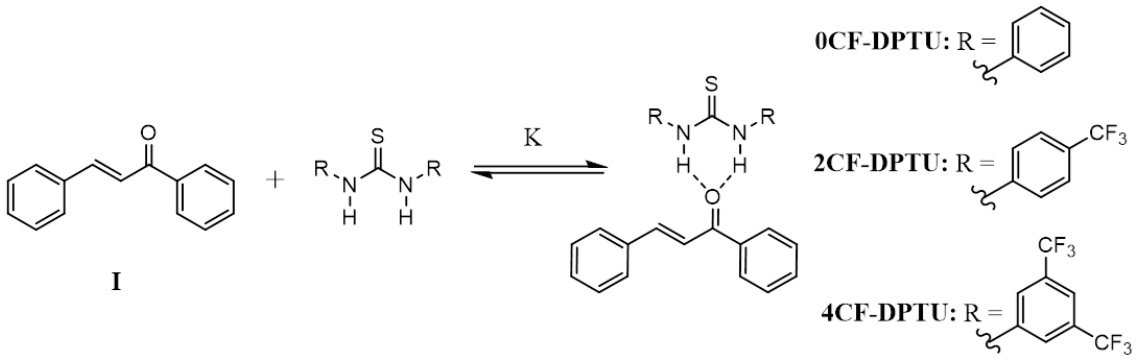

Figure 5-2: Investigated association equilibria between the thiourea catalysts and the substrate, which form a hydrogen-bonded catalyst-substrate complex.

To detect molecular association, we record the ^{1}H-NMR spectra of solutions with constant thiourea concentration (c^0_{cat} = 0.01 mol/L) and varying substrate concentration (c^0_{subs} = 0 – 0.4 mol/L). As can be seen from the NMR spectrum (*Figure 5-3*a) of a solution of only 1,3-Diphenyl-2-propenone, the substrate exhibits four narrow peaks – within the selected range at 7.7 – 8.2 ppm – due to the aromatic protons of the substrate. The spectrum for a solution of 4CF-DPTU contains two narrow peaks (at 7.94 and 7.80 ppm) due to the substituted phenyl groups and a broadened peak at 7.90 ppm due to thiourea's NH protons (*Figure 5-3*b). As can be seen in *Figure 5-3c,d*, also in the ternary mixtures the substrate and catalyst signals are observed, yet shifted with respect to their position in the binary solutions. The NH proton undergoes a marked downfield shift in the presence of the substrate. This de-shielding of the NH proton implies a reduction of the average electron density in the vicinity of the NH proton, consistent with hydrogen-bond-formation to the C=O group of the substrate. Note, that other protons e.g. of the ortho-proton of the phenyl-substituents undergo only a minor shift (*see Figure 5-9, SI*). This marked downfield shift is in line with earlier reports showing that the NH proton is very sensitive to changes in the electronic environment.[30]

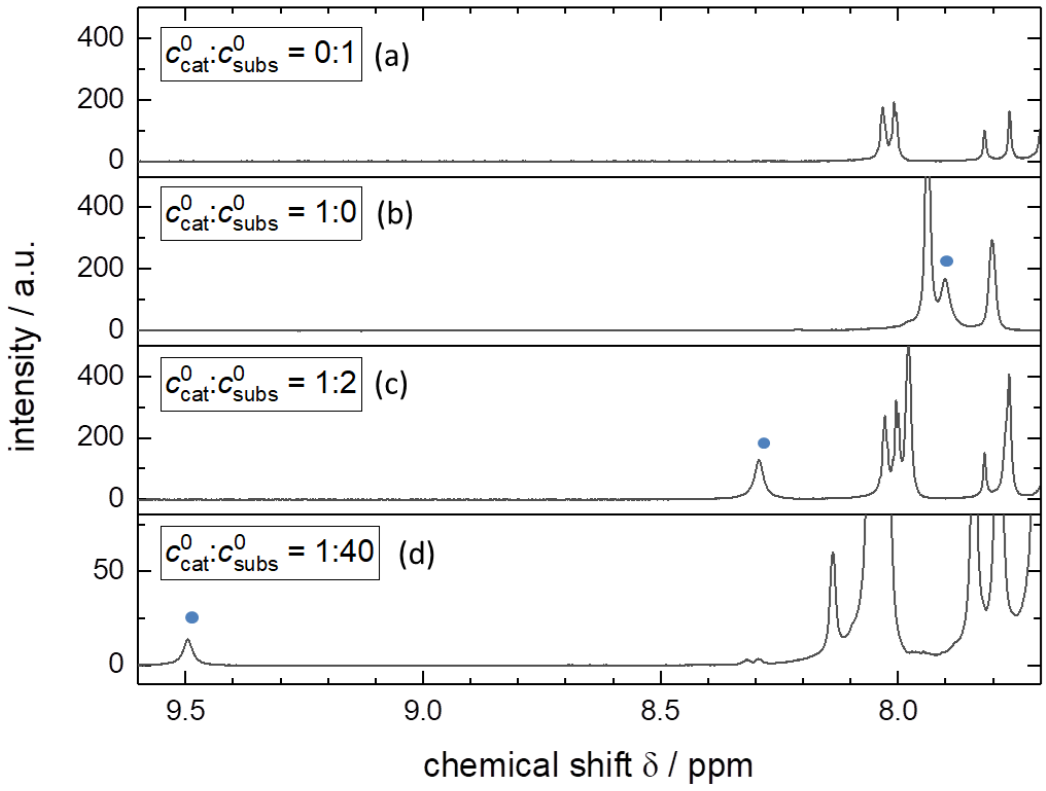

Figure 5-3: ^{1}H-NMR spectra for 4CF-DPTU (cat) and 1,3-Diphenyl-2-propenone (subs) mixtures in DCM at 7.7-9.1 ppm: (a) $\boldsymbol{c^0_{cat}}$: $\boldsymbol{c^0_{subs}}$= 0:1, (b) $\boldsymbol{c^0_{cat}}$: $\boldsymbol{c^0_{subs}}$ = 1:0, (c) $\boldsymbol{c^0_{cat}}$: $\boldsymbol{c^0_{subs}}$= 1:2, and (d) $\boldsymbol{c^0_{cat}}$: $\boldsymbol{c^0_{subs}}$= 1:40. For visual clarity the NH proton peak is marked with blue filled circle.

To quantitatively compare the variation of the chemical shift for the studied thiourea catalysts, we analyse the chemical shift of the NH protons as a function of substrate concentration. As can be seen from *Figure 5-3*, the chemical shift of the NH proton is most sensitive to the presence of the substrate. The extracted chemical shifts of the NH protons shown in *Figure 5-4* exhibit a marked increase with increasing substrate concentration for $c^0_{\mathrm{subs}} < 0.2$ mol/L, which levels off at higher concentrations of substrate for 4CF-DPTU. For 2CF-DPTU and 0CF-DPTU both the magnitude of the increase is lower and the curvature of the chemical shift as a function of c^0_{subs} is less pronounced as compared to 4CF-DPTU, indicative of weaker interaction between the thioureas and the substrate. The observed chemical shift is however due to the motionally averaged signal of the free and the bonded catalyst. Hence, a change of chemical shift can be either caused by a stronger de-shielding upon hydrogen-bond formation (larger values of the chemical shift of the hydrogen-bonded complexes), or by a higher concentration of hydrogen-bonded complexes.

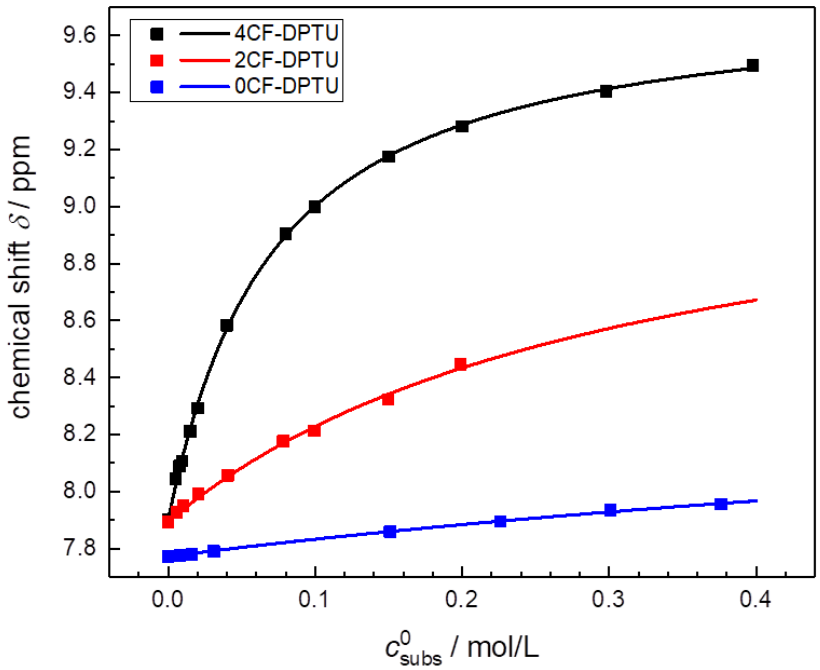

Figure 5-4: Chemical shift of the NH protons as a function of substrate concentration $\boldsymbol{c^0_{subs}}$ *for 4CF-DPTU (black symbols), 2CF-DPTU (red symbols), and 0CF-DPTU (blue-symbols) in DCM. Solid lines show fits with the association model (eqs. (5-1) and (5-2)). The catalyst concentration is kept constant at* $\boldsymbol{c^0_{cat}}$ *= 0.01 mol/L for 4CF-DPTU and 2CF-DPTU. For 0CF-DPTU the concentration of the catalyst (*$\boldsymbol{c^0_{cat}}$ *= 0.015 mol/L) was higher to enable a better discrimination between the NH signals of the catalyst and the peaks of the substrate.*

To disentangle the effect of de-shielding and complex concentration to the observed signals, we fit an association model to the experimental ^{1}H-NMR data in *Figure 5-4*. To this end, we assume a bimolecular association between the catalyst and the substrate

molecule to form a hydrogen-bonded catalyst-substrate complex (*Figure 5-2*). The corresponding association equilibrium is given as:

$$K_{\mathrm{NMR}} = \frac{[complex]}{[cat][subs]} \tag{5-1}$$

where [cat] and [subs] are the equilibrium concentrations of the free catalyst and the free substrate, respectively. [complex] is the concentration of hydrogen-bonded complexes. We assume the observed chemical shift δ to be the concentration weighted average of the chemical shift of the free catalyst, δ_{cat}, and of the chemical shift of the complex $\delta_{complex}$:

$$\delta = \delta_{\mathrm{cat}} \frac{[cat]}{c^0_{\mathrm{cat}}} + \delta_{\mathrm{complex}} \frac{[complex]}{c^0_{\mathrm{cat}}} \tag{5-2}$$

Mass conservation further gives:

$$c^0_{\mathrm{cat}} = [cat] + [complex] \tag{5-3}$$

We take the value for δ_{cat} from the c^0_{subs} = 0 samples (δ_{cat}(4CF-DPTU) = 7.90 ppm, δ_{cat}(2CF-DPTU) 7.89 ppm, and δ_{cat}(0CF-D PTU) = 7.77 ppm). Thus, eqs. ((5-1)-(5-3)) excellently describe the experimental data (see solid lines in *Figure 5-4*) with only two adjustable parameters, K_{NMR} and $\delta_{\mathrm{complex}}$. This suggests, that a bimolecular interaction dominates, as opposed to what has been found for other substrates in the solid state[177] and for asymmetric thiourea catalysts were different pathways are conceivable for a dual activation of the nucleophile and the electrophile.[40]

From the fits of eqs. ((5-1)-(5-3)) to the data, we obtain K_{NMR}(4CF-DPTU) = 15.8 $\pm$ 0.7 L/mol , K_{NMR}(2CF-DPTU) = 3.3 $\pm$ 0.3 L/mol , and K_{NMR}(0CF-DPTU) = 0.86 $\pm$ 0.03 L/mol [178] and for the chemical shift of the complex $\delta_{complex}$(4CF-DPTU) = 9.74 $\pm$ 0.02 ppm, $\delta_{complex}$(2CF-DPTU) = 9.27 $\pm$ 0.06 ppm, and $\delta_{complex}$(0CF-DPTU) = 8.54 $\pm$ 0.02 ppm,[178] respectively. Hence, the observed differences in de-shielding of the NH protons of different catalysts upon substrate addition (*Figure 5-4*) are indeed a result of both, variation of the de-shielding upon complex formation for different catalysts (variation of $\delta_{complex}$ - δ_{cat}) and varying complex concentrations. Our results suggest that 4CF-DPTU forms the strongest hydrogen-bonds to the substrate, giving rise to the highest association constant. The thus obtained association constants are also consistent with the variation of the chemical shift of other protons of the catalyst and the chemical shift of the ^{13}C carbon of the C=O group of the substrate (*see Figure 5-10 and Figure 5-11, SI*).

Association equilibria from FT-IR spectroscopy

Since the association equilibria as extracted from the NMR chemical shift may be biased by a substrate induced variation of the bulk properties of the solvent,[179] in particular for weak variation of the chemical shift (see 2CF-DPTU and 0CF-DPTU),[58] we use IR spectroscopy as an independent method to detect association.[180] In general, the NH stretching vibrations of the thiourea group are very sensitive to molecular associations, as the N-H stretching markedly red-shifts upon hydrogen-bond formation.[61]

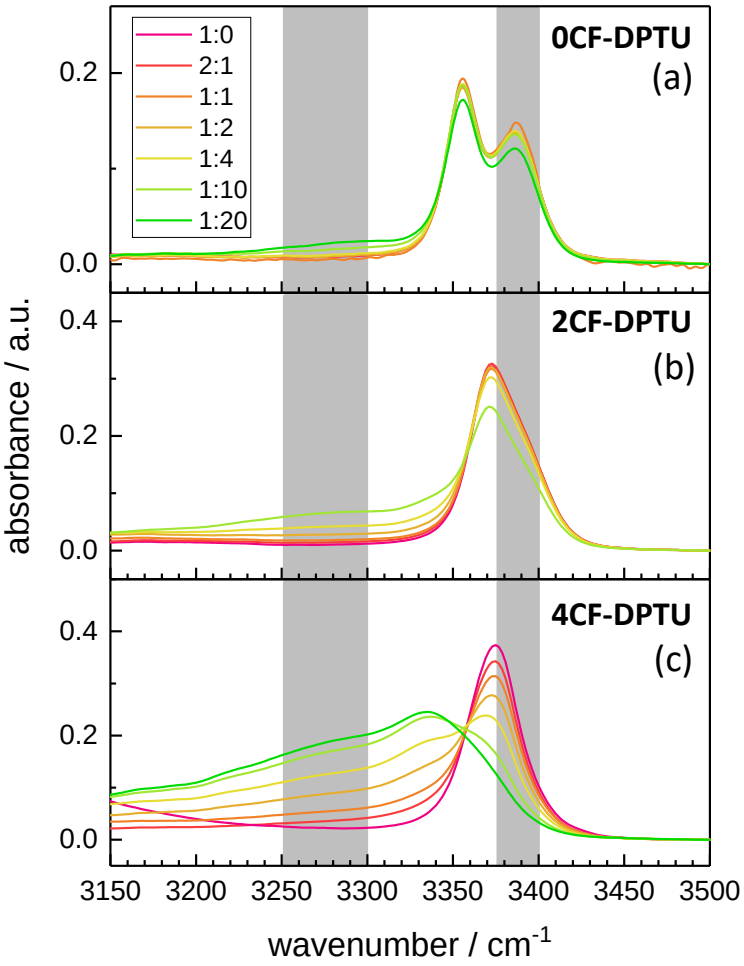

Figure 5-5: Infrared absorption spectra for solutions of $\boldsymbol{c_{cat}^{0}} = 0.02$ mol/L (a) 0CF-DPTU, (b) 2CF-DPTU, and (c) 4CF-DPTU in DCM for different DPTU:substrate (1,3-diphenyl-2-propenone) ratios. Grey areas indicate the integration ranges used for the determination of the integrated absorbance of the free and the hydrogen-bonded catalyst (see text). The absorbance of the solvent and of 1,3-diphenyl-2-propenone has been subtracted from all spectra (for details see Figure 5-12, SI).

In *Figure 5-5* we show the infrared absorption spectra for solutions of 0CF-DPTU (*Figure 5-5a*), 2CF-DPTU (*Figure 5-5b*), and 4CF-DPTU (*Figure 5-5c*) with varying substrate concentration in DCM at frequencies characteristic to the NH stretching modes (~3150 –

3500 cm^{-1}). The absorption spectrum of 0CF-DPTU in DCM exhibits two vibrational modes at 3355 cm^{-1} and 3385 cm^{-1}. For alkyl substituted thioureas the presence of two N-H stretching bands has been explained by the presence of different confomers in solution, with distinctively different vibrational frequencies for the NH stretching mode.[181,182] The two N-H stretching modes of N,N-diphenylthiourea (0CF-DPTU) have been suggested to stem from the trans-trans and trans-cis isomers.[183] Addition of the substrate hardly affects the infrared spectra at NH stretching frequencies, except for a minor reduction of the spectral amplitude of the two bands at 3355 cm^{-1} and 3385 cm^{-1} and a slight increase of the absorbance at 3180 – 3350 cm^{-1}.

The spectrum for a solution of 2CF-DPTU in DCM exhibits a single, yet asymmetric, band at 3370 cm^{-1} (*Figure 5-5b*). The asymmetric band shape, in contrast to the clear double peak structure for 0CF-DPTU, suggests different conformational equilibria and/or faster conformational dynamics[184] for 2CF-DPTU, as compared to 0CF-DPTU. Upon addition of substrate to solutions of 2CF-DPTU, the N-H stretching bands at 3370 cm^{-1} decrease in amplitude and a broad absorbance at 3180 – 3350 cm^{-1} appears. Thus, our results indicate that upon addition of substrate, catalyst-substrate complexes are formed. Formation of complexes leads to the reduced concentration of free 2CF-DPTU molecules in solution giving rise to the decrease in the absorbance at 3370 cm^{-1}. A red-shifted NH stretching band due to hydrogen-bonded catalyst-substrate complexes can explain the absorbance at 3180 – 3350 cm^{-1}.
For solutions of 4CF-DPTU, we observe only a single symmetric absorption band at ~3375 cm^{-1}, which suggests that only one catalyst conformation can be detected on the timescale of the infrared experiments. This is consistent with NMR experiments, which have revealed that the trans-trans configuration of 4CF-DPTU prevails at room-temperature and the cis-trans isomer can only be observed at temperatures below 190 K.[30] The increasing amplitude of the red-shifted catalyst-substrate band at 3180 – 3350 cm^{-1} with increasing substrate concentration is most pronounced for 4CF-DPTU.
Qualitatively, our results are in line with the association constants obtained from NMR: an increasing number of CF_3 groups results in enhanced association of DPTU with 1,3-Diphenyl-2-propenone and the associated complexes give rise to the hydrogen-bonded N-H stretching band at 3180 – 3350 cm^{-1}.

To quantitatively compare the infrared results to the findings from the NMR chemical shifts, we relate the infrared absorbances to molar concentrations. The absorbance of the free catalyst (A_{cat}) and of the complexes (A_{complex}) can be directly related to their molar concentrations, [$catalyst$] and [$complex$], via the extinction coefficients of free ($\varepsilon_{\mathrm{cat}}$) and bound catalyst ($\varepsilon_{\mathrm{complex}}$):

$$A_{\mathrm{cat}} = \varepsilon_{\mathrm{cat}} \cdot [cat] \cdot d \qquad (5\text{-}4)$$

$$A_{\text{complex}} = \varepsilon_{\text{complex}} \cdot [complex] \cdot d \tag{5-5}$$

where d is the optical path length of the sample. To obtain the extinction coefficients, we rearrange eqs (5-4) & ((5-5) such:

$$\frac{c_{\text{cat},0}}{A_{\text{complex}}} = \frac{1}{\varepsilon_{\text{cat}} \cdot d} \cdot \frac{A_{\text{cat}}}{A_{\text{complex}}} + \frac{1}{\varepsilon_{\text{complex}} \cdot d} \tag{5-6}$$

that the inverse extinction coefficients can be obtained from the slope and the intercept of a linear regression ($\frac{c_{\text{cat},0}}{A_{\text{complex}}}$ vs $\frac{A_{\text{cat}}}{A_{\text{complex}}}$). For this analysis, we use the integrated absorbance at 3375-3400 cm^{-1} for A_{cat} and the integrals at 3250 – 3300 cm^{-1} for A_{complex} (see grey areas in *Figure 5-5*). Note, that these frequency ranges do not cover the entire NH stretching bands shown in *Figure 5-5*, in order to omit the spectral range where the contributions of free and bound catalyst overlap. Thus, also the obtained extinction coefficients are characteristic to the selected frequency range. In case of 0CF-DPTU the selected frequency range only covers the blue-shifted part of the split band. Given that the two bands stem from the presence of different conformers, we assume that the selected frequency range is representative of both conformers, which is valid for fast conformational exchange.

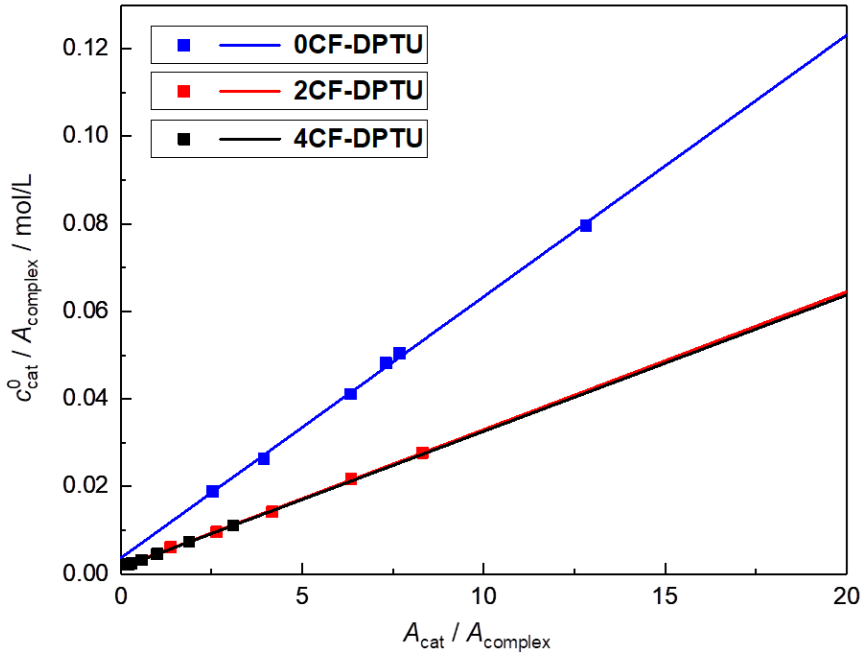

Figure 5-6: Linear regression according to eq. (5-6) to obtain the extinction coefficient of the N-H stretching bands for the bound and the free catalyst.

Using these values for A_{complex} and A_{cat}, the linear relation of eq (5-6) describes the experimental quantities very well (*Figure 5-6*). We note, that the slopes, which are proportional to the inverse extinction coefficients of the free catalysts, are similar for 2CF-DPTU and 4CF-DPTU. For 0CF-DPTU the slope is ~2 times higher, which can be explained by the double peak structure of the NH stretching band as this peak splitting results in a reduced apparent extinction coefficient for 0CF-DPTU within the selected frequency range.

With the thus obtained values for $\varepsilon_{\mathrm{cat}}$ and $\varepsilon_{\mathrm{complex}}$, we determine the degree of association α (see also *Figure 5-13,* SI):

$$\alpha = \frac{[complex]}{c^0_{\mathrm{cat}}} \tag{5-7}$$

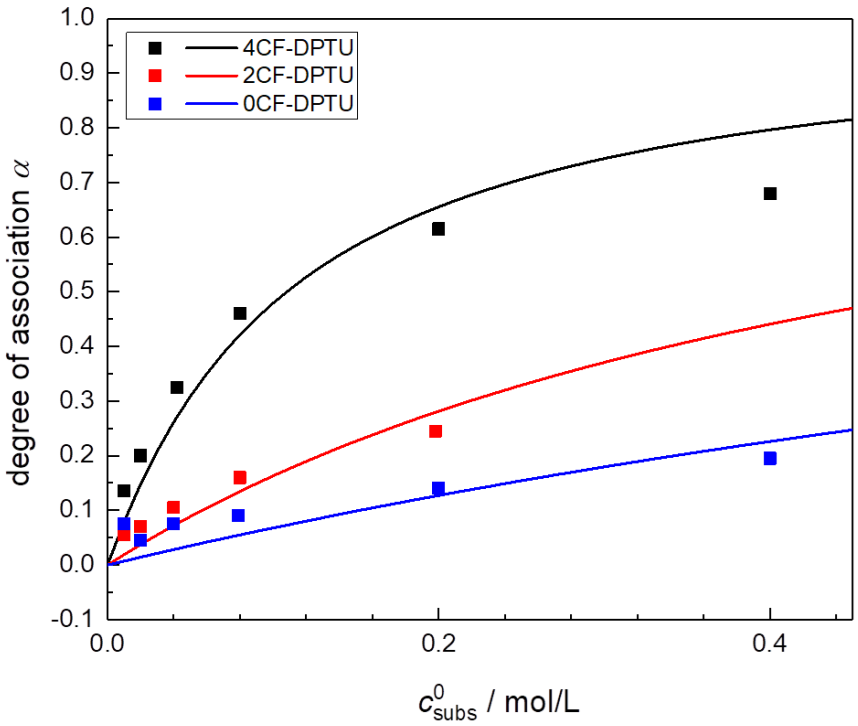

Figure 5-7: Degree of association $\boldsymbol{\alpha}$*, as obtained from the IR experiments (for details see text) for 4CF-DPTU (black symbols), 2CF-DPTU (red symbols) and 0CF-DPTU (blue symbols) in DCM (*$\boldsymbol{c^0_{\mathrm{cat}}}$ *= 0.02 mol/L). Solid lines show fits using the bimolecular association model eq (5-1).*

In line with our NMR results, α increases with increasing c^0_{subs} and association is stronger with increasing number of CF_3 groups (*Figure 5-7*). For a quantitative comparison to our NMR results we fit the bimolecular association model eq (5-1) to the

data in *Figure 5-7*, which describes the variation of α with c^0_{subs} well. The somewhat larger deviations of the data from the model at higher concentrations may stem from the partially overlapping IR bands of the free catalyst and the complex. We thus obtain the association constants K_{IR}, (K_{IR}(4CF-DPTU) = 10.2 ± 5.2 L/mol, K_{IR}(2CF-DPTU) = 2.0 ± 0.7 L/mol, and K_{IR}(0CF-DPTU) = 0.7 ± 0.4 L/mol).[178] In contrast to the NMR results (see $\delta_{complex}$ values above), we find no evidence for the spectra of the complexes to differ significantly for the three DPTUs (see *Figure 5-14,* SI).

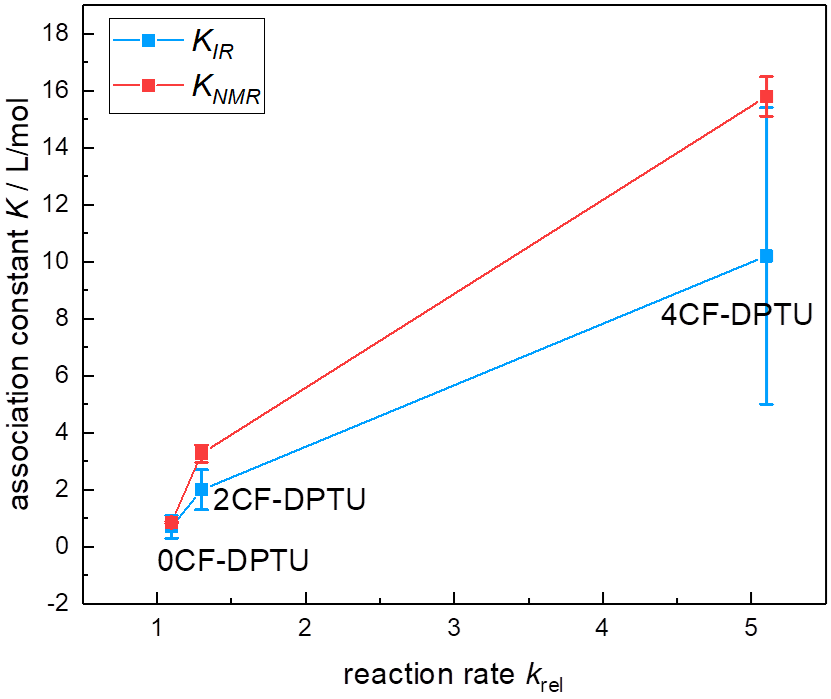

Figure 5-8: Association constants K_{IR} and K_{NMR} vs relative rate constants of a Diels Alder reaction as reported in ref [23]. Error bars correspond to K values for which the sum of the squared deviations increases by 100% when fitting eq (5-1) to the experimental data.

As can be seen in *Figure 5-8*, the association constants determined with both techniques agree well within the experimental error. More importantly, they correlate well with the reaction rates k_{rel} (relative increase of the reaction rate as compared to the absence of a catalyst) reported[23] for the Diels-Alder reaction of 1,3-diphenyl-2-propenone with cyclopentadiene (10-fold excess) in $CDCl_3$ catalyzed by 1 mol% 0CF-DPTU, 2CF-DPTU, or 4CF-DPTU. Thus, our results suggest that the enhanced catalytic conversion for CF_3 substituted DPTU catalysts originates from enhanced substrate binding. Our NMR experiments provide evidence for the enhanced association to originate – at least in part – from stronger N-H···O hydrogen-bonds, as the $\delta_{complex}$, which is predominantly effected by the local chemical environment, is shifted to higher values with increasing number of CF_3 groups. However, given the weak association of DPTU with 1,3-diphenyl-2-propenone, the chemical shift values of the complexes rely on extrapolation and are as such less certain. In fact, the N-H stretching bands, which are – similar to O-H stretching

frequencies[185] – also a measure for the hydrogen-bond strength, are little affected by the presence of the CF_3 groups (see *Figure 5-14*, SI), indicative of different experimental sensitivities of NMR and IR. Nevertheless, the weak variation of the NH stretching band within the complexes across the studied DPTUs suggests that the intermolecular hydrogen-bond is not the sole cause for enhanced binding of 4CF-DPTU to the substrate. Additional, interaction of the ortho-proton of the phenyl group of phenylthiourea[30] with the substrate can comprise an additional interaction motif (see also *Figure 5-9,* SI) and also reduced solvation of the CF_3-substituted DPTU molecules may give rise to enhanced complex formation.

Solvent effects

As differences in the solvation of the substrate, catalyst, and complexes in different solvents may give rise to different association, and thus different catalytic conversion, we investigate the effect of the solvent on the association.

Comparing our results for solutions in DCM to the association of DPTUs with 1,3-diphenyl-2-propenone in toluene, which is a commonly used solvent in catalysis, yet with lower polarity. Accordingly, we determine the K_{NMR} values from the ^{1}H-NMR chemical shifts (see *Figure 5-15, SI*) in toluene.[186] As can be seen from the comparison of the determined values of the K_{NMR} (*Table 5-1*), the association strengths are comparable for 0CF-DPTU and 2CF-DPTU in toluene to those found in DCM. For 4CF-DPTU, however, association is enhanced in toluene as compared to DCM. The enhanced association of 4CF-DPTU with 1,3-diphenyl-2-propenone in toluene as compared to DCM points towards a less favorable interaction between the catalysts NH groups and the solvent in toluene as compared to DCM.

Conversely, in the highly dipolar solvent acetonitrile, we find the chemical shift of the NH protons DPTUs of all DPTUs to hardly vary with increasing concentration of 1,3-diphenyl-2-propenone (see *Figure 5-16, SI*). Hence, no appreciable association between the DPTUs and the substrate in acetonitrile can be detected, which is further confirmed by the insensitivity of the catalysts NH stretching band to the substrate concentration in infrared absorption experiments (see *Figure 5-17, SI*). This suggests that the polarity of the solvent, as for instance determined via the $E_{\mathrm{T}}(30)$ values,[187] is a reasonable estimate for the association strength of the DPTUs with ketones in organic (non-hydrogen-bonding) solvents. In general, binding of catalyst and substrate are markedly affected by the solvent, which suggests that solvation of the catalyst and substrate plays an important role for the formation of the reactive intermediates in catalysis. This is particularly apparent for 4CF-DPTU, for which association is strongly enhanced in toluene. [176]

Table 5-1: Association constants, $K_{NMR,}$ in DCM and toluene, as obtained from ^{1}H-NMR spectroscopy for the catalysts 0CF-DPTU, 2CF-DPTU and 4CF-DPTU, respectively.

K_{NMR}	4CF-DPTU	2CF-DPTU	0CF-DPTU
CD_2Cl_2	15.8 ± 0.7 L/mol	3.27 ± 0.3 L/mol	0.86 ± 0.03 L/mol
Toluene	27.7 ± 1.3 L/mol	3.06 ± 0.1 L/mol	1.65 ± 0.2 L/mol

5.5 CONCLUSIONS

We use two independent techniques, NMR and FT-IR spectroscopy to quantify the association strength of diphenylthiourea-based catalysts with 1,3-diphenyl-2-propenone as a representative substrate in solution. We find bimolecular association to suffice to describe both infrared and NMR experimental findings. Despite the challenges in determining weak association equilibria, the interaction strengths determined by both methods agree very well. We find that with an increasing number of CF_3 substituents from 0CF-DPTU to 4CF-DPTU the association constant increases from ~1 L/mol to ~20 L/mol. This increase in molecular association correlates well with the reported increased catalytic activity of the DPTU-based catalysts. Our results suggest that the hydrogen-bond strength of the N-H···O=C bonds in the catalyst-substrate complexes is not the sole origin of the enhanced binding in solution for CF_3 substitued DPTUs but also the solvation of the catalyst, substrate and the complexes seem to contribute. The relevance of the solvation is supported by the marked dependence of the association equilibria on the solvent, with no detectable binding in solutions of acetonitrile and moderate interactions in toluene and dichloromethane.

5.6 SUPPORTING INFORMATION

^{1}H-NMR spectra of 4CF-DPTU + 1,3-Diphenyl-2-propenone mixtures in DCM

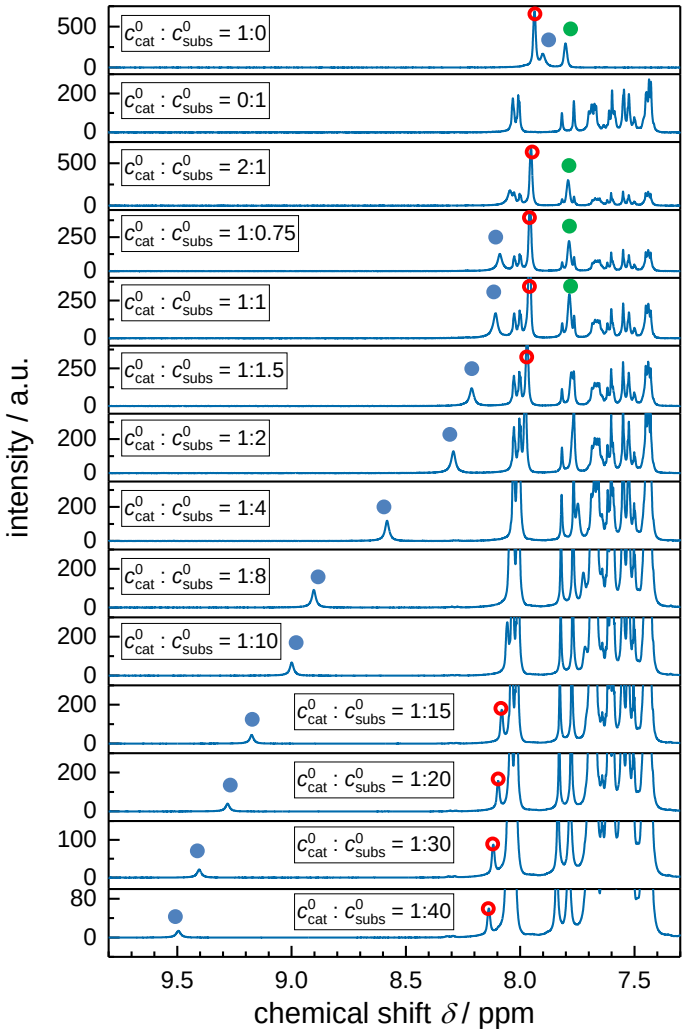

Figure 5-9: ^{1}H-NMR spectra for 4CF-DPTU (cat) and 1,3-Diphenyl-2-propenone (subs) mixtures in DCM. The chemical shift of the NH-, the ortho- and the para-proton of 4CF-DPTU are marked with a blue circle (NH), red circle (ortho) and green circle (para), respectively. The change of chemical shift of the ortho- and para protons is less pronounced than for the NH proton.

Association constants from the chemical shift of the ortho- and para protons of 4CF-DPTU and ^{13}C chemical shifts of 1,3-diphenyl-2-propenones C=O group

In *Figure 5-10* we show the ^{13}C chemical shift of the carbonyl carbon atom of the substrate with varying substrate concentration c^0_{subs} for a solution of 0.01mol/L 4CF-DPTU in DCM. We find the variation of the chemical shift to be consistent with the association equilibria as extracted from the ^{1}H-NMR results (*Figure 5-4* of the main manuscript): Using K_{NMR}(4CF-DPTU,DCM) = 15.8 L/mol the experimental ^{13}C data can be excellently described using eq (5-8):

$$\delta = \delta_{\mathrm{subs}} \frac{[subs]}{c^0_{\mathrm{subs}}} + \delta_{\mathrm{complex}} \frac{[complex]}{c^0_{\mathrm{subs}}} \qquad (5\text{-}8)$$

with δ_{subs}=190.57 ppm and $\delta_{\mathrm{complex}}$=196.76 ppm.

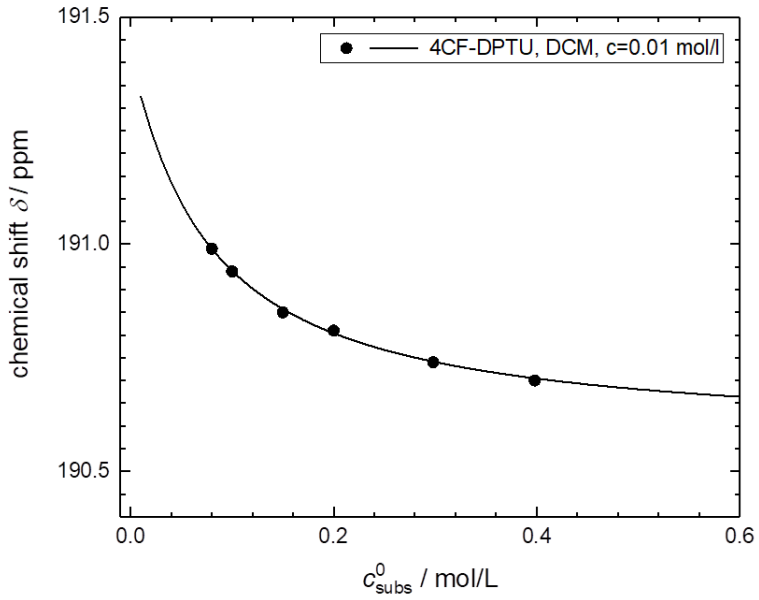

Figure 5-10: ^{13}C Chemical Shift of the carbon of the carbonyl group of the substrate as a function of substrate concentration $\boldsymbol{c^0_{subs}}$*. Solutions in DCM contained a constant concentration of 0.01 mol/L 4CF-DPTU. The symbols represent the experimental data and the solid lines show the association model (eq. (5-1) and eq. (5-8) with a fixed value of* K_{NMR} = $\boldsymbol{15.8\ L/mol}$.

Similar to our analysis of the chemical shift of the NH proton in the main manuscript, the variation of the ortho- and the para-protons of 4CF-DPTU with substrate concentration can be used to extract the association equilibria. In analogy to the analysis shown in *Figure 5-4* of the main manuscript, we also extract *K* values from these data. Using the ortho-proton we find K = 16.6 L/mol, in excellent agreement with the value extracted

from the NH protons (*Figure 5-11*). The para-proton, which is most distant from the hydrogen-bonding NH group, exhibits the least variation of the chemical shift. From this variation we extract (*Figure 5-11*) $K = 25.3\ L/mol$, which is somewhat higher than the value extracted from the ortho- and the NH protons. Given the low sensitivity of the chemical shift of the para-protons to intermolecular binding, this value is still consistent with the association constants determined from the chemical shifts of the ortho- and the NH-proton.

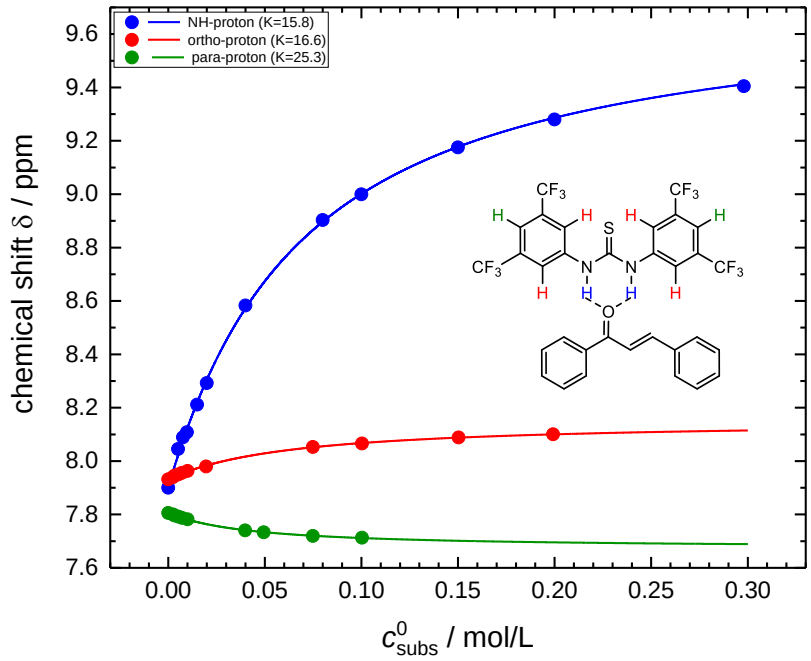

Figure 5-11: Chemical shift of the NH protons (blue), ortho-protons (red) and para-protons (green) as a function of substrate concentration, $\boldsymbol{c^0_{subs}}$ for 4CF-DPTU at a constant catalyst concentration ($\boldsymbol{c^0_{cat}}$ = 0.01 mol/L) in the solvent DCM. Solid lines show fits with the association model (eqs. (5-1) and (5-2)).

Background subtraction from FT-IR spectra

In *Figure 5-5* of the main manuscript, we show FT-IR spectra corrected for background absorption due to the solvent and due to the substrate. The raw spectra (before subtraction) are shown in *Figure 5-12.* To account for the background, we subtract the spectrum of the solvent from all samples. The FT-IR spectra of the pure substrate (blue dashed-dotted line in *Figure 5-12*) reveals a structured absorption at the frequencies characteristic to the NH stretching band of thiourea. To remove these contributions, we subtract a concentration weighted infrared spectrum at a high substrate concentration from the sample spectra. All spectra are additionally corrected for a constant offset due to reflection losses.

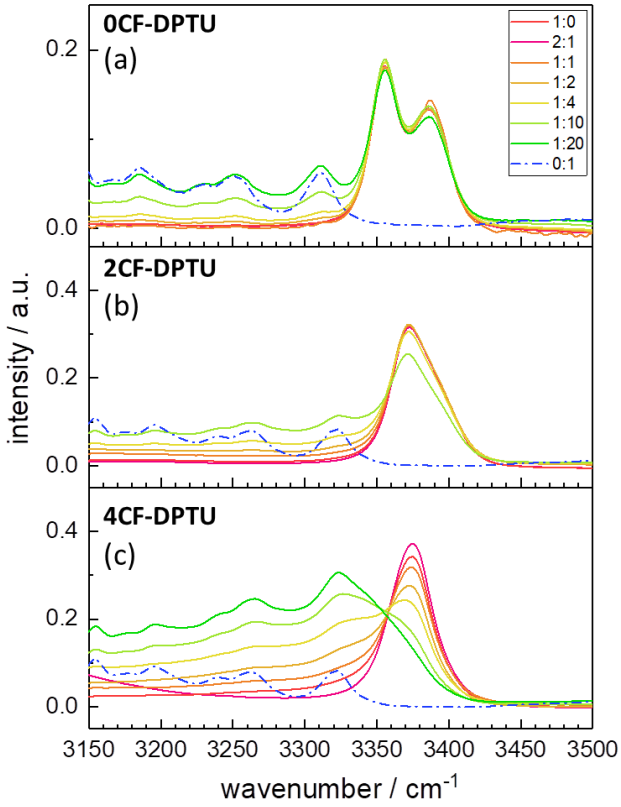

Figure 5-12: Raw FT-IR spectra of the catalysts 0CF-DPTU (a), 2CF-DPTU (b) and 4CF-DPTU (c) upon association with the substrate in DCM. Solutions of only the substrate in DCM (blue dashed-dotted) exhibit a structured absorption overlapping with the frequency range, where we observe the hydrogen-bonded NH-stretching vibration.

Degree of association from IR spectra

From the analysis in *Figure 5-6* of the main manuscript, we obtain the extinction coefficient of both, $\varepsilon_{\mathrm{cat}}$ and $\varepsilon_{\mathrm{complex}}$. Accordingly, the degree of association, α, can be determined from both the absorbance of the catalyst-substrate complexes (eq (5-7) of the main manuscript) or the absorbance of the free catalyst $\alpha = \frac{c_{\mathrm{cat}}^{0} - [cat]}{c_{\mathrm{cat}}^{0}}$. As can be seen from *Figure 5-13*, both values agree very well and yield very similar association constants.

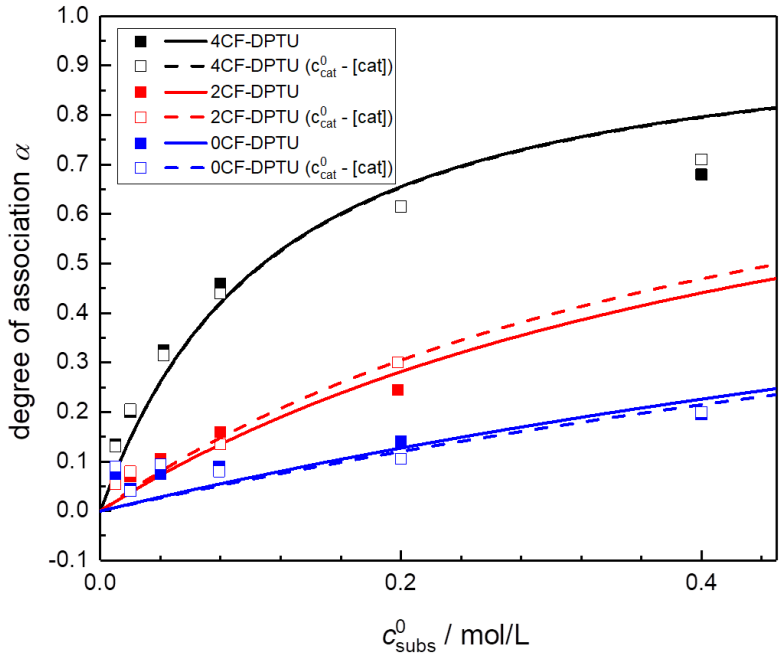

Figure 5-13: Degree of association, α, as obtained from the IR experiments for 4CF-DPTU (black symbols), 2CF-DPTU (red symbols) and 0CF-DPTU (blue symbols) in DCM ($\boldsymbol{c^0_{cat}}$ = 0.02 mol/L). Solid lines show fits using the bimolecular association model (eq (5-1), main manuscript) to $\boldsymbol{\alpha = \frac{[complex]}{c^0_{cat}}}$ values (filled symbols) and dashed lines show fits to $\boldsymbol{\alpha = \frac{c^0_{cat} - [cat]}{c^0_{cat}}}$ values (open symbols). Note, that in case of 4CF-DPTU the two fits overlap.

Vibrational spectra of catalyst-substrate complexes

To isolate the vibrational spectra of the catalyst-substrate complexes, we subtract scaled spectra of the neat catalyst in solution from the spectrum with a molar ratio of catalyst:substrate (1:10) such that the absorbance at >3400cm^{-1} remains positive. These spectra for 0CF-DPTU (blue), 2CF-DPTU (red) and 4CF-DPTU (black) are shown in *Figure 5-14* and reveal that the band shape of the catalyst-substrate complexes is quite similar for the three catalysts. The similarity suggests that the strength of the hydrogen-bonds of the catalyst is comparable.

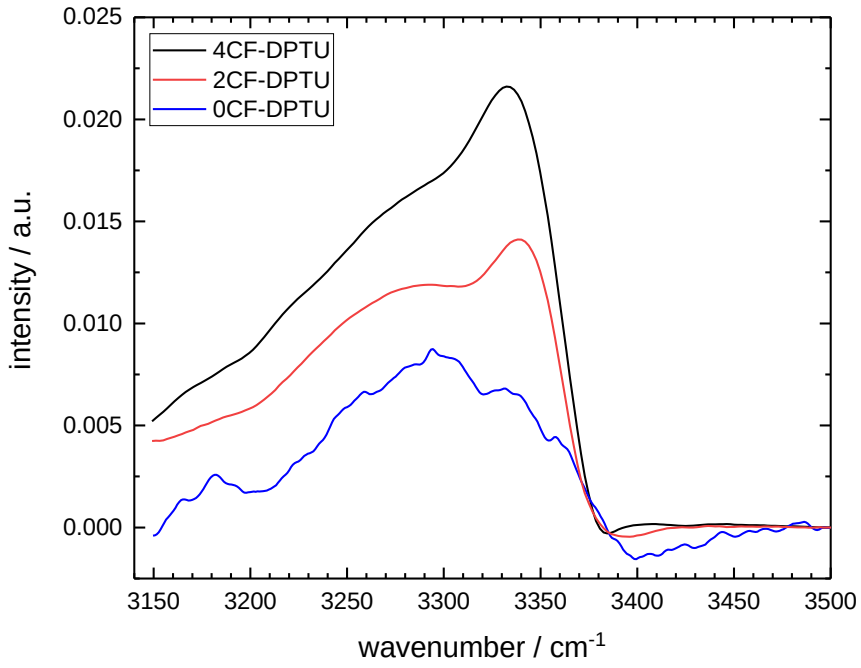

Figure 5-14: FT-IR spectra of the catalyst-substrate complex with 4CF-DPTU (black), 2CF-DPTU (red) and 0CF-DPTU (blue) for a molar ratio of catalyst:substrate (1:10). For details see text.

Association equilibria as obtained from NMR in toluene

The change of the chemical shift of the NH-proton of 4CF-DPTU (black), 2CF-DPTU (red) and 0CF-DPTU (blue) as a function of increasing substrate concentration c^0_{subs} in the solvent toluene is shown in *Figure 5-15*. The largest variation of the chemical shift is observed for 4CF-DPTU and the smallest change for 0CF-DPTU. The association model fit (eq. (5-1) and eq. (5-2) of the main manuscript, solid lines in *Figure 5-15*) yields K_{NMR}(4CF-DPTU) = 27.7 $\pm$ 1.3 L/mol , K_{NMR}(2CF-DPTU) = 2.98 $\pm$ 0.1 L/mol , and K_{NMR}(0CF-DPTU) = 1.65 $\pm$ 0.2 L/mol and the chemical shift of the complex as $\delta_{\mathrm{complex}}$ (4CF-DPTU)= 9.54 $\pm$ 0.04 ppm , $\delta_{\mathrm{complex}}$ (2CF-DPTU)= 10.46 $\pm$ 0.03 ppm and $\delta_{\mathrm{complex}}$(0CF-DPTU)= 8.89 $\pm$ 0.07 ppm, respectively. The measured chemical shifts of the free catalyst, which are used for the fit are δ_{cat}(4CF-DPTU) = 6.59 ppm, δ_{cat}(2CF-DPTU) = 6.98 ppm and δ_{cat}(0CF-DPTU) = 7.77 ppm. Note, that for 2CF-DPTU the signal of the NH overlaps with the solvent peak at 6.98 ppm and we thus take this value as δ_{cat}.

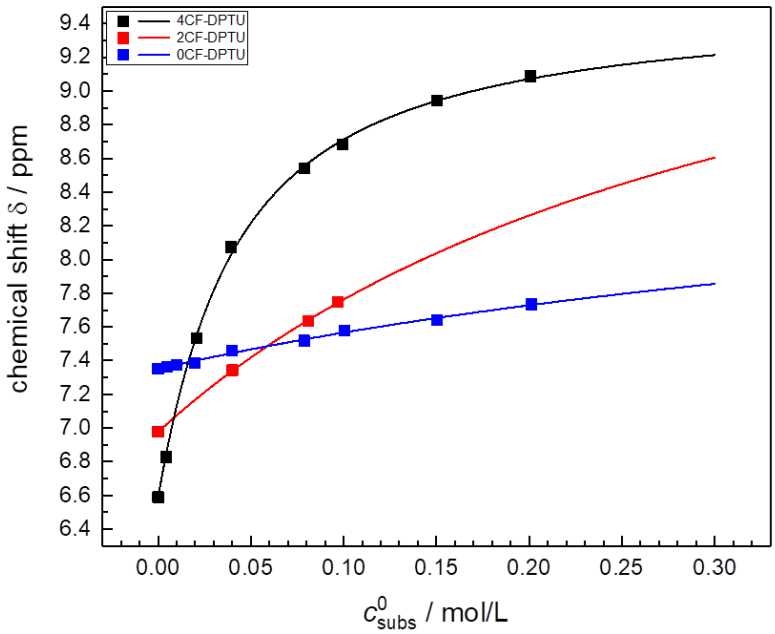

Figure 5-15: Chemical shift of the NH proton as a function of substrate concentration, $\boldsymbol{c^0_{subs}}$ for 4CF-DPTU (black symbols), 2CF-DPTU (red symbols), and 0CF-DPTU (blue-symbols) at a constant catalyst concentration ($\boldsymbol{c^0_{cat}}$ = 0.01 mol/L) in the solvent toluene. Solid lines show fits with the association model (eq. (5-1) and (5-2) of the main manuscript).

NMR and FT-IR spectra of 4CF-DPTU + 1,3-Diphenyl-2-propenone in ACN

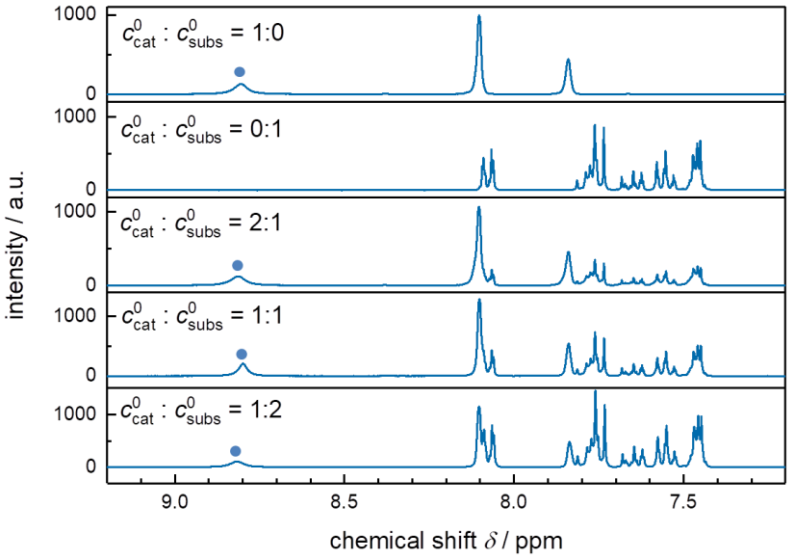

Figure 5-16: ^{1}H-NMR spectra for 4CF-DPTU (cat) and 1,3-Diphenyl-2-propenone (subs) mixtures in ACN. The chemical shift of the NH protons (blue circle) at ~8.8ppm is found independent of substrate concentration, indicating no appreciable association of the catalyst with the substrate.

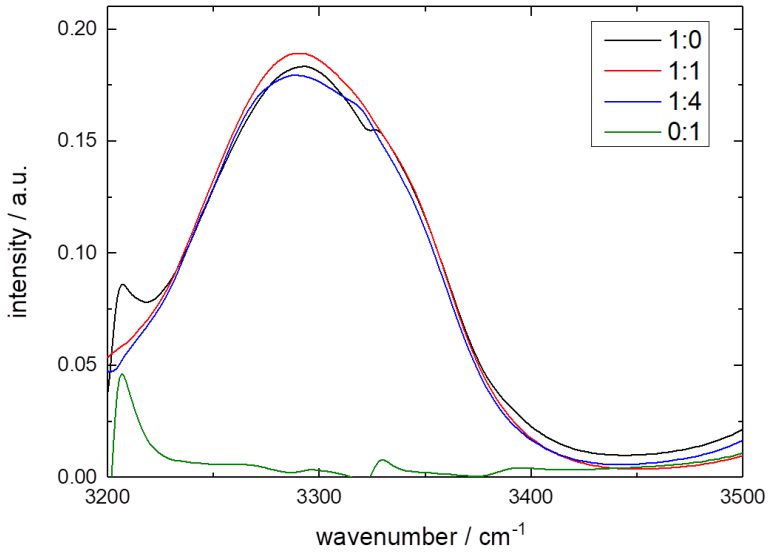

Figure 5-17: Infrared absorption spectra for solutions of $\boldsymbol{c_{cat}^{0}} = 0.02$ mol/L 4CF-DPTU (cat) in ACN for different DPTU:substrate (1,3-Diphenyl-2-propenone) ratios.

6 VIBRATIONAL DYNAMICS OF THIOUREA CATALYSTS IN SOLUTION: INFLUENCE OF CONFORMATION AND H-BONDING TO SUBSTRATES

A. A. Ehrhard, S. Jäger, A. Sell and J. Hunger, "Vibrational Dynamics of Thiourea Catalysts in Solution: Influence of Conformation and H-bonding to Substrates". This Paper manuscript is in preparation.

[redacted]

Author contributions: [redacted]

6.1 ABSTRACT

Substituted diphenylthioureas are a prominent class of efficient organocatalysts and have been shown to exist in different conformations. Yet, the relation between the conformational state and catalytic activity has remained elusive. Here, we investigate the different states of catalytically active thioureas in solution and study the effect of the substrates diphenylpropenone and acetophenone as representative catalytic substrates using a combination of ^{1}H-NMR, FT-IR and femtosecond infrared spectroscopy (fs-IR). For all catalysts in solution, we find two distinct N-H stretching modes, which can be distinguished based on their different vibrational lifetimes and assigned to two different conformers. Using the NMR chemical shift of the N-H proton, we determine the average association strength of the studied catalysts to the ketone substrates. Hydrogen-bonding association of thiourea to these ketones, which are suggested to be the reactive intermediates, gives rise to a spectrally separated, red-shifted N-H stretching band and weakens the C=O band of the ketone. We show that in mixtures of catalyst and substrate, the three molecular states – trans-trans, trans-cis, and thiourea-ketone complexes – can be resolved owing to their different vibrational lifetime. Yet, the thus obtained spectra of only one conformer and the hydrogen-bonded complexes 'spectrally mix', which points at chemical exchange and/or coupling between these two species. As such, our data

suggest that only one conformer forms hydrogen bonds to the ketone substrate on the ~10 ps timescale of our experiment. The observation of conformation-specific hydrogen-bonding dynamics implies that the design of conformationally stable catalysts may help to improve the performance of thiourea catalysts.

6.2 INTRODUCTION

A popular class of organic hydrogen-bonding catalysts, which are used in a wide variety of organic transformations, are (thio)urea catalysts, [17,18,20,21,35,38,188,189] for which the NH group is utilized as hydrogen-bonding donor for the activation of electrophiles. [20,34] The relative rate constants of these catalytic reactions are critically influenced by thiourea's substituents, rather than by the change of the reactant or the solvent:[23] Trifluoromethyl substitution of bisphenylthiourea greatly enhances reaction rates and yields. The 3,5-bis(trifluoromethyl)phenyl group, which has been introduced as a structural key motif in 2002, [22] is nowadays used in a wide range of applications as it has certain advantages for organocatalysis, including enhanced reaction rates and yields. [23,190] Amongst others, the increased acidity of the catalyst, [32] pi-pi interactions [21,191] and the involvement of the highly polar ortho-proton have been suggested to improve catalytic performance.[30]

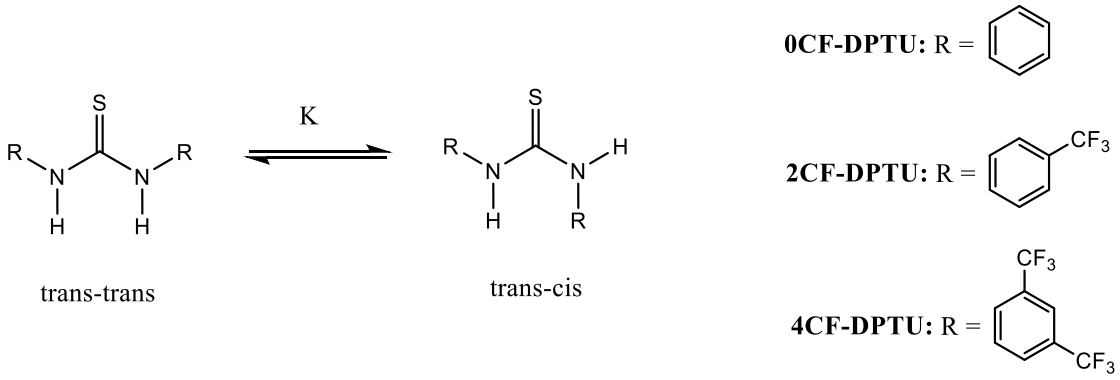

Figure 6-1: Trans-trans and trans-cis conformation of the studied diphenylthiourea (DPTU) based catalysts, containing zero (0CF-DPTU), two (2CF-DPTU) and four (4CF-DPTU) CF_3-groups.

It was found that for substituted thioureas different conformations are possible, whereas the thioamide hydrogen and the thiocarbonyl sulfur are in a cis or a trans configuration with respect to each other (*Figure 6-1*).[181] For the here studied diphenylthiourea (DPTU) based catalysts with different side groups (4CF-DPTU, 2CF-DPTU and 0CF-DPTU) the trans-trans and the trans-cis configuration are conceivable. Yet, trifluoromethyl substitution has been suggested to affect conformational equilibria: A combined study using low-temperature nuclear magnetic resonance (NMR) and

infrared (IR) techniques together with density functional theory (DFT) calculations has suggested that the 3,5-bis(trifluoromethyl)phenyl substituted diphenylthiourea (4CF-DPTU) prefers a trans-trans conformation of the NH protons in the solvent THF at room temperature, but that the trans-cis conformation is more stable below 190K. [30] For urea and thiourea dissolved in dimethysulfoxide or dimethylformamide, NMR studies have suggested that both conformers are present at room temperature and that the rotation around the C-N bond proceeds fast, resulting in a single, time-averaged peak in the NMR spectra. Only at lower temperatures, the NMR signal splits into separate resonances for the trans-cis and the trans-trans conformer due to a slower rotation, [59] indicative of a rotation barrier of ~10 kcal/mol. [59] In line with these findings, IR experiments have shown that diphenylthiourea (0CF-DPTU) in carbon tetrachloride exhibits two disparate N-H stretching bands. The two bands have been ascribed to both conformers with a ratio of approximately 50:50, where the blue-shifted N-H band has been assigned to the trans-trans configuration.[183] Also for thioureas with bulky side groups (e.g. N,N-di-*t*-butylthiourea) the presence of both conformers has been deduced from Fourier-Transform infrared (FT-IR) spectra, while thioureas with less bulky substituents (e.g., N,N-dimethylthiourea and N,N-diethylthiourea) seem to favor the trans-trans conformation. [181]

Besides the conformational degree of freedom, also self-association of thioureas may affect their state in solution. Yet, despite N,N-diethylthiourea is significantly self-association in solution, thioureas with more bulky substituents, like N,N-di-*t*-butylthiourea,[181] or with electron-withdrawing groups[123] appear to be dissolved as rather isolated molecular entities, and the self-association seems to be intimately related to the prevailing conformation. [123] In general, electron-withdrawing CF_3-substituents enhance the formation of reactive intermediates between thioureas and reactants in catalysis, [192] yet the effect of conformational flexibility on the catalytic performance has been poorly understood.

The lack of information on the effect of conformational distributions on catalysis is related to the challenges in determining the conformations at relevant reaction conditions: Powerful techniques, such as NMR spectroscopy or quantum chemical calculations provide insight only at low temperatures (at which conformational dynamics are sufficiently slowed-down) or for isolated molecules (e.g. gas-phase), respectively.[30] In turn, infrared absorption spectroscopy can, in principle, probe conformations on much shorter timescales (i.e. the time scale of molecular vibrations), but it relies on distinct vibrational bands for different conformers. For differently CF_3 substituted diphenylthioureas, the bare diphenylthiourea (0CF-DPTU) indeed displays two disparate N-H stretching bands. [183,192] Yet, in the presence of two CF_3-groups (2CF-DPTU) the two bands overlap and become nearly indistinguishable for DPTU with four CF_3-substituents (4CF-DPTU), [192] which might be explained by different conformational populations or coincidence of the resonance frequencies. [192]

In the presence of hydrogen-bond accepting substrates, the N-H groups of thiourea form hydrogen-bonds, and an additional red-shifted N-H stretching band is evident in the FTIR spectra.[52,60,61] Analysis of the hydrogen-bonded band has, in fact, allowed quantifying the overall binding strengths of the catalysts with the substrates and the obtained overall binding strengths were in line with NMR results. [192] Yet, the presence of various infrared absorption bands makes isolation of the contributions of the individual molecular species (conformations and reactive intermediates) on the basis of the FTIR absorption spectra challenging. The different molecular level conformations, however, make not only the infrared absorption line shapes to differ but also result in different interaction with and coupling to the environment. As such, the different molecular oscillators can have different vibrational dynamics, which allows better discrimination of the contributing molecular species. [108] Thus, resolving different molecular species can be readily achieved using femtosecond infrared spectroscopy (fs-IR). [89,108,193-196]

Here, we study the vibrational dynamics of diphenylthiourea with zero (0CF-DPTU), two (2CF-DPTU), and four CF_3 substituents (4CF-DPTU) in solution, whose catalytic activity has been studied in detail before. [192] As model systems for hydrogen-bond accepting species we use 1,3-diphenyl-2-propenone and acetophenone, since ketones are the relevant substrates, which are applied in Diels-Alder cycloadditions. [23] To disentangle different molecular species contributing at N-H stretching frequencies, we perform fs-IR experiments. We find that for all substituted thioureas two disparate vibrational modes, with distinctively different vibrational relaxation times, give rise to the measured infrared absorption spectra at N-H stretching frequencies, which we ascribe to different conformers. Using the motionally averaged signals of the free and the bound catalyst in the NMR spectra, [59,175,176] we show that with increasing CF_3 substitution more hydrogen-bonded species with the hydrogen-bond accepting ketones are formed. Fs-IR experiments evidence that the vibrational dynamics of the hydrogen-bonded N-H groups are very similar for all studied thiourea-ketone mixtures. Yet, our results indicate that in the presence of the ketone the vibrational response of only one conformer is altered, which suggests the binding of the ketone occurs predominantly for a specific catalyst conformation.

6.3 Experimental Methods

Sample preparation

The preparation and the implementation of the experiments were done analogous to previous experiments[192], which are used as comparison to the here described data. The catalysts diphenylthiourea (0CF-DPTU, Fluka, >98%), N,N′-bis[4-(trifluoromethyl)phenyl]-thiourea (2CF-DPTU, TCI, >97%), N,N′−bis[3,5−bis(trifluoromethyl)phenyl]−thiourea (4CF-DPTU, TCI, >98%) and the

substrate 1,3-diphenyl-2-propenone (Sigma-Aldrich, >98%) were used without further purification. The substrate acetophenone (Merck-Schuchardt, 98%) was dried over 4 Å molecular sieve. For the NMR experiments, the deuterated solvents dichloromethane (DCM-d2, Deutero, 99.6%) and toluene (toluene-d8, Aldrich, 99.6%) were used. All deuterated solvents were dried over a 4 Å molecular sieves and filtered with a 0.2 µm Omnipore membrane filter prior to sample preparation. For the infrared experiments, the non-deuterated solvents dichloromethane (DCM, Fischer Chemical, 99.98%) and toluene (Fischer Chemical, 99.8%) were used without any further purification. The solutions were prepared with an analytical balance by weight, assuming the solution density to be the density of the solvent.

FT-IR experiments

A Bruker Vertex 70 and a Nicolet 850 Magna IR spectrometer were used to record the FT-IR spectra with a spectral resolution of 4 cm^{-1}. The sample was positioned between two CaF_2 windows, separated by a 0.2mm or 0.5mm thick spacer in a "Specac demountable Omni Cell".

NMR experiments

NMR-spectroscopy was used to obtain information about the chemical environment of the catalysts NH-proton. A Bruker 300 MHz AVANCE III spectrometer was used to record the ^{1}H-NMR spectra. As a reference, the residual DCM peak at 5.32ppm and the residual toluene peak at 2.09ppm were used. In case of acetophenone, there was an overlap at ~2.09ppm of acetophenones proton resulting from the CH_3-group with the toluene peak. In this case we referenced to the toluene peak at 6.98ppm. The chemical shift was determined by using the peak picking tool in MestReNova.

Femtosecond IR experiments

A similar sample cell as for the FT-IR experiments is used: the sample is positioned between two CaF_2 windows within a demountable sample cell with variable thickness.
Femtosecond IR pump-probe experiments were based on a Ti:Sa regenerative amplifier to generate 800nm pulses at a repetition rate of 1kHz (Spectra Physics, Spitfire Ace). The femtosecond laser pulses are used to pump an optical parametric amplifiers (TOPAS Prime with non-collinear difference frequency generation, Light Conversion), which generates IR pulses centered at a frequency of 3000 nm, a pulse duration of ~200fs, a pulse energy of 5-8 µJ and a FWHM of ~400cm^{-1}. The pulses are split into a pump pulse (~92%), probe pulse (~4%), and a reference pulse (~4%). The reference pulse is used to correct for pulse-to-pulse fluctuations of the probe beam. The pump beam is guided to a delay stage to control the time delay between pump and probe pulses. Using a λ/2-plate we rotate the polarization of the pump beam to 45° with respect to the probe pulse. The pump beam passes a chopper, which blocks every second pulse, to measure the pump-induced difference of the probe pulse on a shot-to-shot basis. With a parabolic mirror all three beams are focused into the sample and pump and probe beam are

overlapped at this position. The pump beam is blocked after the sample and the probe and the reference beam are recollimated and guided through a rotating wire-grid polarizer, which enables to split the parallel and perpendicular polarization contributions of the probe beam. Probe and reference beams are then guided to a spectrograph, which spectrally disperses them on a nitrogen-cooled MCT array detector (Horiba, 300 Grooves/mm and 150 Grooves/mm). The pump pulse is used to excite the vibration to the first vibrational excited state and induces a transient absorption change $\Delta\alpha$. This absorption change is probed by a second weak infrared probe pulse, which is variable in time and can detect the absorption change as a function of time. The transient absorption change $\Delta\alpha$ of the sample can be calculated with the transmitted intensities:

$$\Delta\alpha = -\ln \frac{\frac{I_{probe}}{I_{reference}}}{\frac{I_{probe,0}}{I_{reference,0}}} \tag{6-1}$$

, where I_{probe} and $I_{reference}$ are the intensities of the probe and the reference beam with pump excitation and $I_{probe,0}$ and $I_{reference,0}$ are the intensities of the probe and the reference beam without pump excitation. The parallel $\Delta\alpha_{par}$ and perpendicular $\Delta\alpha_{perp}$ polarization contributions are needed to construct the isotropic signal $\Delta\alpha_{iso}$:

$$\Delta\alpha_{iso} = \frac{\Delta\alpha_{par} + 2\Delta\alpha_{perp}}{3} \tag{6-2}$$

The isotropic signal is independent of orientational dynamics, but contains information about population dynamics and the vibrational lifetime.

6.4 Results and Discussion

N-H vibrational structure and dynamics of thiourea catalysts in solution

Before studying the influence of substrates on the molecular association of different CF_3 substituted diphenylthiourea catalysts, we first explore the state of the bare catalysts in solution and its associated vibrational dynamics. In *Figure 6-2a* and *b* we show the FT-IR spectra of the catalysts 4CF-DPTU and 0CF-DPTU in the solvent DCM at N-H stretching frequencies. [192] The linear absorption spectrum of 0CF-DPTU shows a clear double-peak

structure with two modes at 3355 cm^{-1} and 3385 cm^{-1}. The presence of two bands has been rationalized to be due to the NH-stretching vibration of two different conformers in solution[192], that are the trans-trans and the trans-cis isomer. [183]

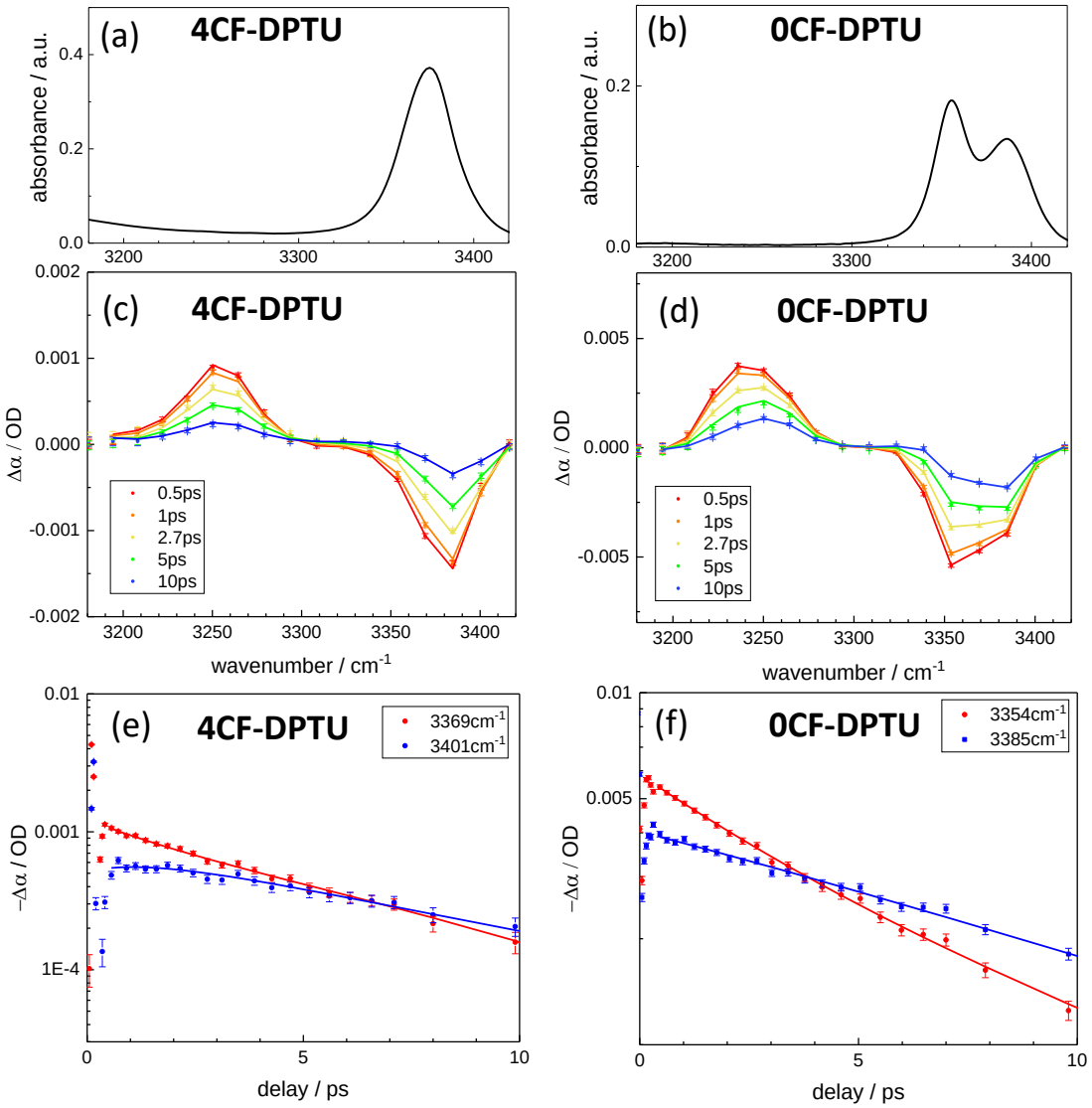

Figure 6-2: Comparison of the NH stretching vibration of pure 4CF-DPTU and 0CF-DPTU in DCM. (a),(b) Shown are the FT-IR spectra, (c),(d) the transient fs-IR spectra, (e),(f) and the time traces of the bleach of the fs-IR data.

Conversely, the linear absorption spectrum of 4CF-DPTU only reveals a single rather symmetric N-H stretching band at ~3375 cm^{-1}. The observation of a single band is in line with the trans-trans configuration prevailing at room temperature as suggested by a combined NMR and DFT study.[30] Yet, for both 0CF-DPTU and 4CF-DPTU both conformers are similar in energy and thus the single band for 4CF-DPTU may also stem from different conformational equilibria and/or faster conformational dynamics[184] and/or from resonance frequencies of the two conformers coinciding, which would be in

line with other studies suggesting that both conformers are present at room-temperature. [16, 18, 19]

To better resolve different contributions to the absorption spectra, we perform ultrafast infrared pump-probe spectroscopy experiments. In this experiment, oscillators are excited with a pump pulse and the time-dependent changes of the absorption spectrum, which were induced by the pump pulse, are detected with a variably delayed probe pulse. The isotropic transient absorption spectra, which are independent of reorientation processes and represent the vibrational dynamics as a function of the wavenumber. [88,106] are shown in *Figure 6-2c* and *d*. In case of 0CF-DPTU, we observe a ground state bleach at the spectral position of the NH vibration at all delay times. This ground state bleaching (GSB) signal can be explained by the depopulation of the ground state, after the arrival of the pump pulse and the stimulated emission from the excited state. Red-shifted to the ground state bleach is a positive peak due to the excited state absorption (ESA). It can be explained by the transition of the oscillator from the first to the second vibrational excited state. The bleaching signal is rather broad (~45cm^{-1}, broader than ~35cm^{-1} for 4CF-DPTU, see below), which can be explained by the spectrally unresolved contributions of both peaks in the linear absorption spectrum. We note that using our experimental setup, the double-peak structure can be resolved at the cost of detecting the excited state absorption (see SI, *Figure 6-10*). Nevertheless, the two bands that have been assigned to the two different conformers of 0CF-DPTU are reflected in the vibrational dynamics. As can be seen in *Figure 6-2f*, the transient signals decay faster at red-shifted frequencies as compared to blue-shifted frequencies for 0CF-DPTU.

For 4CF-DPTU, we also observe a negative, but somewhat narrower peak compared to 0CF-DPTU centered at the spectral position of the NH-vibration in the linear IR spectrum (~3375 cm^{-1}) at all delay times and a red-shifted positive peak due to the excited state absorption (ESA). The red-shift of the ESA relative to the GSB is a measure for the anharmonicity. In both cases we find a ~135cm^{-1} red-shift of the ESA relative to the GSB - the ground state bleach and ESA are well separated - which corresponds to a rather large anharmonicity. Remarkably, also for 4CF-DPTU (*Figure 6-2e*) the blue-wing of the bleach reveals a slower vibrational relaxation as compared to the red-shifted frequencies, indicative of a frequency-dependent vibrational relaxation, which points at different molecular-level oscillators. We note that such frequency-dependent vibrational relaxation can only be detected if spectral diffusion (fluctuation of the instantaneous resonance frequency of the excited oscillators) is slower than the vibrational relaxation.
To quantify the frequency-dependent vibrational relaxation, we model the experimental data. One limiting case exhibiting slow spectral diffusion occurs when two subensembles of molecular oscillators exchange slower than their relaxation to the ground state. [197] Therefore we assume two distinct modes contributing to the transient signals. Based on the reported presence of two conformers, we assign the two subensembles to the two

conformers. Given that, at reduced temperatures, the two conformers interchange sufficiently slowly that they can be resolved on the slow NMR timescale,[30,58] we assume both conformers to not exchange on the timescale of a few picoseconds probed in the fs-IR experiments. In the model, we assume that both subensembles have their own transient spectrum and different vibrational lifetime with which they relax to a common (hot) ground state. In the hot ground state, the vibrational energy is fully dissipated to thermal energy. [88,108] As can be seen in *Figure 6-2c-f*, this model describes the experimental data very well. As such, the N-H stretching vibrational structure and dynamics of both catalysts in solutions can be excellently modeled by assuming two disparate N-H oscillators (for details, see SI). For 4CF-DPTU these modes have a vibrational relaxation time of 6.6ps and 1.4ps, while the relaxation times are roughly two times slower in the case of 0CF-DPTU in solution: 11.4ps and 3.4ps.

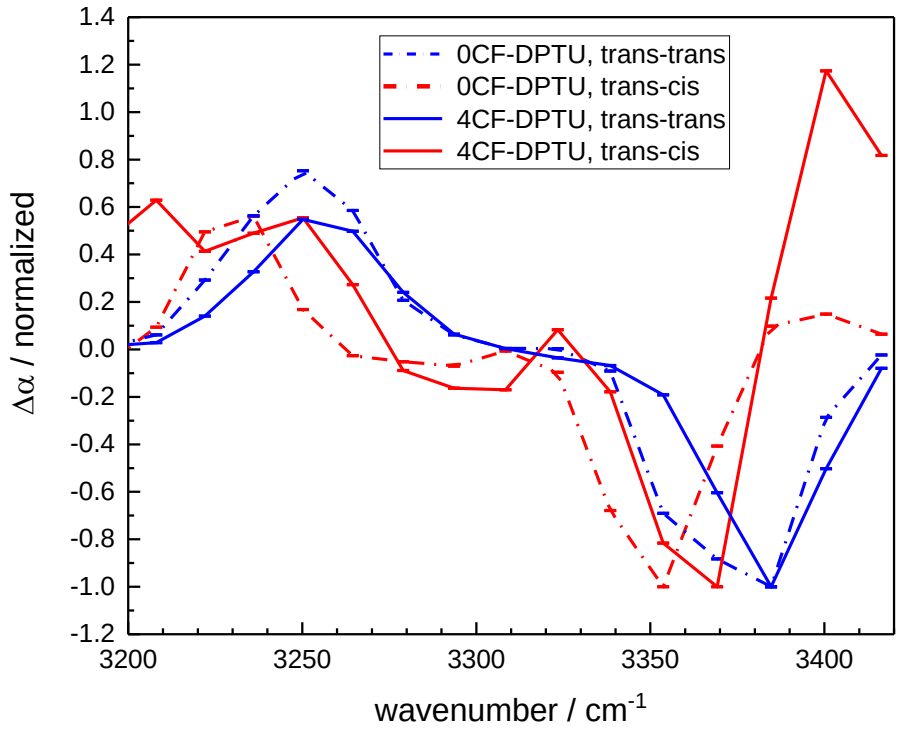

Figure 6-3: Comparison of the associated spectra of pure 4CF-DPTU (solid lines) and pure 0CF-DPTU (dashed-dotted lines) in DCM extracted from a parallel model fit with 2 times constants. The trans-trans conformer (blue) spectrum is centered at higher frequencies and has a longer vibrational relaxation compared to that of the trans-cis conformer (red) and has a shorter vibrational relaxation.

From the fits, we can also extract the associated spectra, corresponding to the different vibrational lifetimes (see SI). In *Figure 6-3* we show the associated spectra for the two components for solutions of 4CF-DPTU and 0CF-DPTU. The longer vibrational lifetime is associated with the blue-shifted spectrum (blue), which we assign to the trans-trans conformer, and the shorter vibrational lifetime corresponds to the red-shifted spectrum (red), which we assign to the trans-cis conformer according to previous assignments in

literature. [181,183,198,199] All four extracted associated spectra reveal a bleach and a red-shifted ESA (*Figure 6-3*). Our experiments of the thiourea catalysts in solution thus show the presence of the distinctively different N-H stretching modes in solution.

N-H hydrogen-bonding in the presence of ketones

Thiourea-ketone association from NMR chemical shifts

In catalysis, thiourea catalysts are shown to hydrogen-bond to ketones to form reactive hydrogen-bonded complexes. To investigate such complexes, we study the interaction of 0CF-DPTU, 2CF-DPTU and 4CF-DPTU in solution with acetophenone and diphenylpropenone[192] as representative substrates.

In a first step, we determine the overall interaction of the different thiourea catalysts with the ketones using ^{1}H-NMR-spectroscopy and compare it to our previous results on the association with diphenylpropenone[192] (*Figure 6-4*). The details of these experiments are described in ref [192]. Briefly, we detect the chemical shift of thiourea's NH proton at ~7.75-7.9ppm at a constant thiourea concentration (c^0_{cat} = 0.01 mol/L) as a function of substrate (c^0_{subs} = 0 – 0.4 mol/L) concentration[30]. Upon addition of substrate, the NH proton experiences a marked downfield shift due to de-shielding of the NH proton upon hydrogen bonding to the ketones. These experimentally observed chemical shifts can be modeled by assuming the N-H chemical shift to be the motionally averaged signal of free (δ_{cat}, see *Table 6-1*) and hydrogen-bonded $\delta_{complex}$ thioureas, with the relative amount of hydrogen-bonded catalysts determined by the thermodynamic association equilibrium. From this model the chemical shift of the hydrogen-bonded complex, $\delta_{complex}$, and the association constant, K_{NMR}, can be obtained (see fits in *Figure 6-4*). The thus obtain association parameters are summarized in *Table 6-1*.

The NMR results confirm our earlier findings[192] for diphenylpropenone also for acetophenone: the association constants K_{NMR} in the solvent DCM increase with increasing CF_3 substitution: K_{NMR}(4CF-DPTU) > K_{NMR}(2CF-DPTU) > K_{NMR}(0CF-DPTU). Despite the association constants K_{NMR}(4CF-DPTU) and K_{NMR}(2CF-DPTU) are somewhat higher for diphenylpropenone as compared to acetophenone, taking the experimental uncertainty into account [178], the association strengths are very similar. We note that the same trend is observed in toluene as a solvent, except for the combination 4CF-DPTU with diphenylpropenone (see SI, *Table 6-2* and *Figure 6-12*).

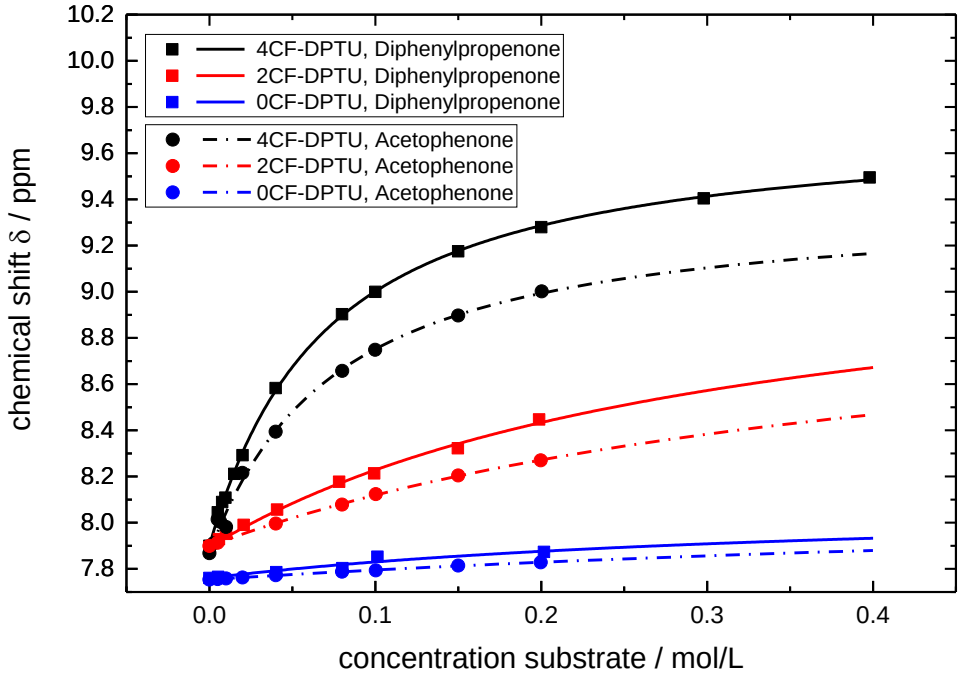

Figure 6-4: Chemical shift of the NH protons as a function of substrate concentration $\boldsymbol{c^0_{subs}}$ *for 4CF-DPTU (black), 2CF-DPTU (red), and 0CF-DPTU (blue) in DCM with the substrate acetophenone (round symbols, dashed lines) and diphenylpropenone (rectangular symbols, solid lines). The catalyst concentration is kept constant at* $\boldsymbol{c^0_{cat}}$ *= 0.01 mol/L (for 0CF-DPTU:diphenylpropenone:* $\boldsymbol{c^0_{cat}}$ *= 0.015 mol/L, see[192]). The data of the substrate diphenylpropenone is taken from[192]. Solid and dashed lines show fits with the association model analogously to ref [192].*

In addition to the association constants, the value of the chemical shift of the complex $\delta_{complex}$ provides insight into hydrogen-bonding within the formed complexes: In general, stronger de-shielding of hydrogen-bonding protons is indicative of stronger hydrogen-bonds. [200] For increasing CF_3 substitution from 0CF-DPTU to 4CF-DPTU we find higher values of $\delta_{complex}$, indicative of stronger intermolecular interaction. Interestingly, the chemical shift of the complex $\delta_{complex}$ is lower for all studied thioureas when substituting the substrate diphenylpropenone with acetophenone. These differences are also somewhat reflected in the trend of the K_{NMR} values. The difference between the two substrates could originate from weaker hydrogen-bonding of the N-H groups to acetophenone as compared to diphenylpropenone or, alternatively, result from enhanced shielding of the N-H proton due to the conjugated pi-electrons of diphenylpropenone as compared to acetophenone.

Table 6-1: Association constants, $K_{NMR,}$ and the chemical shift of the complex $\delta_{complex}$ in DCM for the substrates acetophenone, and diphenylpropenone (taken from reference[192]), as obtained from the fits of the ^{1}H-NMR chemical shifts for the catalysts 0CF-DPTU, 2CF-DPTU and 4CF-DPTU, respectively. The shift of the free catalyst δ_{cat}, was fixed to the value found for solutions of only the catalyst.

K_{NMR}	4CF-DPTU	2CF-DPTU	0CF-DPTU
Diphenylpropenone	15.8 $\pm$ 0.7 L/mol	3.27 $\pm$ 0.3 L/mol	0.86 $\pm$ 0.03 L/mol
Acetophenone	14.6 $\pm$ 1.8 L/mol	2.3 $\pm$ 0.05 L/mol	1.2 $\pm$ 0.05 L/mol
$\delta_{complex}$	**4CF-DPTU**	**2CF-DPTU**	**0CF-DPTU**
Diphenylpropenone	9.74 $\pm$ 0.02 ppm	9.27 $\pm$ 0.06 ppm	8.54 $\pm$ 0.02 ppm
Acetophenone	9.39 $\pm$ 0.07 ppm	9.10 $\pm$ 0.01 ppm	8.15 $\pm$ 0.01 ppm
δ_{cat}	**4CF-DPTU**	**2CF-DPTU**	**0CF-DPTU**
Diphenylpropenone	7.90 ppm	7.89 ppm	7.77 ppm
Acetophenone	7.87 ppm	7.90 ppm	7.75 ppm

Linear infrared spectra of catalyst-substrate mixtures

To explore potential differences of the hydrogen-bonded structure and dynamics within the complexes, we perform linear infrared (FT-IR) spectroscopy. Given that the largest fraction of catalysts is bound in complexes for an excess of ketone, we focus here on the catalyst:substrate mixture 1:20. To explore (i) the effect of substrate on hydrogen bonding, we choose the catalyst 4CF-DPTU and compare the substrates diphenylpropenone and acetophenone upon binding. To explore (ii) the effect of the catalyst, we compare 0CF-DPTU and 4CF-DPTU upon binding to the substrate diphenylpropenone.

In *Figure 6-5a*, we show the absorption spectra for solutions of 4CF-DPTU and a mixture of 4CF-DPTU:diphenylpropenone=1:20 in DCM, which are taken from reference[192], and compare it to a mixture of 4CF-DPTU:acetophenone=1:20. To isolate contributions of the thiourea catalyst at N-H stretching frequencies (~3150-3500cm^{-1}), contributions of the solvent and the substrate have been subtracted. Upon addition of both ketone substrates, the detected band becomes asymmetric and markedly red-shifts for both substrates. For both catalyst-substrate mixtures, the absorption band broadens

(spanning a frequency range of ~3150cm^{-1} – 3400cm^{-1}) relative to the pure 4CF-DPTU (FWHM ~30cm^{-1}) with almost identical line shapes. However, the red-shift is around 15 cm^{-1} larger for the mixture of 4CF-DPTU:diphenylpropenone (1:20) compared to 4CF-DPTU:acetophenone (1:20). This may suggest a different electronic structure or a different binding motif for the different substrates, yet we caution the reader that this red-shift is somewhat sensitive to the subtraction of the solvent absorption.

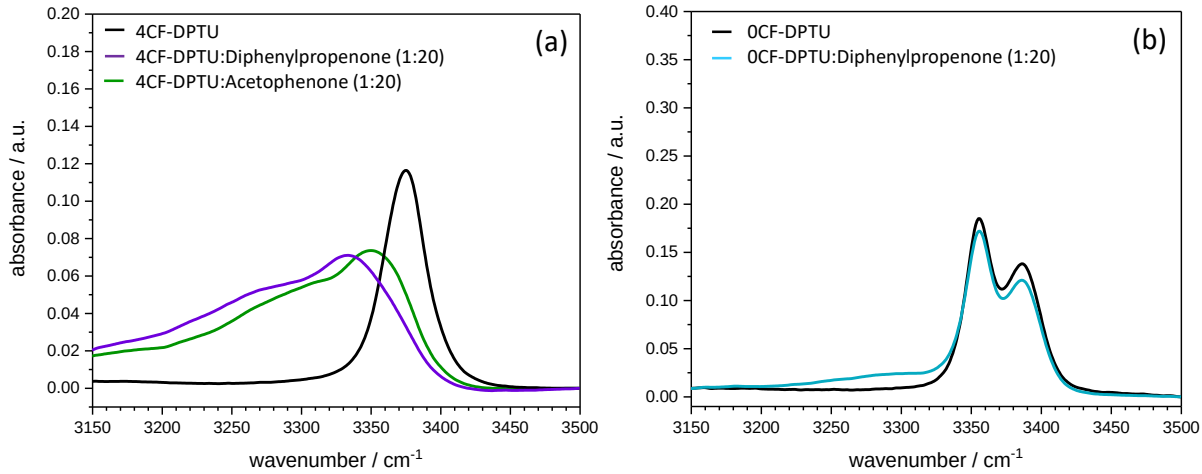

Figure 6-5: (a) Infrared absorption spectra for solutions of 4CF-DPTU in DCM ($\boldsymbol{c^0_{cat}}$ = 0.02 mol/L, black line) and with the substrate acetophenone ($\boldsymbol{c^0_{subs}}$ = 0.4 mol/L, green line) and the substrate diphenylpropenone ($\boldsymbol{c^0_{subs}}$ = 0.4 mol/L, purple line) as reported in ref. [192]. (b) Infrared absorption spectra for solutions of 0CF-DPTU in DCM ($\boldsymbol{c^0_{cat}}$ = 0.02 mol/L, black line) and with the substrate diphenylpropenone ($\boldsymbol{c^0_{subs}}$ = 0.4 mol/L, purple line) as reported in[192]. The absorbance of the solvent and the absorbance of the substrate were subtracted from all spectra and additionally corrected for a constant offset due to reflection losses (for details, see reference[192]).

Comparison of the 0CF-DPTU in DCM to 0CF-DPTU:diphenylpropenone (1:20) mixtures in DCM (*Figure 6-5b*) reveals only a minor reduction of the amplitude of the free NH stretching vibrations, relative to solutions without ketone - in line with the weaker association constants determined from the NMR chemical shift (*Table 6-1*). In the presence of the substrate a weak absorption at 3200cm^{-1} – 3340cm^{-1} emerges. This red-shifted absorbance can again be attributed to the hydrogen-bonded NH stretching vibration within hydrogen-bonded complexes, which is less intense due to the weaker association strength. Thus, the FTIR spectra point at slightly different bonding strengths depending on the substrate and shifted conformational equilibria in the presence of the ketones. Yet, the exact lineshapes in the FT-IR spectra are prone to the correction of the background (solvent and ketone), which might bias spectral shapes. To better discriminate the different N-H oscillators that give rise to the absorption bands, we again use ultrafast vibrational pump-probe IR spectroscopy.

Fs-IR spectroscopy for catalyst-substrate mixtures

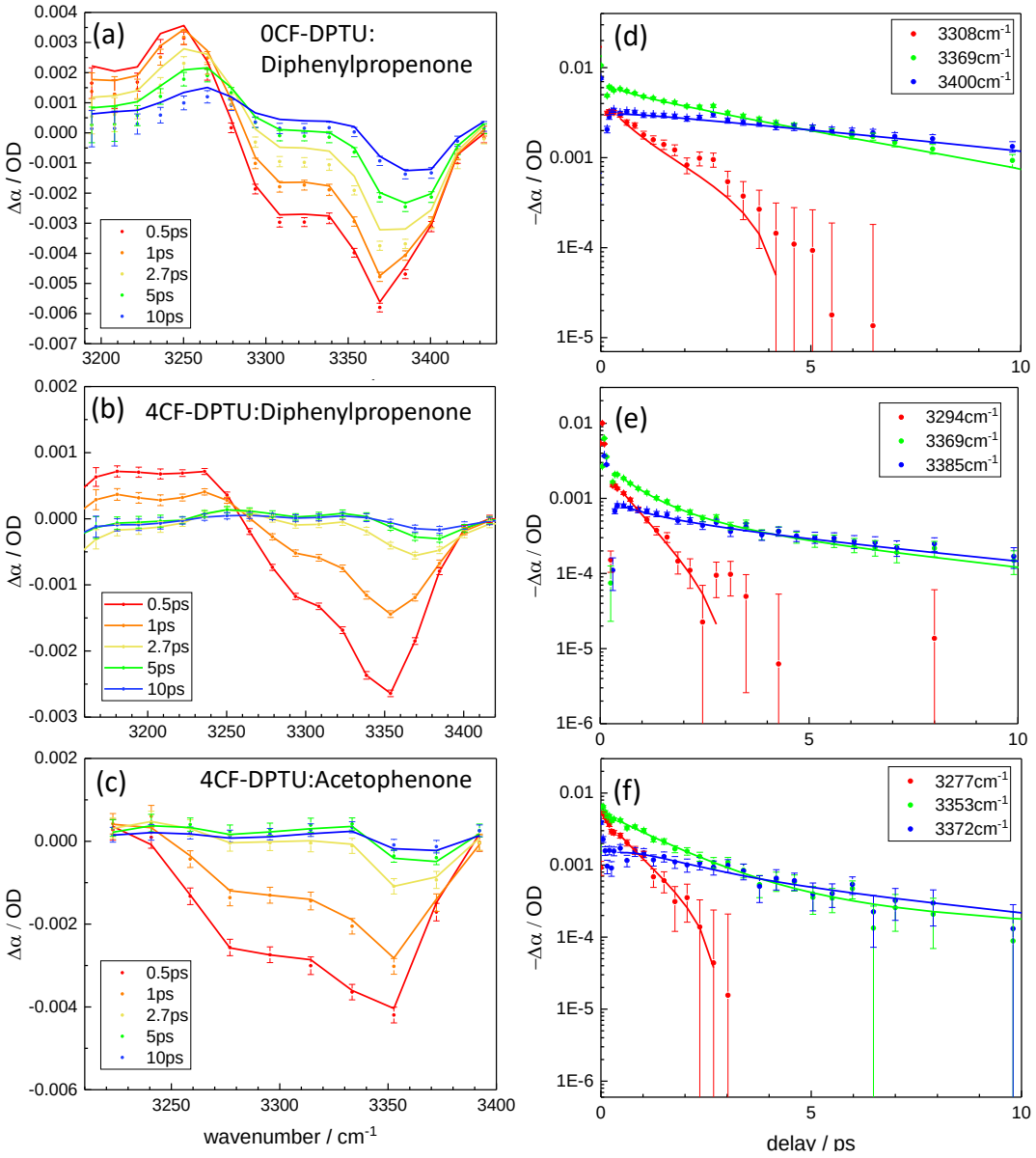

Figure 6-6: Fs-IR spectra of 4CF-DPTU:acetophenone=1:20 (a), 4CF-DPTU:diphenylpropenone=1:20 (b) and 0CF-DPTU:diphenylpropenone=1:20 (c). Time traces for three different wavenumbers for 4CF-DPTU:acetophenone=1:20 (d), 4CF-DPTU:diphenylpropenone=1:20 (e) and 0CF-DPTU:diphenylpropenone=1:20 (f). Symbols show experimental data. The lines show fits of a parallel model fit to the experimental data with 3 relaxation times (for details see text).

In *Figure 6-6* we show the transient pump-probe IR spectra as a function of wavenumber at different delay times for 4CF-DPTU with two different substrates, 4CF-DPTU:acetophenone=1:20 (*Figure 6-6c*) and 4CF-DPTU:diphenylpropenone=1:20 (*Figure 6-6b*). In both cases, we observe a rather broad bleaching signal at ~3250-3400cm^{-1}, due to the ground state bleach of the different NH modes. Due to the

simultaneous presence of free catalysts (with 2 conformations) and hydrogen-bonded complexes with the ketone the bleaching signal is much broader than for solutions of only the catalysts, in line with the FTIR spectra (*Figure 6-5*). However, the maximum amplitude of the bleaches is slightly blue-shifted compared to the FT-IR spectra, which can be explained by the ESA of the free catalyst that is still present in solution and partly overlaps with the bleach of the H-bonded complexes prevailing in solution. Based on our NMR results, we estimate the relative populations of the hydrogen-bonded species to >70 % while < 30% of catalysts are present as free (solvated) molecules (see SI, *Figure 6-13*). For 4CF-DPTU:diphenylpropenone=1:20, we also observe a red-shifted positive signal due to the ESA. The amplitude of the transient signal is less pronounced than in case of the free catalyst 4CF-DPTU (compare to *Figure 6-2*), because the bleach and ESA partly overlap due to the markedly broadened NH absorption band and partially cancel out. 4CF-DPTU:acetophenone does not reveal a significant amount of ESA, which might be due to a stronger extent of the overlap with the bleaching signal.

Similarly, also for 0CF-DPTU:diphenylpropenone (*Figure 6-6a*) the transient spectrum exhibits a rather broad bleaching signal from ~3280-3420cm^{-1}. The FWHM of the bleaching signal is similar to 4CF-DPTU:acetophenone=1:20 and 4CF-DPTU:diphenylpropenone=1:20, indicative of hydrogen-bonded complexes also contributing to the spectra in *Figure 6-6a*. However, the bleaching signal is present at higher wavenumbers, because 0CF-DPTU:diphenylpropenone=1:20 exhibits a broader free NH band with a higher concentration of free catalyst (~80%) being present (see SI, *Figure 6-14*). The red-shifted ESA for 0CF-DPTU:diphenylpropenone=1:20 is more intense as for 4CF-DPTU:acetophenone=1:20 and 4CF-DPTU:diphenylpropenone=1:20, which can also be explained by the higher fraction of free catalysts (and the more intense ESA of free catalysts).

For all mixtures, the red-shifted bleaching signals decay faster with time than blue-shifted bleaching signals: at a delay time of ~4 ps the signals at ~3300 cm^{-1} have nearly fully vanished. At 3360 cm^{-1}, where the GSB of the free catalysts is observed (*Figure 6-2*), a somewhat narrow bleaching signal is still detectable. Overall this results in a blue-shift of the bleach with increasing delay time. Hence, already from the time-dependent spectra, largely different vibrational relaxation times are apparent, which is a prerequisite for a better decomposition of the individual N-H modes. The frequency-dependent relaxation is even more apparent from the transient signals shown at three different wavenumbers as a function of the delay time in *Figure 6-6d-f*. Similar to the pure catalysts (*Figure 6-2*), we observe at higher frequencies two distinctively different decay times (green and blues symbols in *Figure 6-6d-f*) for all catalyst-substrate mixtures. Additionally, at red-shifted frequencies, we observe in all cases that the transient signals (red symbols in *Figure 6-6d-f*) decay much faster (at least 3x faster than for the pure catalyst). Thus, as commonly observed for hydrogen-bonded systems, [88] the

excited states of the N-H stretching modes for the hydrogen-bonded complexes relax much faster to the ground state as compared to the free catalyst.

To better resolve the contributions of different molecular species to the transient signals, we model data using three different excited-state molecular species, which each relax with a given – frequency-independent – relaxation time to a common heated ground state (see *Figure 6-7*). Two of the three molecular species correspond to the two species (conformers) that are already present for solutions of only the catalysts. The third species is used to model the contributions of the hydrogen-bonded complexes with the substrate. Note that here we consider vibrational dynamics of all three species to be independent of each other, which appears reasonable as (i) conformational dynamics are slow (see above), and (ii) the large spatial separation of the individual thiourea molecules due to the low concentration, which hampers coupling and energy transfer between different thiourea molecules in solution. Yet, chemical exchange due to the breaking and formation of hydrogen-bonded complexes, which may occur within our experimental time window, is neglected (see discussion below). To reduce parameter space when modeling the data, we assume the vibrational relaxation times of the two species assigned to the free catalyst to be the same as in the absence of the substrate (6.6ps and 1.4ps for 4CF-DPTU and 11.4ps and 3.4ps for 0CF-DPTU). Using this model, we thus obtain the vibrational relaxation time and the associated spectra of the hydrogen-bonded complexes from the data in *Figure 6-6* (for details of the model, see SI). We find that the vibrational relaxation time of the hydrogen-bonded complexes are very similar – irrespective of the catalyst or the substrate: 4CF-DPTU:acetophenone=1:20 (0.52ps), 4CF-DPTU:diphenylpropenone=1:20 (0.65ps) and 0CF-DPTU:diphenylpropenone=1:20 (0.58ps), yet significantly faster than that of the free catalyst contributions.

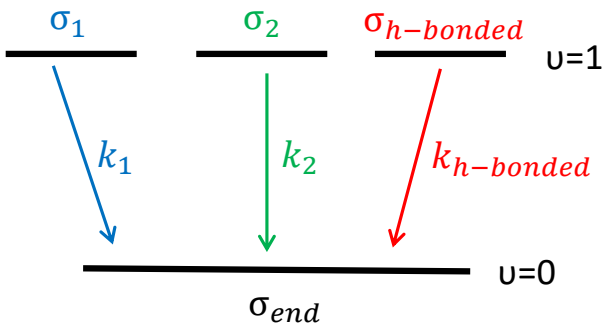

Figure 6-7: Schematic representation of the parallel kinetic model fit. The excitations of the trans-trans conformer (1), the trans-cis conformer (2) and the H-bonded species decay with characteristic rate constants k_j to the final end state (for details see SI). Each state has its corresponding spectral signature σ_j.

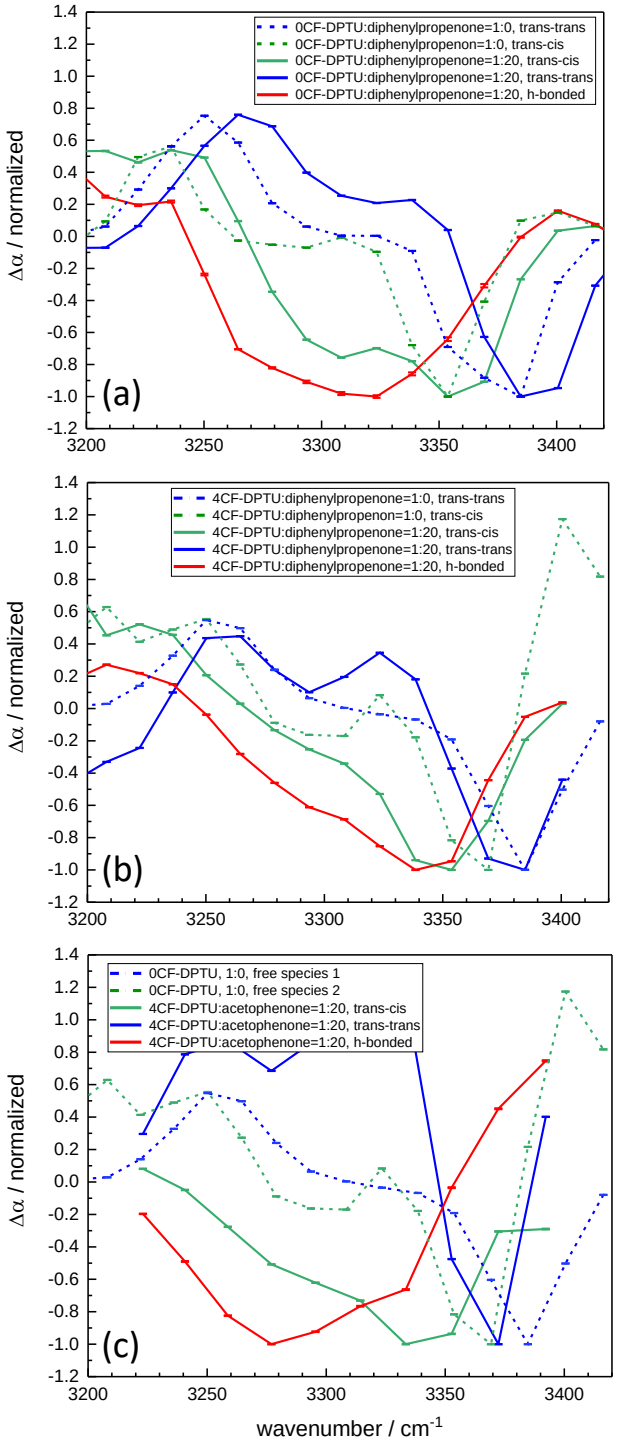

Figure 6-8: Normalized associated spectra for (a) 0CF-DPTU (dashed lines) and 0CF-DPTU:diphenylpropenone=1:20 (solid lines), (b) 4CF-DPTU (dashed lines) and 4CF-DPTU:acetophenone=1:20 (solid lines) and (c) 4CF-DPTU (dashed lines) and 4CF-DPTU: diphenylpropenone=1:20 (solid lines). Note that the associated spectra of the mixtures with the substrate (catalyst:substrate=1:20, solid lines) were extracted from a parallel model fit with 3 time constants. The associated spectra belong to the free species of the trans-trans conformer, the free species of the trans-cis conformer, and the hydrogen-bonded catalyst-substrate complexes.

In general, we find for all samples that the associated spectra of the trans-trans conformer of the free catalysts to be broadly consistent with those obtained from solutions of only the catalysts (cf blue dashed in *Figure 6-8*). Conversely, the associated spectra of the trans-cis conformer deviate from the associated spectrum of the trans-cis conformer for the pure catalyst (dashed green lines in *Figure 6-8*). One notable observation from this comparison is the variation of the associated spectra of the trans-cis conformer: For all three catalyst-substrate mixtures, the associated spectra of the trans-cis conformer are much broader in the presence of the ketone, as compared to the solutions of only the catalyst. In the presence of the substrate, these spectra extend to much lower frequencies, in contrast to the rather narrow line shape in the absence of the ketone. In fact, the asymmetric broadening towards lower frequencies appears like in the presence of ketone, as the spectra of the trans-cis conformer also contain spectral amplitude from the hydrogen-bonded species. Such spectral contributions of complexes to the spectral signatures of the trans-cis conformer may have two distinct origins: (i) Chemical exchange: If a long-lived vibrational excitation of a free N-H oscillator forms a hydrogen-bond to a H-bonding acceptor, its vibrational frequency will red-shift. Yet, the persistence of these signals in the transient signals is determined by the much longer vibrational lifetime of the free catalyst and will persist much longer than the quickly decaying contributions of the excited H-bonded complexes. As such, the variation of the spectra associated with the trans-cis conformer is indicative of chemical exchange between H-bonded N-H modes and the peaks due to the trans-cis conformer. We note that it is unlikely that this exchange is due to the formation of a catalyst-substrate complex from entirely free (solvated) molecules, as diffusion of the involved large molecular entities is too slow to occur to a significant extent. Yet, hydrogen-bond switching between a free and a bonded N-H group of a single catalyst may occur on this timescale. (ii) Alternatively, vibrational energy transfer or coupling between a free N-H group and an H-bonded N-H group with one thiourea molecule may explain the observed 'spectral' mixing. Irrespective of the exact mechanism of the spectral mixing, our observations suggest that only the trans-cis conformer exhibits exchange and/or energy transfer, while the free trans-trans conformer is rather unaffected by the substrate. This could mean that the trans-trans conformer does not form hydrogen bonds to the substrate, or – more likely – the hydrogen-bonded complexes of the trans-trans conformer to the ketone are longer-lived and do not exchange on the timescale of our experiment to a significant extent.

Effect of complex formation on acetophenone's C=O bond

We record the linear IR absorption spectra in the range of ~1640-1720cm^{-1}, characteristic of the C=O stretching vibration (*Figure 6-9*). In the absence of the catalyst, we find an absorption at ~1680cm^{-1}, due to the free C=O stretching vibration. The addition of the catalyst 4CF-DPTU, leads to a side-band at lower wavenumbers, centered

at 1660cm^{-1}. Increasing the amount of catalyst causes an increase of this side-band. Hence, we assign this band to the hydrogen-bonded C=O stretching vibration of acetophenone, as the band strength of the free C=O is weakened (red-shifted) upon the binding of the catalyst, similar to what we observe in the linear IR spectra for the NH group of the catalysts. In order to separate the different contributions, we collected ultrafast vibrational pump-probe IR spectra of the pure acetophenone and a mixture with the catalyst at a 1:1 ratio of 4CF-DPTU:substrate (see SI, *Figure 6-14*). We find that even two time constants are not sufficient to accurately describe the experimental data and conclude that it is challenging to extract the different species from fs-IR spectroscopy, as the vibrational dynamics of the substrate seem to be more complex. Yet, it might be possible to resolve the different contributions with 2D-IR spectroscopy, which is part of future studies.

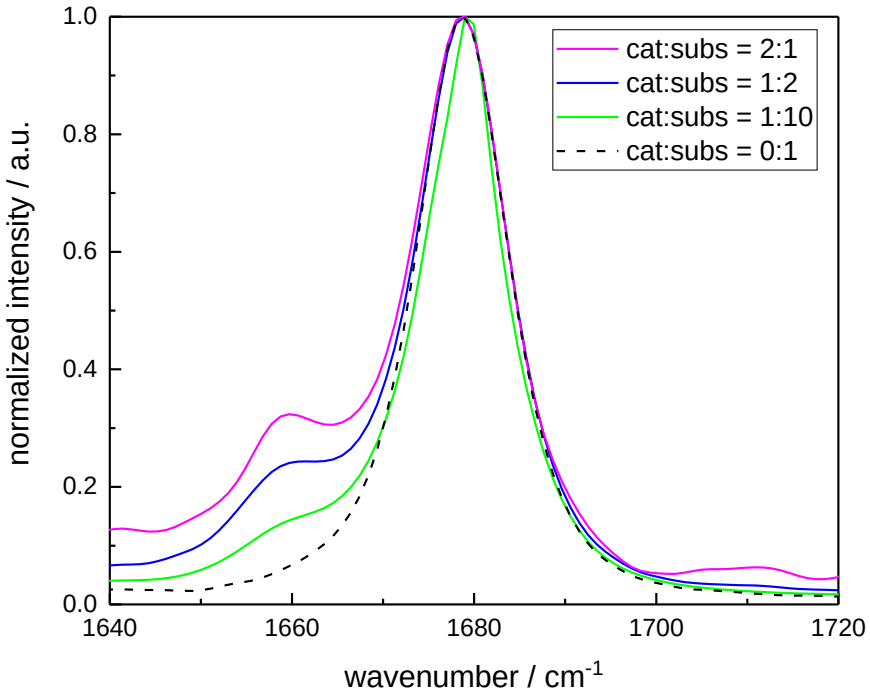

Figure 6-9: FT-IR of pure acetophenone of the CO stretching vibration (dashed black line) with increasing ratio of catalyst (colored lines). The spectra are normalized to the maximum absorbance of the free C=O stretching vibration.

6.5 CONCLUSIONS

We use ^{1}H-NMR, FT-IR and ultrafast vibrational pump probe IR spectroscopy to detect and compare the molecular association of diphenylthiourea-based catalysts with the substrates diphenylpropenone and acetophenone in the solvent DCM in order to investigate the effect of the substrates and the different conformational states of the thiourea catalysts. By examining the N-H stretching modes of the catalysts 4CF-DPTU and 0CF-DPTU with fs-IR spectroscopy, we find two different vibrational dynamics indicative of the presence of two different conformers. Our data suggest the simultaneous presence of the trans-trans and the trans-cis conformers with relaxation times of 6-12ps and 1.5-3.5ps, respectively, for all samples. The trans-trans conformer is concluded to exhibit blue-shifted spectral features compared to the trans-cis conformer.

In the presence of model substrates, we determine the association strength with ^{1}H-NMR spectroscopy. The data reveal a reduced chemical shift of the complex $\delta_{complex}$ for acetophenone compared to diphenylpropenone, indicative of a somewhat stronger intermolecular interaction with diphenylpropenone. The molecular association can also be observed in the FT-IR spectra of the NH-stretching vibration of the catalyst as well as in the FT-IR spectra of the C=O stretching vibration of the substrate: Hydrogen-bonding gives rise to red-shifted absorption bands next to the free N-H stretch and free C=O stretch band. Fs-IR spectroscopy of different catalyst substrate mixtures reveal significantly broadened transient spectra. The hydrogen-bonded N-H groups have shorter vibrational relaxation (~0.6ps), irrespective of the nature of the catalyst or substrate. Based on the different vibrational relaxation times, we can discriminate contributions of the two conformers and the hydrogen-bonded complexes also in solution. Remarkably, the extracted associated spectra reveal “spectral mixing” of the spectra of the trans-cis conformer and of the hydrogen-bonded complexes. This observation can be explained by hydrogen-bond formation with the substrate for only the trans-cis conformer on the ~10ps timescale of the experiment, while the trans-trans conformer seems not to display significant exchange. As such, our results provide evidence that the conformation of the catalyst critically affects the binding dynamics to the catalytic substrates.

6.6 SUPPORTING INFORMATION

Fs-IR spectrum of 0CF-DPTU:diphenylpropenone=1:1 with a higher resolution

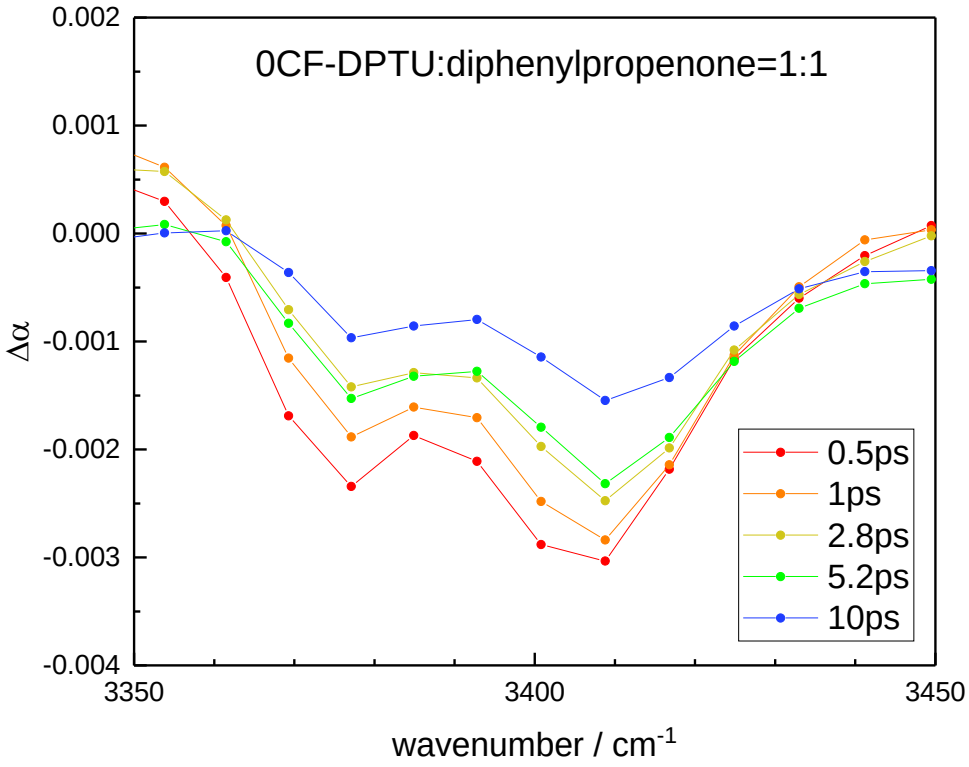

Figure 6-10: Transient fs-IR spectrum of the bleaching signal of the NH stretching vibration of 0CF-DPTU with 1,3-diphenylpropenone in DCM for different delay times. The double peak structure observed in the linear IR spectra, corresponding to conformer 1 and conformer 2, respectively, can also be resolved with ultrafast pump probe IR spectroscopy using a higher spectral resolution for the probe pulse detection.

Parallel Model fit

To fit the transient absorption changes $\Delta\alpha_{iso,}$ we use a model fit that is represented schematically in *Figure 6-11*. To account for the two different conformers of the pure DPTU catalysts, we use two excited states, of conformer 1 and conformer 2, which decay to a common final ground state. The further formation of hydrogen-bonded catalyst-substrate complexes for the mixtures of catalyst with substrate (DPTU:substrate=1:20) is modeled by introducing a third excited state, which decays to the same final ground state. For j=2 or 3 excited states, each excited state is assumed to be equally populated at t=0 ($N_{1..j}(t=0) = 1/j$). The temporal evolution of these population is assumed to follow first order kinetics ($dN_i(t)/dt = -k_i\ N_i(t)$). The measured isotropic spectra are then

assumed to be the linear combination of the time dependent population of the four states multiplied by their corresponding spectra $\sigma_i(\omega)$:

$$\Delta\alpha_{\mathrm{iso}}(\omega,t) = \sum_{i=1}^{4} N_i(t)\sigma_i(\omega) \tag{6-3}$$

By fitting the isotropic data $\Delta\alpha_{iso}$ over the measured frequency range and delay time range, we obtain the rate constants k_i and the spectra, which are associated to each state. This model is based on the assumption that the rate constants k_i and therefore the vibrational lifetimes ($\tau = \frac{1}{k_i}$) are constant over the investigated frequency range. A more detailed explanation of the fitting procedure can be found elsewhere[64,88,108].

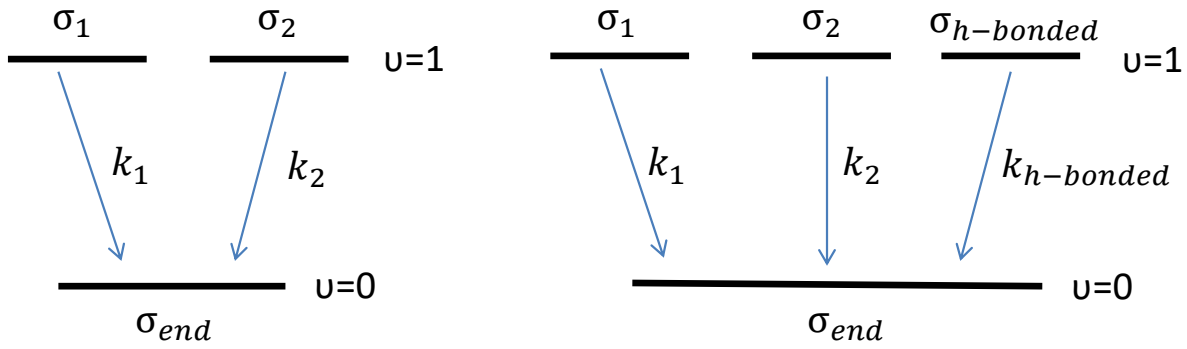

Figure 6-11: Schematic graphical representation of the kinetic model, which is used to describe the experimental isotropic data $\Delta\alpha_{iso}$ of the vibrational relaxation dynamics of the NH vibrations of DPTU based catalysts in DCM. (a) The excitation of conformer 1 and conformer 2 (with the corresponding spectra $\boldsymbol{\sigma_1}$ and $\boldsymbol{\sigma_2}$), in case of the pure DPTU catalysts, decay to the final end state (with the corresponding spectrum $\boldsymbol{\sigma_{end}}$) with characteristic rate constants $\boldsymbol{k_1}$ and $\boldsymbol{k_2}$. (b) For the catalyst-substrate mixtures (DPTU:substrate=1:20), the rate constants $\boldsymbol{k_1}$ and $\boldsymbol{k_2}$ are fixed to the rate constants of the pure DPTU catalyst and a third excited state is introduced, the hydrogen-bonded NH (with the corresponding spectrum $\boldsymbol{\sigma_{h-bonded}}$), which also decays with a characteristic rate constant $\boldsymbol{k_{h-bonded}}$ to the final end state. The associated transient spectral signatures are shown in the main manuscript.

Association equilibria in toluene

Similar to the solvent DCM, we performed an association model fit in toluene for the catalysts 4CF-DPTU, 2CF-DPTU and 0CF-DPTU with the substrates diphenylpropenone and acetophenone (*Figure 6-12*) and find a similar trend: the change of the chemical shift is largest for 4CF-DPTU and decreases with decreasing amount of CF_3-groups. Additionally, the substrate acetophenone reveals a smaller change of the chemical shift than the substrate diphenylpropenone for all studied DPTU based catalysts.

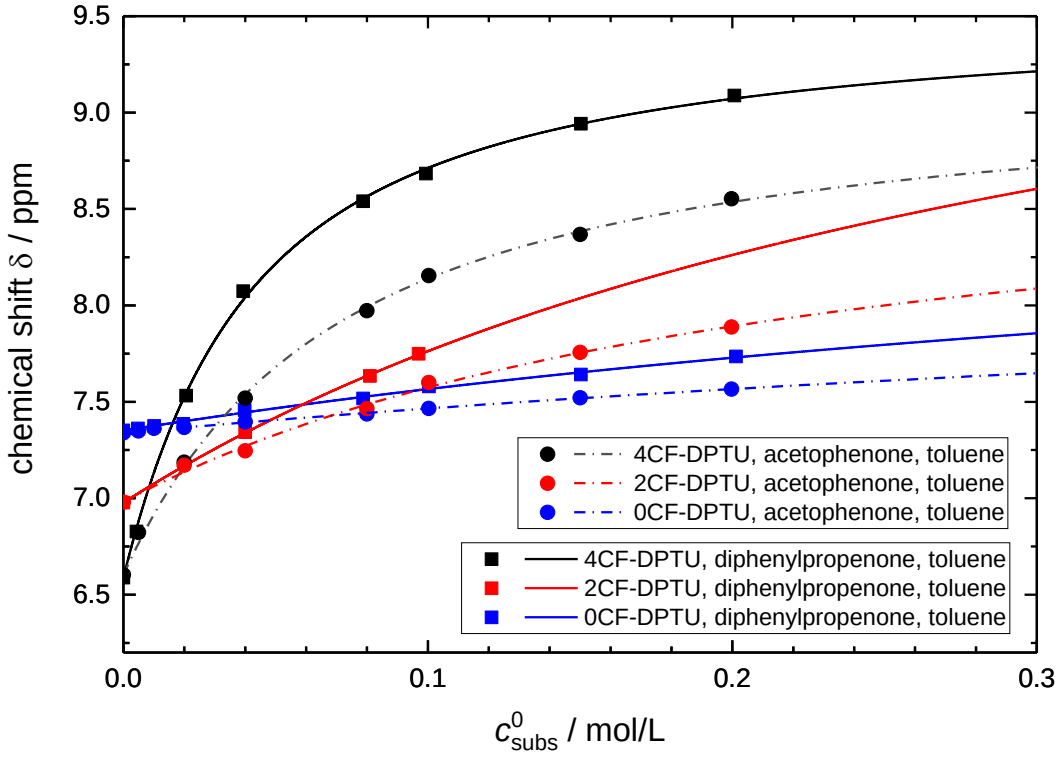

Figure 6-12: Chemical shift of the NH proton as a function of substrate concentration, $\boldsymbol{c^0_{subs}}$ *for 4CF-DPTU (black), 2CF-DPTU (red), and 0CF-DPTU (blue) at a constant catalyst concentration (*$\boldsymbol{c^0_{cat}}$ *= 0.01 mol/L) with the substrates diphenylpropenone (solid lines, squared symbols) and acetophenone (dashed dotted lines, circles) in the solvent toluene. Lines show fits with the association model (see main manuscript and reference[192]).*

Table 6-2: Association constants and chemical shift in toluene

K_{NMR}	4CF-DPTU	2CF-DPTU	0CF-DPTU
Diphenylpropenone	27.7 ± 1.3 L/mol	3.0 ± 0.1 L/mol	1.65 ± 0.2 L/mol
Acetophenone	15.8 ± 0.9 L/mol	4.6 ± 0.3 L/mol	1.3 ± 0.06 L/mol
$\delta_{complex}$	**4CF-DPTU**	**2CF-DPTU**	**0CF-DPTU**
Diphenylpropenone	9.54 ± 0.04 ppm	10.46 ± 0.03 ppm	8.89 ± 0.07 ppm
Acetophenone	9.17 ± 0.05 ppm	8.91 ± 0.07 ppm	8.45 ± 0.04 ppm

Table 6-2 summarizes the obtained association constants K_{NMR} and the chemical shift of the complex $\delta_{complex}$ extracted from the fit. The association constants in toluene obtained for bimolecular association of DPTU based catalysts with the substrates diphenylpropenone and acetophenone reveal also the largest association constant for 4CF-DPTU, which decreases with decreasing amount of CF_3-substitutents at the

catalyst's phenylring, independent of the substrate. Yet, the catalysts 2CF-DPTU and 0CF-DPTU show similar association constants for the two substrates, while 4CF-DPTU reveals a significantly larger association constant upon binding to the substrate diphenylpropenone, compared to acetophenone, suggesting a larger concentration of formed catalyst-substrate complexes. Comparison of the chemical shift of the complex yields for DPTU catalysts a smaller value for acetophenone compared to diphenylpropenone, indicative of a larger binding strength for the substrate diphenylpropenone. Additionally, the chemical shift of the complex decreases with decreasing number of CF_3-groups, except for 2CF-DPTU:diphenylpropenone. This difference can be explained by an higher uncertainty in these experiments, as the chemical shift of the free catalyst 2CF-DPTU coincides with a toluene solvent peak at 6.98ppm, which makes the determination of this signal less robust. [192]

Percentages of bound catalyst and bound substrate in DCM as extracted from NMR

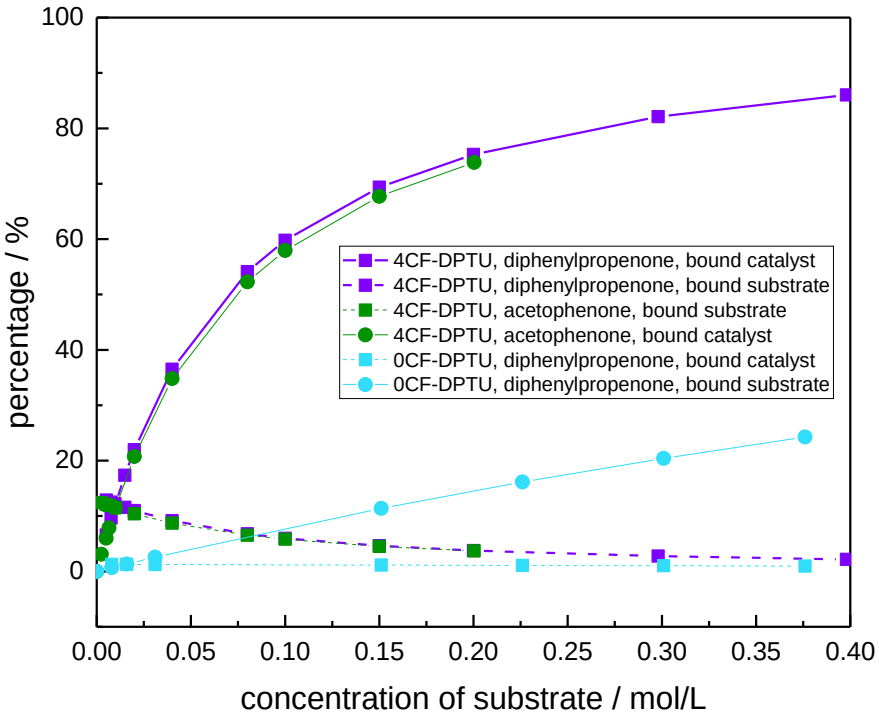

Figure 6-13: Percentage of bound catalyst (solid lines) and bound substrate (dashed lines) extracted from the ^{1}H-NMR association model fits for 4CF-DPTU:acetophenone (green), 4CF-DPTU:diphenylpropenone (purple) and 0CF-DPTU:diphenylpropenone (light blue) in DCM. The catalyst concentration is kept constant at $\boldsymbol{c_{cat}^0}$ = 0.01 mol/L for 4CF-DPTU:acetophenone and 4CF-DPTU:diphenylpropenone and $\boldsymbol{c_{cat}^0}$ = 0.015 mol/L for 0CF-DPTU:diphenylpropenone, while the concentration of the substrate is varied from $\boldsymbol{c_{subs}^0}$ = 0 – 0.4 mol/L.

With the extracted association constants K_{NMR} and the chemical shift of the complex $\delta_{complex}$, the concentration of the formed complex $c_{complex}$ for each concentration of added substrate c^0_{subs} can be calculated *Figure 6-13*. From this, we can determine the percentage of bound catalyst (solid lines) and the percentage of bound substrate (dashed lines) for the studied systems 4CF-DPTU:acetophenone (green), 4CF-DPTU:diphenylproepnone (purple) and 0CF-DPTU:diphenylpropenone (light blue). While the percentage of bound catalyst increases for all studied systems, the percentage of bound substrate decreases, because the total concentration of substrate c^0_{subs} also increases (which leads to a larger concentration of bound substrate, but also to a larger concentration of free substrate), while the concentration of the catalyst c^0_{cat} remains constant. The ratio DPTU:substrate=1:20 was investigated with ultrafast vibrational pump probe IR spectroscopy, which corresponds to a substrate concentration in the NMR measurements of c^0_{subs} = 0.2 mol/L for 4CF-DPTU:acetophenone and 4CF-DPTU:diphenylpropenone and c^0_{subs} = 0.3 mol/L for 0CF-DPTU:diphenylpropenone. This ratio corresponds to >70% bound catalyst for 4CF-DPTU (<5% bound substrate), independent of the substrate. In contrast, 0CF-DPTU:diphenylpropenone, reveals only ~20% bound catalyst (<<5% bound substrate). Consequently, the percentage of bound catalyst depends mainly on the catalyst and only to a minor extend on the substrate.

Effect of complex formation on acetophenone's C=O bond

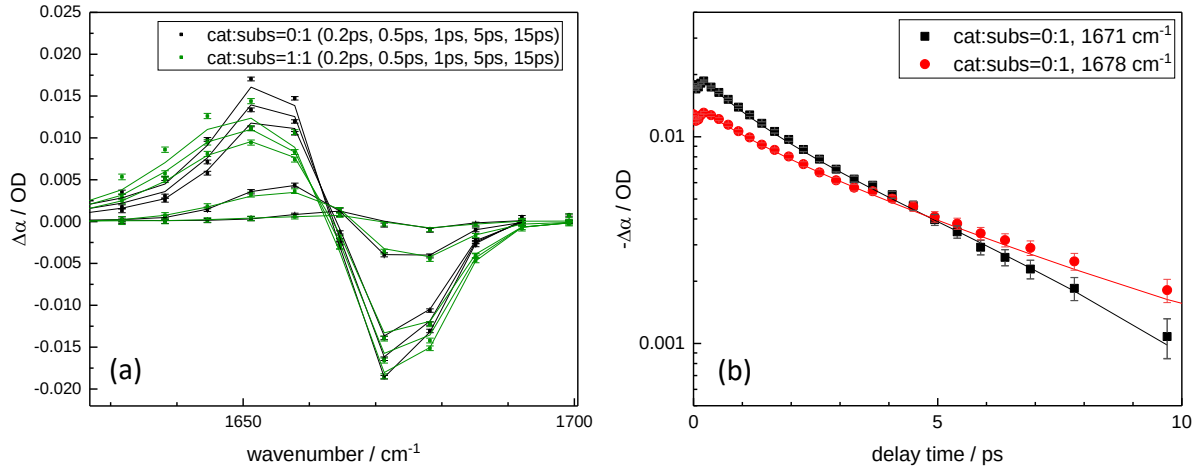

Figure 6-14: (a) Transient fs-IR spectrum of the CO of pure acetophenone (black) and with the catalyst 4CF-DPTU (green) with a ratio of 4CF-DPTU:substrate = 1:1.(b) Time traces for two different wavenumbers for the pure acetophenone. The symbols represent the experimental data and the lines show fits with a parallel model fit with two time constants.

We collected ultrafast vibrational pump probe IR spectra of the pure acetophenone and a mixture with the catalyst at the ratio 4CF-DPTU:substrate = 1:1 (*Figure 6-14*). We observe for acetophenone (black) a negative bleaching signal at ~1675cm^{-1} belonging to

the depopulation of the ground state of the C=O stretching vibration and a red-shifted ESA at ~1655cm^{-1}. The anharmonicity is rather small as the bleach and ESA seem to partly overlap. For the mixture with the catalyst, 4CF-DPTU:substrate = 1:1 (green), we find a nearly perfect overlap of the two bleaches. Yet, the ESA of 4CF-DPTU:substrate = 1:1 is slightly reduced in its maximum amplitude, but contains a larger contribution at lower wavenumbers at ~1620-1640cm-1. This can be attributed to the hydrogen-bonded C=O stretching vibration. It can only be observed for the ESA, as the lower frequency part of the bleach (corresponding to the hydrogen-bonded region) partly overlaps with the ESA of the free C=O and partly cancels (which also results in a slightly reduced amplitude of the ESA at ~1660cm^{-1}). By modeling the experimental data, more than one time constant needs to be taken into account to describe the experimental data, as already is apparent from the time traces, which reveal at least two different vibrational dynamics (*Figure 6-14b*). Analogous to the modeling of the catalysts we assume a parallel model fit with two time constants and obtain the vibrational relaxation times of 4.5ps and 1.1 ps for the pure substrate acetophenone and 5.3ps and 1.7ps for 4CF-DPTU:substrate = 1:1. However, in both cases the fit deviates from the experimental data at early delay times of the ESA. These findings point to more complex vibrational dynamics of the substrates and make it challenging to extract the different species from fs-IR spectroscopy.

7 CONCLUSION AND OUTLOOK

In this thesis, I studied the fundamental interaction of (thio)urea catalysts to ketones and the fundamental hydrogen-bonding dynamics of urea-motifs, in order to get insights into catalyst-substrate binding under catalytically relevant conditions, which is vital to understand and predict catalytic efficiencies. The results of this thesis can contribute to a better understanding of the fundamental catalyst-substrate interaction. This can help to enable a rational catalyst design in the future, by replacing the current approach that mainly consists of trial and error. The main results of each chapter are summarized in the following paragraphs, as well as the questions, which still remain open and how to address them.

In chapter 4, I presented a study of urea-d4/urea mixtures – as a model system for (thio)urea catalysts – in the solvent dimethylsulfoxide (DMSO) with varying degrees of deuteration to investigate the hydrogen-bonds donated by urea and to disentangle the vibrational dynamics of urea. Therefore, I used vibrational spectroscopy methods, more specifically, linear IR spectroscopy and 2D-IR spectroscopy combined with DFT-calculations. The linear IR spectra exhibited spectrally separated infrared absorption bands for ND_2 and ND stretching modes, with the ND mode being broader than the ND_2 modes. This was also observed in the 2D-IR spectra, which revealed ~1.5-2 times larger inhomogeneous linewidths for the ND compared to the ND_2 modes. However, the homogeneous linewidths and the vibrational lifetimes (~ 0.6 – 0.9ps) were similar for the ND and ND_2 modes. From the larger inhomogeneous broadening for ND compared to ND_2, it could be concluded that the hydrogen-bond environments give rise to a broader frequency range for ND compared to ND_2 modes. DFT calculations could explain this experimental observation with a marked asymmetry in the strength of the two hydrogen-bonds donated by an ND_2 group. Further experimental analysis revealed that this asymmetry persists over a rather long time of ~1ps, indicating a surprisingly long-lived inhomogeneity of hydrogen-bonding environments.

As catalysts are known to provide a larger catalytic conversion if they contain CF_3 substituents, I investigated in chapter 5 substituted diphenylthiourea (DPTU) catalysts with zero (0CF-DPTU), two (2CF-DPTU) and four CF_3-groups (4CF-DPTU) at the phenylring upon binding to the substrate 1,3-diphenyl-2-propenone in various solvents. Two independent techniques were used to quantify the association strength of the catalyst-substrate binding in solution: Upon binding to the substrate, thiourea's NH proton was followed with ^{1}H-NMR spectroscopy and the NH stretching vibration of the thiourea catalysts were investigated with linear IR spectroscopy. For both approaches it was sufficient to describe the experimental data with a bimolecular association and the obtained association constants from both methods agree very well. The solvents

dichloromethane and toluene yielded increasing association constants from ~1 L/mol – 30 L/mol for an increasing number of CF_3 substituents (from 0CF-DPTU to 4CF-DPTU), while there was no detectable association in acetonitrile, suggesting that also the solvation of the catalyst, the substrate and the complex contributes to the molecular association. This enhanced binding with increasing number of CF_3-groups for rather unpolar solvents (e.g. dichloromethane) correlated well with their increased catalytic activity reported in literature and can explain the increased reaction rates observed for CF_3 substituted diphenylthiourea catalysts.

In chapter 6, a similar approach was used, where I used a combination of ^{1}H-NMR, linear IR, fs-IR and 2D-IR spectroscopy in order to study the influence of the substrate and of the different conformational states of the catalysts on the catalyst-substrate binding. Therefore, I used acetophenone as model system for the substrate and compared it to diphenylpropenone by studying their binding to the catalysts 4CF-DPTU, 2CF-DPTU and 0CF-DPTU. I used ^{1}H-NMR spectroscopy to detect molecular association. This revealed similar association constants by changing the substrate. However the substrate acetophenone exhibited a siginificant decrease in the chemical shift of the complex $\delta_{complex}$ compared to diphenylpropenone, which indicates a somewhat stronger interaction with diphenylpropenone. The hydrogen-bonded catalyst-substrate complexes give rise to spectrally separated absorption bands in the NH region of the catalyst and in the CO region of the substrate in the FT-IR spectra, indicative for a weakening of the molecular bonds. By investigating the NH modes of thiourea catalysts with fs-IR spectroscopy, the two catalytic conformers, trans-trans and trans-cis, could be discriminated based on their significantly different vibrational lifetimes. In mixtures of catalyst with substrate, I could resolve three different molecular states, the trans-trans and trans-cis conformer and the hydrogen-bonded complex, whereas the third significantly shorter vibrational relaxation of ~0.6ps was assigned to the hydrogen-bonded species. The obtained spectra of the trans-cis conformer contained spectral components of the hydrogen-bonded complex in the presence of the substrate, suggesting that hydrogen-bonding to the substrate only occurs for this conformer within the experimental time window.

In this work, I found a long-lived inhomogeneity and asymmetry in hydrogen-bond strength of urea, which raises the question, if this property is characteristic to urea itself or if this is a general observation for hydrogen-bonding donors consisting of a XH_2-group (X=N,O,…). For this purpose, it would be interesting to measure for instance 2D-IR spectra of H2O/D2O in DMSO and determine their linewidths, similar to the approach presented in chapter 5, in order to find out if this asymmetry is also relevant for water. Additionally, the asymmetry is of high interest for other applications, as it could be the key to understand the high directionality of urea's hydrogen-bond properties, which might explain the biological activity of urea towards proteins and might be relevant for molecular self-assembly or DNA base-pairing, suggesting that further studies in these fields could be designed based on this knowledge.

I further explored the different conformations of the thiourea catalysts and suggested that only one conformer is relevant for the binding to the substrate. However, the influence of the conformational state on the catalytic activity is still an open question. Therefore, it would be of considerable interest to investigate conformational more stable catalysts, for instance a thiourea catalyst, where both side groups are connected via a covalent bond, which captures the catalyst in a specific configuration and to study their catalytic activity. This could help to understand the contribution of the two conformers to the catalyst-substrate binding.

Additionally, it would be very interesting to explore the binding angle of the substrate in the binding pocket of the catalyst, which can be done with two-color pump probe IR spectroscopy. This might be interesting for the here studied systems, but also for a chiral thiourea catalyst (for instance Takemoto's bifunctional chiral thiourea derivative) in order to elucidate how chirality can be transferred to a substrate.

8 REFERENCES

1 Wisniak, J. The History of Catalysis. From the Beginning to Nobel Prizes. *Educación Química* **21**, 60-69, doi:https://doi.org/10.1016/S0187-893X(18)30074-0 (2010).

2 Schüth, F. Heterogene Katalyse. Schlüsseltechnologie der chemischen Industrie. *Chemie in unserer Zeit* **40**, 92-103, doi:https://doi.org/10.1002/ciuz.200600374 (2006).

3 Van Houten, J. A Century of Chemical Dynamics Traced through the Nobel Prizes. 1909: Wilhelm Ostwald. *Journal of Chemical Education* **79**, 146, doi:10.1021/ed079p146 (2002).

4 Vogel, P., Lam, Y. H., Simon, A. & Houk, K. N. Organocatalysis: Fundamentals and Comparisons to Metal and Enzyme Catalysis. *Catalysts* **6**, 65, doi:10.3390/catal6090128 (2016).

5 Atkins, P. W. d. P., Julio. *Physikalische Chemie*. (Wiley-VCH, Weinheim, 2013).

6 in *Catalyst Design: Optimal Distribution of Catalyst in Pellets, Reactors, and Membranes Cambridge Series in Chemical Engineering* (eds Arvind Varma, Asterios Gavriilidis, & Massimo Morbidelli) 1-5 (Cambridge University Press, 2001).

7 Humphreys, J., Lan, R. & Tao, S. Development and Recent Progress on Ammonia Synthesis Catalysts for Haber–Bosch Process. *Advanced Energy and Sustainability Research* **n/a**, 2000043, doi:https://doi.org/10.1002/aesr.202000043.

8 Erisman, J. W., Sutton, M. A., Galloway, J., Klimont, Z. & Winiwarter, W. How a century of ammonia synthesis changed the world. *Nature Geoscience* **1**, 636-639, doi:10.1038/ngeo325 (2008).

9 Farnetti, E., Monte, R. & Kaapar, J.

10 Yuryev, R. & Liese, A. Biocatalysis: The Outcast. *ChemCatChem* **2**, 103-107, doi:https://doi.org/10.1002/cctc.200900126 (2010).

11 Hopmann, K. H. Quantum chemical studies of asymmetric reactions: Historical aspects and recent examples. *International Journal of Quantum Chemistry* **115**, 1232-1249, doi:https://doi.org/10.1002/qua.24882 (2015).

12 Zhou, Q.-L. Transition-Metal Catalysis and Organocatalysis: Where Can Progress Be Expected? *Angewandte Chemie International Edition* **55**, 5352-5353, doi:https://doi.org/10.1002/anie.201509164 (2016).

13 MacMillan, D. W. C. The advent and development of organocatalysis. *Nature* **455**, 304-308, doi:10.1038/nature07367 (2008).

14 Tu, Y., Wang, Z.-X. & Shi, Y. An Efficient Asymmetric Epoxidation Method for trans-Olefins Mediated by a Fructose-Derived Ketone. *Journal of the American Chemical Society* **118**, 9806-9807, doi:10.1021/ja962345g (1996).

15 Denmark, S. E., Wu, Z., Crudden, C. M. & Matsuhashi, H. Catalytic Epoxidation of Alkenes with Oxone. 2. Fluoro Ketones. *The Journal of Organic Chemistry* **62**, 8288-8289, doi:10.1021/jo971781y (1997).

16 Yang, D. *et al.* A C2 Symmetric Chiral Ketone for Catalytic Asymmetric Epoxidation of Unfunctionalized Olefins. *Journal of the American Chemical Society* **118**, 491-492, doi:10.1021/ja9529549 (1996).

17 Dalko, P. I. & Moisan, L. In the Golden Age of Organocatalysis. *Angewandte Chemie International Edition* **43**, 5138-5175, doi:10.1002/anie.200400650 (2004).

18 Takemoto, Y. Development of Chiral Thiourea Catalysts and Its Application to Asymmetric Catalytic Reactions. *Chemical and Pharmaceutical Bulletin* **58**, 593-601, doi:10.1248/cpb.58.593 (2010).

19 Yoon, T. P. & Jacobsen, E. N. Privileged Chiral Catalysts. *Science* **299**, 1691-1693, doi:10.1126/science.1083622 (2003).

20 Taylor, M. S. & Jacobsen, E. N. Asymmetric Catalysis by Chiral Hydrogen-Bond Donors. *Angewandte Chemie International Edition* **45**, 1520-1543, doi:10.1002/anie.200503132 (2006).

21 Knowles, R. R. & Jacobsen, E. N. Attractive noncovalent interactions in asymmetric catalysis: Links between enzymes and small molecule catalysts. *Proceedings of the National Academy of Sciences* **107**, 20678-20685, doi:10.1073/pnas.1006402107 (2010).

22 Schreiner, P. R. & Wittkopp, A. H-Bonding Additives Act Like Lewis Acid Catalysts. *Organic Letters* **4**, 217-220, doi:10.1021/ol017117s (2002).

23 Wittkopp, A. & Schreiner, P. R. Metal-Free, Noncovalent Catalysis of Diels–Alder Reactions by Neutral Hydrogen Bond Donors in Organic Solvents and in Water. *Chemistry – A European Journal* **9**, 407-414, doi:10.1002/chem.200390042 (2003).

24 Schreiner, P. R. Metal-free organocatalysis through explicit hydrogen bonding interaction. *Royal Society of Chemistry* **32**, 289-296, doi:10.1039/B107298F (2003).

25 Zhang, Z. & Schreiner, P. R. (Thio)urea organocatalysis—What can be learnt from anion recognition? *Chemical Society Reviews* **38**, 1187-1198, doi:10.1039/B801793J (2009).

26 Sigman, M. S., Vachal, P. & Jacobsen, E. N. A General Catalyst for the Asymmetric Strecker Reaction. *Angewandte Chemie International Edition* **39**, 1279-1281, doi:10.1002/(SICI)1521-3773(20000403)39:7<1279::AID-ANIE1279>3.0.CO;2-U (2000).

27 Sigman, M. S. & Jacobsen, E. N. Schiff Base Catalysts for the Asymmetric Strecker Reaction Identified and Optimized from Parallel Synthetic Libraries. *Journal of the American Chemical Society* **120**, 4901-4902, doi:10.1021/ja980139y (1998).

28 Okino, T., Hoashi, Y. & Takemoto, Y. Enantioselective Michael Reaction of Malonates to Nitroolefins Catalyzed by Bifunctional Organocatalysts. *Journal of the American Chemical Society* **125**, 12672-12673, doi:10.1021/ja036972z (2003).

29 Takemoto, Y. Recognition and activation by ureas and thioureas: stereoselective reactions using ureas and thioureas as hydrogen-bonding donors. *Organic & Biomolecular Chemistry* **3**, 4299-4306, doi:10.1039/B511216H (2005).

30 Lippert, K. M. *et al.* Hydrogen-Bonding Thiourea Organocatalysts: The Privileged 3,5-Bis(trifluoromethyl)phenyl Group. *European Journal of Organic Chemistry* **2012**, 5919-5927, doi:10.1002/ejoc.201200739 (2012).

31 Žabka, M. & Šebesta, R. Experimental and Theoretical Studies in Hydrogen-Bonding Organocatalysis. **20**, 15500-15524 (2015).

32 Jakab, G., Tancon, C., Zhang, Z., Lippert, K. M. & Schreiner, P. R. (Thio)urea Organocatalyst Equilibrium Acidities in DMSO. *Organic Letters* **14**, 1724-1727, doi:10.1021/ol300307c (2012).

33 Walvoord, R. R., Huynh, P. N. H. & Kozlowski, M. C. Quantification of Electrophilic Activation by Hydrogen-Bonding Organocatalysts. *Journal of the American Chemical Society* **136**, 16055-16065, doi:10.1021/ja5086244 (2014).

34 Serdyuk, O. V., Heckel, C. M. & Tsogoeva, S. B. Bifunctional primary amine-thioureas in asymmetric organocatalysis. *Organic & Biomolecular Chemistry* **11**, 7051-7071, doi:10.1039/C3OB41403E (2013).

35 Fang, X. & Wang, C.-J. Recent advances in asymmetric organocatalysis mediated by bifunctional amine-thioureas bearing multiple hydrogen-bonding donors. *Chemical Communications* **51**, 1185-1197, doi:10.1039/C4CC07909D (2015).

36 Kleiner, C. M. & Schreiner, P. R. Hydrophobic amplification of noncovalent organocatalysis. *Chemical Communications*, 4315-4317, doi:10.1039/B605850G (2006).

37 Zhang, Z., Lippert, K. M., Hausmann, H., Kotke, M. & Schreiner, P. R. Cooperative Thiourea–Brønsted Acid Organocatalysis: Enantioselective Cyanosilylation of Aldehydes with TMSCN. *The Journal of Organic Chemistry* **76**, 9764-9776, doi:10.1021/jo201864e (2011).

38 Connon, S. J. Organocatalysis Mediated by (Thio)urea Derivatives. *Chemistry – A European Journal* **12**, 5418-5427, doi:10.1002/chem.200501076 (2006).

39 Ana Alcaine, E. M.-L. a. R. P. H. Synthesis of interesting β-nitrohydrazides through a thiourea organocatalysed aza-Michael addition. *Royal Society of Chemistry* **4**, 9856-9865 (2014).

40 Lutete, L. M., Miyamoto, T. & Ikemoto, T. Tertiary amino thiourea-catalyzed asymmetric cross aldol reaction of aryl methyl ketones with aryl trifluoromethyl ketones. *Tetrahedron Letters* **57**, 1220-1223, doi:https://doi.org/10.1016/j.tetlet.2016.02.001 (2016).

41 Brini, E. *et al.* How Water's Properties Are Encoded in Its Molecular Structure and Energies. *Chemical Reviews* **117**, 12385-12414, doi:10.1021/acs.chemrev.7b00259 (2017).

42 Ball, P. Water — an enduring mystery. *Nature* **452**, 291-292, doi:10.1038/452291a (2008).

43 Greve, C. & Elsaesser, T. Ultrafast Two-Dimensional Infrared Spectroscopy of Guanine–Cytosine Base Pairs in DNA Oligomers. *The Journal of Physical Chemistry B* **117**, 14009-14017, doi:10.1021/jp408229k (2013).

44 Watson, J. D. & Crick, F. H. C. Molecular Structure of Nucleic Acids: A Structure for Deoxyribose Nucleic Acid. *Nature* **171**, 737-738, doi:10.1038/171737a0 (1953).

45 Spencer, M. The stereochemistry of deoxyribonucleic acid. II. Hydrogen-bonded pairs of bases. *Acta Crystallographica* **12**, 66-71, doi:doi:10.1107/S0365110X59000160 (1959).

46 Saenger, W. *Principles of Nucleic Acid Structure*. (Springer, New York, NY, 1984).

47 Pauling, L., Corey, R. B. & Branson, H. R. The structure of proteins: Two hydrogen-bonded helical configurations of the polypeptide chain. *Proceedings of the National Academy of Sciences* **37**, 205-211, doi:10.1073/pnas.37.4.205 (1951).

48 Peters, D. & Peters, J. The Ribbon of Hydrogen Bonds in the Three-Dimensional Structure of Globular Proteins. *Molecular Engineering* **8**, 345-356, doi:10.1023/A:1008321322623 (1999).

49 Pauling, L. The Shared-Electron Chemical Bond. *Proceedings of the National Academy of Sciences of the United States of America* **14**, 359-362, doi:10.1073/pnas.14.4.359 (1928).

50 Laurence, C. & Berthelot, M. Observations on the strength of hydrogen bonding. *Perspectives in Drug Discovery and Design* **18**, 39-60, doi:10.1023/A:1008743229409 (2000).
51 Emsley, J. Very strong hydrogen bonding. *Chemical Society Reviews* **9**, 91-124, doi:10.1039/CS9800900091 (1980).
52 Elsaesser, T. in *Ultrafast Infrared Vibrational Spectroscopy*

(ed M.D. (Ed.) Fayer) (CRC Press, 2013).
53 Nibbering, E. T. J. & Elsaesser, T. Ultrafast Vibrational Dynamics of Hydrogen Bonds in the Condensed Phase. *Chemical Reviews* **104**, 1887-1914, doi:10.1021/cr020694p (2004).
54 Cowan, M. L. *et al.* Ultrafast memory loss and energy redistribution in the hydrogen bond network of liquid H2O. *Nature* **434**, 199-202, doi:10.1038/nature03383 (2005).
55 Ratajczak, H. & Orville-Thomas, W. J. Hydrogen-bond studies: Part I. The relation between vibrational frequencies and bond length in O-H β O hydrogen-bonded systems. *Journal of Molecular Structure* **1**, 449-461, doi:https://doi.org/10.1016/0022-2860(68)87019-X (1968).
56 Elsässer, T. & Becker, H. *Ultrafast hydrogen bonding dynamics and proton transfer processes in the condensed phase*. Vol. 23 (Springer Science & Business Media, 2013).
57 Bakker, H. & Bonn, M. (ed M. D. Fayer) (CRC Press).
58 Lee, F. NMR Methods for the Determination of Protein- Ligand Dissociation Constants. *Current Topics in Medicinal Chemistry* **3**, 39-53, doi:http://dx.doi.org/10.2174/1568026033392705 (2003).
59 Haushalter, K. A., Lau, J. & Roberts, J. D. An NMR Investigation of the Effect of Hydrogen Bonding on the Rates of Rotation about the C−N Bonds in Urea and Thiourea. *Journal of the American Chemical Society* **118**, 8891-8896, doi:10.1021/ja961380k (1996).
60 Arunan, E. *et al.* Definition of the hydrogen bond (IUPAC Recommendations 2011). *Pure and Applied Chemistry* **83**, 1637-1641, doi:https://doi.org/10.1351/PAC-REC-10-01-02 (2011).
61 Le Parc, R. *et al.* Infrared and Raman spectroscopy of non-conventional hydrogen bonding between N,N′-disubstituted urea and thiourea groups: a combined experimental and theoretical investigation. *Physical Chemistry Chemical Physics* **21**, 3310-3317, doi:10.1039/C8CP06625F (2019).
62 Dantus, M., Bowman, R. M. & Zewail, A. H. Femtosecond laser observations of molecular vibration and rotation. *Nature* **343**, 737-739, doi:10.1038/343737a0 (1990).
63 Mazur, K., Bonn, M. & Hunger, J. Hydrogen Bond Dynamics in Primary Alcohols: A Femtosecond Infrared Study. *The Journal of Physical Chemistry B* **119**, 1558-1566, doi:10.1021/jp509816q (2015).
64 Hunger, J. *et al.* Hydrogen-Bond Dynamics in a Protic Ionic Liquid: Evidence of Large-Angle Jumps. *The Journal of Physical Chemistry Letters* **3**, 3034-3038, doi:10.1021/jz301334j (2012).
65 Hamm, P. Femtosecond IR pump-probe spectroscopy of nonlinear energy localization in protein models and model proteins. *J Biol Phys* **35**, 17-30, doi:10.1007/s10867-009-9126-3 (2009).

66 Elsaesser, T. Two-Dimensional Infrared Spectroscopy of Intermolecular Hydrogen Bonds in the Condensed Phase. *Accounts of Chemical Research* **42**, 1220-1228, doi:10.1021/ar900006u (2009).

67 P. Hamm, M. Z. Concepts and Methods of 2D Infrared Spectroscopy. *Cambridge University Press* **Oxford, UK** (2011).

68 Shim, S.-H. & Zanni, M. T. How to turn your pump–probe instrument into a multidimensional spectrometer: 2D IR and Vis spectroscopiesvia pulse shaping. *Physical Chemistry Chemical Physics* **11**, 748-761, doi:10.1039/B813817F (2009).

69 Demtröder, W. *Experimentalphysik 2: Elektrizität und Optik*. (Springer Berlin Heidelberg, 2018).

70 Parson, W. W. *Modern Optical Spectroscopy*. (Springer-Verlag Berlin Heidelberg, 2007).

71 Petrascheck, D. & Schwabl, F. in *Elektrodynamik* 157-197 (Springer Berlin Heidelberg, 2016).

72 Boyd, R. W. in *Nonlinear Optics (Third Edition)* (ed Robert W. Boyd) 69-133 (Academic Press, 2008).

73 Gerd Wedler, H.-J. F. *Lehr- und Arbeitsbuch Physikalische Chemie*. (Wiley-VCH Verlag GmbH & Co. KGaA, 2019).

74 Lambert, A. G., Davies, P. B. & Neivandt, D. J. Implementing the Theory of Sum Frequency Generation Vibrational Spectroscopy: A Tutorial Review. *Applied Spectroscopy Reviews* **40**, 103-145, doi:10.1081/ASR-200038326 (2005).

75 Hollas, J. M. *Modern Spectroscopy*. (Wiley, 2004).

76 Boyd, R. W. in *Nonlinear Optics (Third Edition)* (ed Robert W. Boyd) 1-67 (Academic Press, 2008).

77 Cho, M. in *Coherent Multidimensional Spectroscopy* (ed Minhaeng Cho) 1-34 (Springer Singapore, 2019).

78 Park, S., Kwak, K. & Fayer, M. D. Ultrafast 2D-IR vibrational echo spectroscopy: a probeof molecular dynamics. **4**, 704-718, doi:doi:10.1002/lapl.200710046 (2007).

79 Fayer, M. D. E. Ultrafast Infrared Vibrational Spectroscopy. *CRC Press*, doi:https://doi.org/10.1201/b13972 (2013).

80 Tokmakoff, A. & Fayer, M. D. Homogeneous vibrational dynamics and inhomogeneous broadening in glass-forming liquids: Infrared photon echo experiments from room temperature to 10 K. *The Journal of Chemical Physics* **103**, 2810-2826, doi:10.1063/1.470517 (1995).

81 Milder, M. T. W. *Energy transfer in (bio)molecular systems*, (2010).

82 Selig, O. *Ultrasensitive nonlinear vibrational spectroscopy of complex molecular systems*, (2017).

83 Balci, M. in *Basic 1H- and 13C-NMR Spectroscopy* (ed Metin Balci) 9-24 (Elsevier Science, 2005).

84 A. K. Covington, T. D. *Physical Chemistry of Organic Solvent Systems*. (Springer, Boston, MA, 1973).

85 Balci, M. in *Basic 1H- and 13C-NMR Spectroscopy* (ed Metin Balci) 25-85 (Elsevier Science, 2005).

86 Balci, M. in *Basic 1H- and 13C-NMR Spectroscopy* (ed Metin Balci) 241-251 (Elsevier Science, 2005).

87 Bowen, S. & Hilty, C. Time-Resolved Dynamic Nuclear Polarization Enhanced NMR Spectroscopy. *Angewandte Chemie International Edition* **47**, 5235-5237, doi:10.1002/anie.200801492 (2008).

88 Hunger, J., Tielrooij, K.-J., Buchner, R., Bonn, M. & Bakker, H. J. Complex Formation in Aqueous Trimethylamine-N-oxide (TMAO) Solutions. *The Journal of Physical Chemistry B* **116**, 4783-4795, doi:10.1021/jp212542q (2012).

89 Hunger, J., Liu, L., Tielrooij, K.-J., Bonn, M. & Bakker, H. Vibrational and orientational dynamics of water in aqueous hydroxide solutions. *The Journal of Chemical Physics* **135**, 124517, doi:10.1063/1.3643763 (2011).

90 Middleton, C. T., Woys, A. M., Mukherjee, S. S. & Zanni, M. T. Residue-specific structural kinetics of proteins through the union of isotope labeling, mid-IR pulse shaping, and coherent 2D IR spectroscopy. *Methods* **52**, 12-22, doi:https://doi.org/10.1016/j.ymeth.2010.05.002 (2010).

91 Strasfeld, D. B., Shim, S.-H. & Zanni, M. T. Controlling Vibrational Excitation with Shaped Mid-IR Pulses. *Physical Review Letters* **99**, 038102, doi:10.1103/PhysRevLett.99.038102 (2007).

92 Strasfeld, D. B., Middleton, C. T. & Zanni, M. T. Mode selectivity with polarization shaping in the mid-IR. *New Journal of Physics* **11**, 105046, doi:10.1088/1367-2630/11/10/105046 (2009).

93 Shim, S.-H., Strasfeld, D. B., Ling, Y. L. & Zanni, M. T. Automated 2D IR spectroscopy using a mid-IR pulse shaper and application of this technology to the human islet amyloid polypeptide. *Proceedings of the National Academy of Sciences* **104**, 14197-14202, doi:10.1073/pnas.0700804104 (2007).

94 Shim, S.-H., Strasfeld, D. B., Fulmer, E. C. & Zanni, M. T. Femtosecond pulse shaping directly in the mid-IR using acousto-optic modulation. *Opt. Lett.* **31**, 838-840, doi:10.1364/OL.31.000838 (2006).

95 Hillegas, C. W., Tull, J. X., Goswami, D., Strickland, D. & Warren, W. S. Femtosecond laser pulse shaping by use of microsecond radio-frequency pulses. *Opt. Lett.* **19**, 737-739, doi:10.1364/OL.19.000737 (1994).

96 Shim, S. H., Strasfeld, D. B. & Zanni, M. T. Generation and characterization of phase and amplitude shaped femtosecond mid-IR pulses. *Opt Express* **14**, 13120-13130, doi:10.1364/oe.14.013120 (2006).

97 Hoccart, X. & Turrell, G. Raman spectroscopic investigation of the dynamics of urea–water complexes. *The Journal of Chemical Physics* **99**, 8498-8503, doi:10.1063/1.465626 (1993).

98 Zou, Q., Bennion, B. J., Daggett, V. & Murphy, K. P. The Molecular Mechanism of Stabilization of Proteins by TMAO and Its Ability to Counteract the Effects of Urea. *Journal of the American Chemical Society* **124**, 1192-1202, doi:10.1021/ja004206b (2002).

99 Bennion, B. J. & Daggett, V. Counteraction of urea-induced protein denaturation by trimethylamine N-oxide: A chemical chaperone at atomic resolution. *Proceedings of the National Academy of Sciences of the United States of America* **101**, 6433-6438, doi:10.1073/pnas.0308633101 (2004).

100 Hunger, J., Ottosson, N., Mazur, K., Bonn, M. & Bakker, H. J. Water-mediated interactions between trimethylamine-N-oxide and urea. *Physical Chemistry Chemical Physics* **17**, 298-306, doi:10.1039/C4CP02709D (2015).

101 Kuffel, A. & Zielkiewicz, J. The hydrogen bond network structure within the hydration shell around simple osmolytes: Urea, tetramethylurea, and trimethylamine-N-oxide, investigated using both a fixed charge and a polarizable water model. *The Journal of Chemical Physics* **133**, 035102, doi:10.1063/1.3464768 (2010).

102 Grdadolnik, J. & Maréchal, Y. Bovine serum albumin observed by infrared spectrometry. I. Methodology, structural investigation, and water uptake. *Biopolymers* **62**, 40-53, doi:10.1002/1097-0282(2001)62:1<40::Aid-bip60>3.0.Co;2-c (2001).

103 Mountain, R. D. & Thirumalai, D. Molecular Dynamics Simulations of End-to-End Contact Formation in Hydrocarbon Chains in Water and Aqueous Urea Solution. *Journal of the American Chemical Society* **125**, 1950-1957, doi:10.1021/ja020496f (2003).

104 Klimov, D. K., Straub, J. E. & Thirumalai, D. Aqueous urea solution destabilizes Aβ_{16–22} oligomers. *Proceedings of the National Academy of Sciences of the United States of America* **101**, 14760-14765, doi:10.1073/pnas.0404570101 (2004).

105 Hua, L., Zhou, R., Thirumalai, D. & Berne, B. J. Urea denaturation by stronger dispersion interactions with proteins than water implies a 2-stage unfolding. *Proceedings of the National Academy of Sciences* **105**, 16928-16933, doi:10.1073/pnas.0808427105 (2008).

106 Rezus, Y. L. A. & Bakker, H. J. Effect of urea on the structural dynamics of water. **103**, 18417-18420, doi:10.1073/pnas.0606538103 %J Proceedings of the National Academy of Sciences (2006).

107 Sofronov, O. O. & Bakker, H. J. Energy Relaxation and Structural Dynamics of Protons in Water/DMSO Mixtures. *The journal of physical chemistry. B* **122**, 10005-10013, doi:10.1021/acs.jpcb.8b06938 (2018).

108 Lotze, S., Groot, C. C. M., Vennehaug, C. & Bakker, H. J. Femtosecond Mid-Infrared Study of the Dynamics of Water Molecules in Water–Acetone and Water–Dimethyl Sulfoxide Mixtures. *The Journal of Physical Chemistry B* **119**, 5228-5239, doi:10.1021/jp512703w (2015).

109 Kashid, S. M., Jin, G. Y., Bagchi, S. & Kim, Y. S. Cosolvent Effects on Solute–Solvent Hydrogen-Bond Dynamics: Ultrafast 2D IR Investigations. *The Journal of Physical Chemistry B* **119**, 15334-15343, doi:10.1021/acs.jpcb.5b08643 (2015).

110 Wallace, V. M., Dhumal, N. R., Zehentbauer, F. M., Kim, H. J. & Kiefer, J. Revisiting the Aqueous Solutions of Dimethyl Sulfoxide by Spectroscopy in the Mid- and Near-Infrared: Experiments and Car–Parrinello Simulations. *The Journal of Physical Chemistry B* **119**, 14780-14789, doi:10.1021/acs.jpcb.5b09196 (2015).

111 Kuffel, A. & Zielkiewicz, J. The hydrogen bond network structure within the hydration shell around simple osmolytes: urea, tetramethylurea, and trimethylamine-N-oxide, investigated using both a fixed charge and a polarizable water model. *J Chem Phys* **133**, 035102, doi:10.1063/1.3464768 (2010).

112 Sharp, K. A. & Vanderkooi, J. M. Water in the Half Shell: Structure of Water, Focusing on Angular Structure and Solvation. *Accounts of Chemical Research* **43**, 231-239, doi:10.1021/ar900154j (2010).

113 Wei, H., Fan, Y. & Gao, Y. Q. Effects of Urea, Tetramethyl Urea, and Trimethylamine N-Oxide on Aqueous Solution Structure and Solvation of Protein Backbones: A Molecular Dynamics Simulation Study. *The Journal of Physical Chemistry B* **114**, 557-568, doi:10.1021/jp9084926 (2010).

114 Soper, A. K., Castner, E. W. & Luzar, A. Impact of urea on water structure: a clue to its properties as a denaturant? *Biophysical Chemistry* **105**, 649-666, doi:https://doi.org/10.1016/S0301-4622(03)00095-4 (2003).

115 Yang, Z., Xiu, P., Shi, B., Hua, L. & Zhou, R. Coherent Microscopic Picture for Urea-Induced Denaturation of Proteins. *The Journal of Physical Chemistry B* **116**, 8856-8862, doi:10.1021/jp304114h (2012).

116 Pazos, I. M. & Gai, F. Solute's Perspective on How Trimethylamine Oxide, Urea, and Guanidine Hydrochloride Affect Water's Hydrogen Bonding Ability. *The Journal of Physical Chemistry B* **116**, 12473-12478, doi:10.1021/jp307414s (2012).

117 Hua, L., Zhou, R., Thirumalai, D. & Berne, B. J. Urea denaturation by stronger dispersion interactions with proteins than water implies a 2-stage unfolding. *Proceedings of the National Academy of Sciences of the United States of America* **105**, 16928-16933, doi:10.1073/pnas.0808427105 (2008).

118 Volz, N. & Clayden, J. The Urea Renaissance. *Angewandte Chemie International Edition* **50**, 12148-12155, doi:10.1002/anie.201104037 (2011).

119 Wang, L. M., Zhao, M. J., Chen, Z., Mu, H. W. & Jin, Y. Urea derivative catalyzed enantioselective aldol reaction of isatins with ketones. **30**, 1005-1011, doi:doi:10.1002/chir.22977 (2018).

120 Sun, L. F., Wu, X. W., Xiong, D. C. & Ye, X. S. Stereoselective Koenigs-Knorr Glycosylation Catalyzed by Urea. *Angew. Chem.-Int. Edit.* **55**, 8041-8044, doi:10.1002/anie.201600142 (2016).

121 Biedermann, F. & Schneider, H.-J. Experimental Binding Energies in Supramolecular Complexes. *Chemical Reviews* **116**, 5216-5300, doi:10.1021/acs.chemrev.5b00583 (2016).

122 De Greef, T. F. A. *et al.* Supramolecular Polymerization. *Chemical Reviews* **109**, 5687-5754, doi:10.1021/cr900181u (2009).

123 Custelcean, R. Crystal engineering with urea and thiourea hydrogen-bonding groups. *Chemical Communications*, 295-307, doi:10.1039/B708921J (2008).

124 Kraack, J. P. Ultrafast structural molecular dynamics investigated with 2D infrared spectroscopy methods. *Topics in Current Chemistry* **375**, 86, doi:10.1007/s41061-017-0172-1 (2017).

125 Marekha, B. A. & Hunger, J. Hydrophobic pattern of alkylated ureas markedly affects water rotation and hydrogen bond dynamics in aqueous solution. *Physical Chemistry Chemical Physics* **21**, 20672-20677, doi:10.1039/C9CP04108G (2019).

126 Shaw, D. J., Panman, M. R. & Woutersen, S. Evidence for Cooperative Vibrational Relaxation of the NH-, OH-, and OD-Stretching Modes in Hydrogen-Bonded Liquids Using Infrared Pump-Probe Spectroscopy. *Physical Review Letters* **103**, 227401, doi:10.1103/PhysRevLett.103.227401 (2009).

127 Knop, S., Lindner, J. & Vöhringer, P. OH and NH Stretching Vibrational Relaxation of Liquid Ethanolamine. *Zeitschrift für Physikalische Chemie* **225**, 913, doi:https://doi.org/10.1524/zpch.2011.0125 (2011).

128 Schäfer, T., Kandratsenka, A., Vöhringer, P., Schroeder, J. & Schwarzer, D. Vibrational energy relaxation of the ND-stretching vibration of NH2D in liquid NH3. *Physical Chemistry Chemical Physics* **14**, 11651-11656, doi:10.1039/C2CP41382E (2012).

129 Zheng, Z.-P. *et al.* Ionic Liquids: Not only Structurally but also Dynamically Heterogeneous. *Angewandte Chemie International Edition* **54**, 687-690, doi:10.1002/anie.201409136 (2015).

130 Woutersen, S. & Cristalli, G. Strong enhancement of vibrational relaxation by Watson-Crick base pairing. *The Journal of Chemical Physics* **121**, 5381-5386, doi:10.1063/1.1785153 (2004).

131 Fidder, H. *et al.* N–H Stretching Vibrations of Guanosine–Cytidine Base Pairs in Solution: Ultrafast Dynamics, Couplings, and Line Shapes. *The Journal of Physical Chemistry A* **117**, 845-854, doi:10.1021/jp309237u (2013).

132 Yang, M. *et al.* Dynamics and Couplings of N–H Stretching Excitations of Guanosine–Cytidine Base Pairs in Solution. *The Journal of Physical Chemistry B* **115**, 5484-5492, doi:10.1021/jp110561d (2011).

133 Greve, C. *et al.* N–H Stretching Excitations in Adenosine-Thymidine Base Pairs in Solution: Pair Geometries, Infrared Line Shapes, and Ultrafast Vibrational Dynamics. *The Journal of Physical Chemistry A* **117**, 594-606, doi:10.1021/jp310177e (2013).

134 Rubtsov, I. V., Wang, J. & Hochstrasser, R. M. Vibrational Coupling between Amide-I and Amide-A Modes Revealed by Femtosecond Two Color Infrared Spectroscopy. *The Journal of Physical Chemistry A* **107**, 3384-3396, doi:10.1021/jp021922m (2003).

135 Rubtsov, I. V., Wang, J. & Hochstrasser, R. M. Dual frequency 2D-IR of peptide amide-A and amide-I modes. *The Journal of Chemical Physics* **118**, 7733-7736, doi:10.1063/1.1570398 (2003).

136 Idrissi, A., Sokolić, F. & Perera, A. A molecular dynamics study of the urea/water mixture. *The Journal of Chemical Physics* **112**, 9479-9488, doi:10.1063/1.481566 (2000).

137 Huerta-Viga, A., Domingos, S. R., Amirjalayer, S. & Woutersen, S. A salt-bridge structure in solution revealed by 2D-IR spectroscopy. *Physical Chemistry Chemical Physics* **16**, 15784-15786, doi:10.1039/C4CP00233D (2014).

138 Lotze, S. & Bakker, H. J. Structure and dynamics of a salt-bridge model system in water and DMSO. *The Journal of Chemical Physics* **142**, 212436, doi:10.1063/1.4918904 (2015).

139 Neese, F. The ORCA program system. *WIREs Computational Molecular Science* **2**, 73-78, doi:10.1002/wcms.81 (2012).

140 Lee, C., Yang, W. & Parr, R. G. Development of the Colle-Salvetti correlation-energy formula into a functional of the electron density. *Physical Review B* **37**, 785-789, doi:10.1103/PhysRevB.37.785 (1988).

141 Becke, A. D. Density-functional exchange-energy approximation with correct asymptotic behavior. *Physical Review A* **38**, 3098-3100, doi:10.1103/PhysRevA.38.3098 (1988).

142 Grimme, S., Ehrlich, S. & Goerigk, L. Effect of the damping function in dispersion corrected density functional theory. *Journal of Computational Chemistry* **32**, 1456-1465, doi:10.1002/jcc.21759 (2011).

143 Grimme, S., Antony, J., Ehrlich, S. & Krieg, H. A consistent and accurate ab initio parametrization of density functional dispersion correction (DFT-D) for the 94 elements H-Pu. *The Journal of Chemical Physics* **132**, 154104, doi:10.1063/1.3382344 (2010).

144 Weigend, F. & Ahlrichs, R. Balanced basis sets of split valence, triple zeta valence and quadruple zeta valence quality for H to Rn: Design and assessment of accuracy. *Physical Chemistry Chemical Physics* **7**, 3297-3305, doi:10.1039/B508541A (2005).

145 Weigend, F. Accurate Coulomb-fitting basis sets for H to Rn. *Physical Chemistry Chemical Physics* **8**, 1057-1065, doi:10.1039/B515623H (2006).

146 Scalmani, G. & Frisch, M. J. Continuous surface charge polarizable continuum models of solvation. I. General formalism. *The Journal of Chemical Physics* **132**, 114110, doi:10.1063/1.3359469 (2010).

147 Scheiner, S. Relative Strengths of NH··O and CH··O Hydrogen Bonds between Polypeptide Chain Segments. *The Journal of Physical Chemistry B* **109**, 16132-16141, doi:10.1021/jp053416d (2005).

148 Keuleers, R., Desseyn, H. O., Rousseau, B. & Van Alsenoy, C. Vibrational Analysis of Urea. *The Journal of Physical Chemistry A* **103**, 4621-4630, doi:10.1021/jp984180z (1999).

149 Saito, Y., Machida, K. & Uno, T. Infrared spectra of partially deuterated ureas. *Spectrochimica Acta Part A: Molecular Spectroscopy* **27**, 991-1002, doi:https://doi.org/10.1016/0584-8539(71)80183-6 (1971).

150 Hadži, D., Kidrič, J., Kneževic, Ž. V. & Barlič, B. The normal coordinate analysis of urea, thiourea, and thier isotopic analogues in the solid phase and in solution. *Spectrochimica Acta Part A: Molecular Spectroscopy* **32**, 693-704, doi:https://doi.org/10.1016/0584-8539(76)80136-5 (1976).

151 Grdadolnik, J. & Maréchal, Y. Urea and urea–water solutions—an infrared study. *Journal of Molecular Structure* **615**, 177-189, doi:https://doi.org/10.1016/S0022-2860(02)00214-4 (2002).

152 Mukherjee, P., Kass, I., Arkin, I. T. & Zanni, M. T. Picosecond dynamics of a membrane protein revealed by 2D IR. *Proceedings of the National Academy of Sciences of the United States of America* **103**, 3528-3533, doi:10.1073/pnas.0508833103 (2006).

153 Kim, Y. S. & Hochstrasser, R. M. Applications of 2D IR Spectroscopy to Peptides, Proteins, and Hydrogen-Bond Dynamics. *The Journal of Physical Chemistry B* **113**, 8231-8251, doi:10.1021/jp8113978 (2009).

154 Cundiff, S. T. & Mukamel, S. Optical multidimensional coherent spectroscopy. *Physics Today* **66**, 44-49, doi:10.1063/pt.3.2047 (2013).

155 Tokmakoff, A. Two-Dimensional Line Shapes Derived from Coherent Third-Order Nonlinear Spectroscopy. *The Journal of Physical Chemistry A* **104**, 4247-4255, doi:10.1021/jp993207r (2000).

156 van der Post, S. T. *et al.* Strong frequency dependence of vibrational relaxation in bulk and surface water reveals sub-picosecond structural heterogeneity. *Nature Communications* **6**, 8384, doi:10.1038/ncomms9384 (2015).

157 De Marco, L., Ramasesha, K. & Tokmakoff, A. Experimental Evidence of Fermi Resonances in Isotopically Dilute Water from Ultrafast Broadband IR Spectroscopy. *The Journal of Physical Chemistry B* **117**, 15319-15327, doi:10.1021/jp4034613 (2013).

158 Szyc, Ł., Dwyer, J. R., Nibbering, E. T. J. & Elsaesser, T. Ultrafast dynamics of N–H and O–H stretching excitations in hydrated DNA oligomers. *Chemical Physics* **357**, 36-44, doi:https://doi.org/10.1016/j.chemphys.2008.08.013 (2009).

159 Hamm, P., Lim, M. & Hochstrasser, R. M. Structure of the Amide I Band of Peptides Measured by Femtosecond Nonlinear-Infrared Spectroscopy. *The Journal of Physical Chemistry B* **102**, 6123-6138, doi:10.1021/jp9813286 (1998).

160 Fenn, E. E. & Fayer, M. D. Extracting 2D IR frequency-frequency correlation functions from two component systems. **135**, 074502, doi:10.1063/1.3625278 (2011).

161 Kwak, K., Park, S., Finkelstein, I. J. & Fayer, M. D. Frequency-frequency correlation functions and apodization in two-dimensional infrared vibrational echo spectroscopy: A new approach. **127**, 124503, doi:10.1063/1.2772269 (2007).

162 Guo, Q., Pagano, P., Li, Y.-L., Kohen, A. & Cheatum, C. M. Line shape analysis of two-dimensional infrared spectra. *The Journal of Chemical Physics* **142**, 212427, doi:10.1063/1.4918350 (2015).

163 DeCamp, M. F. *et al.* Amide I Vibrational Dynamics of N-Methylacetamide in Polar Solvents: The Role of Electrostatic Interactions. *The Journal of Physical Chemistry B* **109**, 11016-11026, doi:10.1021/jp050257p (2005).

164 HoozenJr., B. L. V. & Petersen, P. B. Vibrational tug-of-war: The pKA dependence of the broad vibrational features of strongly hydrogen-bonded carboxylic acids. *The Journal of Chemical Physics* **148**, 134309, doi:10.1063/1.5026675 (2018).

165 Kühne, T. D. & Khaliullin, R. Z. Electronic signature of the instantaneous asymmetry in the first coordination shell of liquid water. *Nature Communications* **4**, 1450, doi:10.1038/ncomms2459 (2013).

166 Kühne, T. D. & Khaliullin, R. Z. Nature of the Asymmetry in the Hydrogen-Bond Networks of Hexagonal Ice and Liquid Water. *Journal of the American Chemical Society* **136**, 3395-3399, doi:10.1021/ja411161a (2014).

167 Elgabarty, H. & Kühne, T. D. Tumbling with a limp: local asymmetry in water's hydrogen bond network and its consequences. *Physical Chemistry Chemical Physics* **22**, 10397-10411, doi:10.1039/C9CP06960G (2020).

168 LeBel, R. G. & Goring, D. A. I. Density, Viscosity, Refractive Index, and Hygroscopicity of Mixtures of Water and Dimethyl Sulfoxide. *Journal of Chemical & Engineering Data* **7**, 100-101, doi:10.1021/je60012a032 (1962).

169 Eaves, J. D. *et al.* Hydrogen bonds in liquid water are broken only fleetingly. *Proceedings of the National Academy of Sciences of the United States of America* **102**, 13019-13022, doi:10.1073/pnas.0505125102 (2005).

170 Canchi, D. R. & García, A. E. Cosolvent Effects on Protein Stability. *Annual Review of Physical Chemistry* **64**, 273-293, doi:10.1146/annurev-physchem-040412-110156 (2013).

171 Moeser, B. & Horinek, D. Unified Description of Urea Denaturation: Backbone and Side Chains Contribute Equally in the Transfer Model. *The Journal of Physical Chemistry B* **118**, 107-114, doi:10.1021/jp409934q (2014).

172 Goyal, S., Chattopadhyay, A., Kasavajhala, K. & Priyakumar, U. D. Role of Urea–Aromatic Stacking Interactions in Stabilizing the Aromatic Residues of the Protein in Urea-Induced Denatured State. *Journal of the American Chemical Society* **139**, 14931-14946, doi:10.1021/jacs.7b05463 (2017).

173 H.S, G., Melavanki, R. M., D, N., P, B. & Kusanur, R. A. Binding of boronic acids with sugars in aqueous solution at physiological pH - Estimation of association and dissociation constants using spectroscopic method. *Journal of Molecular Liquids* **227**, 37-43, doi:https://doi.org/10.1016/j.molliq.2016.11.097 (2017).

174 Banipal, T. S., Kaur, R. & Banipal, P. K. Interactions of diazepam with sodium dodecylsulfate and hexadecyl trimethyl ammonium bromide: Conductometric, UV–visible spectroscopy, fluorescence and NMR studies. *Journal of Molecular Liquids* **236**, 331-337, doi:https://doi.org/10.1016/j.molliq.2017.04.043 (2017).

175 Rakipov, I. T. *et al.* FTIR – spectroscopy of intermolecular interactions of pyrrole in solutions: The influence of media and cooperativity of hydrogen bonds. *Journal of Molecular Liquids* **277**, 200-206, doi:https://doi.org/10.1016/j.molliq.2018.12.117 (2019).

176 Malm, C., Kim, H., Wagner, M. & Hunger, J. Complexity in Acid–Base Titrations: Multimer Formation Between Phosphoric Acids and Imines. *Chemistry – A European Journal* **23**, 10853-10860, doi:10.1002/chem.201701576 (2017).
177 Chitra, R. *et al.* Hydrogen bonding in thiourea: diethyl oxalate complex in 2:1 ratio. *Journal of Chemical Crystallography* **35**, 509-512, doi:10.1007/s10870-005-2853-9 (2005).
178 The errors were estimated by fixing the chemical shift of the complex to the optimized value of the association model fit. The corresponding association constants to a change of the fitchi value of 100% was then defined as the error. .
179 Zhang, Y. & Cremer, P. S. Interactions between macromolecules and ions: the Hofmeister series. *Current Opinion in Chemical Biology* **10**, 658-663, doi:https://doi.org/10.1016/j.cbpa.2006.09.020 (2006).
180 Vanderheyden, L. & Zeegers-Huyskens, T. Infrared and Raman study of the interaction between methyl acetate and phenol derivatives. *Journal of Molecular Liquids* **25**, 1-11, doi:https://doi.org/10.1016/0167-7322(83)80003-8 (1983).
181 Gosavi, R. K., Agarwala, U. & Rao, C. N. R. Infrared Spectra and Configuration of Alkylthiourea Derivatives. Normal Vibrations of N,N′-Dimethyl- and Tetramethylthiourea. *Journal of the American Chemical Society* **89**, 235-239, doi:10.1021/ja00978a009 (1967).
182 Willem M. Nissink, J., Boerrigter, H., Verboom, W., N. Reinhoudt, D. & H. van der Maas, J. An infrared study of host–guest association in solution by substituted resorcinarene cavitands. Part II.1 Comparison of halide complexation by tetrathiourea cavitands and a simple thiourea. *Journal of the Chemical Society, Perkin Transactions 2*, 2623-2630, doi:10.1039/A806519E (1998).
183 Russell, R. A. & Thompson, H. W. Vibrational spectra and geometrical isomerism in amides. *Spectrochimica Acta* **8**, 138-141, doi:https://doi.org/10.1016/0371-1951(56)80049-0 (1956).
184 Cohen, B. & Weiss, S. IR lines broadened by chemical exchange. *The Journal of Chemical Physics* **72**, 6804-6804, doi:10.1063/1.439173 (1980).
185 Ojha, D., Karhan, K. & Kühne, T. D. On the Hydrogen Bond Strength and Vibrational Spectroscopy of Liquid Water. *Scientific Reports* **8**, 16888, doi:10.1038/s41598-018-35357-9 (2018).
186 Note, that the solubility of DPTU in toluene is too low to reliably extract K from infrared experiments.
187 Reichardt, C. Solvatochromic Dyes as Solvent Polarity Indicators. *Chemical Reviews* **94**, 2319-2358, doi:10.1021/cr00032a005 (1994).
188 Pellisier, H. *Recent Developments in Asymmetric Organocatalysis*. (2010).
189 Olga V. Serdyuk, C. M. H. a. S. B. T. Bifunctional primary amine-thioureas in asymmetric organocatalysis. *Royal Society of Chemistry* **11**, 7051-7071, doi:10.1039/C3OB41403E (2013).
190 Zhang, Z. G., Bao, Z. B. & Xing, H. B. N, N '-Bis 3,5-bis(trifluoromethyl)phenyl thiourea: a privileged motif for catalyst development. *Organic & Biomolecular Chemistry* **12**, 3151-3162, doi:10.1039/c4ob00306c (2014).
191 Meyer, E. A., Castellano, R. K. & Diederich, F. Interactions with Aromatic Rings in Chemical and Biological Recognition. *Angewandte Chemie International Edition* **42**, 1210-1250, doi:https://doi.org/10.1002/anie.200390319 (2003).
192 Ehrhard, A. A., Jäger, S., Malm, C., Basaran, S. & Hunger, J. CF3-groups critically enhance the binding of thiourea catalysts to ketones – a NMR and FT-IR study.

Journal of Molecular Liquids **296**, 111829, doi:https://doi.org/10.1016/j.molliq.2019.111829 (2019).

193 Woutersen, S., Emmerichs, U. & Bakker, H. J. Femtosecond Mid-IR Pump-Probe Spectroscopy of Liquid Water: Evidence for a Two-Component Structure. *Science* **278**, 658-660, doi:10.1126/science.278.5338.658 (1997).

194 Schäfer, T., Lindner, J., Vöhringer, P. & Schwarzer, D. OD stretch vibrational relaxation of HOD in liquid to supercritical H2O. *The Journal of Chemical Physics* **130**, 224502, doi:10.1063/1.3151673 (2009).

195 Schwarzer, D., Lindner, J. & Vöhringer, P. OH-Stretch Vibrational Relaxation of HOD in Liquid to Supercritical D2O. *The Journal of Physical Chemistry A* **110**, 2858-2867, doi:10.1021/jp0530350 (2006).

196 Piatkowski, L., Eisenthal, K. B. & Bakker, H. J. Ultrafast intermolecular energy transfer in heavy water. *Physical Chemistry Chemical Physics* **11**, 9033-9038, doi:10.1039/B908975F (2009).

197 van der Post, S. T. *et al.* Strong frequency dependence of vibrational relaxation in bulk and surface water reveals sub-picosecond structural heterogeneity. *Nature Communications* **6**, 8384, doi:10.1038/ncomms9384 (2015).

198 Suzuki, I., Tsuboi, M. & Shimanouchi, T. An intra-molecular interaction between the NH and phenyl groups in N-methylphenylacetamide. *Spectrochimica Acta* **16**, 467-470, doi:https://doi.org/10.1016/0371-1951(60)80041-0 (1960).

199 Suzuki, I. INFRARED SPECTRA AND NORMAL VIBRATIONS OF THIOAMIDES - .3. N-METHYLTHIOFORMAMIDE AND N-METHYLTHIOACETAMIDE. *Bull. Chem. Soc. Jpn.* **35**, 1456-1464, doi:10.1246/bcsj.35.1456 (1962).

200 Limbach, H.-H. *et al.* NMR Parameters and Geometries of OHN and ODN Hydrogen Bonds of Pyridine–Acid Complexes. *Chemistry – A European Journal* **10**, 5195-5204, doi:https://doi.org/10.1002/chem.200400212 (2004).